161

Neurons on 3D polymer nanostructures

Andreea Anamaria Belu

Neurons on 3D polymer nanostructures

Andreea Anamaria Belu

JÜLICH
Forschungszentrum

Mitglied der Helmholtz-Gemeinschaft

JÜLICH
Forschungszentrum

Mitglied der Helmholtz-Gemeinschaft

Neurons on 3D polymer nanostructures

Andreea Anamaria Belu

Abstract

The interface between living cells and artificial surfaces is highly relevant for biomedical applications such as implants and organized cell growth for tissue reconstruction as well as for basic science purposes. The topography of implantable biomaterials is critical for optimizing the electrical coupling between cells and device surface. One way to modulate cellular responses is to vary surface topographies. Instructive biomaterials with different surface topographies can regulate cellular behavior from initial attachment and further dictate the response of surrounding tissue. A considerable attention was directed towards 3D micro- and nanostructured polymers. In this study, the influence of isotropic and anisotropic 3D polymer surfaces on the adhesion and maturation of primary neurons is presented.

This work mainly consists of three parts: the 3D micro- and nanostructured polymer fabrication and characterization, followed by the evaluation of the influence of surface topographies on neuronal behaviour responses. Additionally, a novel resin embedding procedure was developed for morphological visualization of neuron interface with 3D surfaces at the nanoscale. Particular attention was given to the cell membrane wrapping around the nanostructures studied by scanning electron microscopy and focused ion beam sectioning.

First, a reliable method for the fabrication of 3D structures was established with the possibility of using large range of sizes and heights (on 1 cm^2 surface area) based on nanoimprint lithography: i) Isotropic surfaces with 100 nm and 400 nm high posts with diameter and distance ranging from 250 nm to 2 μm and ii) Gradient patterns of 250 nm diameter posts and linear slopes of $0.15 \cdot 10^{-3}$, $0.75 \cdot 10^{-3}$, $1.95 \cdot 10^{-3}$, and $3.95 \cdot 10^{-3}$/mm. These polymer substrates exhibited high cell viability and neuronal maturation. Employing the systematic design variations of the surface topographies, the engulfment-like process of the 3D nanostructures by the cell membrane has been quantified. An optimal 3D structured area (100 nm high posts with 250 nm diameter and 1 μm pitch) has been found to increase the cell membrane adhesion in comparison to the planar surface. In addition, the 3D pillars enhanced axon growth and alignment to the topography, an effect that diminished with decreasing pillars height. However, for the lower pillar height the alignment could be induced by gradient patterns with 1 μm and 4 μm distance between the pillars. Finally, 3D asymmetric surfaces characterized by dense inclined PPX polymer nanopillars, have been used to induce axon elongation and initial directionality of axon formation. This thesis contributes to the understanding of neuron adhesion, neuritogenesis, and neurite elongation in response to micro- and nanometer range pattern dimensions. Implementing axonal guidance and elongation by use of topography (3D nano-modified surfaces) can be a versatile tool for neuronal applications, such as nerve regeneration.

Zusammenfassung

Die Schnittstelle zwischen lebenden Zellen und künstlichen Substraten ist ein zentraler Faktor in biomedizinischen Anwendungen, wie der Implantatherstellung, dem organisierten Zellwachstum für die Geweberekonstruktion oder der Grundlagenforschung. Dabei spielt die Oberflächentopographie der implantierbaren Biomaterialien eine wichtige Rolle bei der Optimierung der elektrischen Kopplung zwischen Zelle und Chipoberfläche. Eine Möglichkeit zelluläre Reaktionen zu beeinflussen, ist die Veränderung der Oberflächenbeschaffenheit. Nano- und zell-instruktive Biomaterialien mit unterschiedlichen Topographien können zelluläres Verhalten vom ersten Anheften an regulieren und darüber hinaus die Reaktion des umliegenden Gewebes bestimmen. Der Fokus dieser Arbeit liegt auf 3D mikro- und nanostrukturieren Polymeren. Dabei wurde hauptsächlich der Einfluss isotroper und anisotroper 3D Polymeroberflächen auf die Adhäsion und Entwicklung der primären Neuronen untersucht.

Diese Arbeit gliedert sich in drei Teile: Die Herstellung und Charakterisierung der 3D mikro- und nanostrukturierten Polymere, die Evaluation des Topographieeinflusses auf das neuronale Verhalten und die Entwicklung einer neuen Methode zur Visualisierung der Schnittstellen zwischen Neuronen und strukturierten Oberflächen. Letztere basiert auf einer speziellen Harzeinbettung und ermöglicht eine Auflösung im Nanometer-Bereich. Im Besonderen wurde die Umschlingung der Zellmembran um die Nanostrukturen untersucht. Dazu wurden Querschnitte mittels fokussierter Ionenstrahlpräparation (focus ion beam, FIB) hergestellt, welche unter dem Rasterelektronenmikroskop visualisiert wurden.

Zunächst wurde eine verlässliche Methode zur Herstellung der 3D Strukturen basierend auf Nanoimprint Lithographie entwickelt. Diese ermöglicht eine große Variation an Strukturbreiten und –höhen auf einer Fläche von 1 cm^2: i) Homogen verteilte Säulen mit einer Höhe von 100 nm und 400 nm sowie einem Durchmesser von 250 nm bis zu 2 μm und einer Distanz von 250 nm bis zu 4 μm und ii) Säulen mit einem Durchmesser von 250 nm angeordnet in einem distanzabhängigen Gradienten von $0.15 \cdot 10^{-3}$, $0.75 \cdot 10^{-3}$, $1.95 \cdot 10^{-3}$ und $3.95 \cdot 10^{-3}$/mm. Diese Polymerstrukturen wurden im nächsten Schritt in *in vitro* Experimenten getestet und zeigten eine gute Zell-Viabilität und neuronale Entwicklung. Durch systematische Variation des Topographie-Designs wurde die Umschlingung der Nanostrukturen durch die Zellmembran untersucht und quantifiziert. Es hat sich herausgestellt, dass eine optimal strukturierte Oberfläche (Säulen mit einer Höhe von 100 nm, einem Durchmesser von 250 nm und einem Abstand von 1 μm) die Adhäsion der Zellmembran an die Polymerstruktur im Vergleich zu einer planaren Oberfläche verbessert. Außerdem beschleunigten die 3D Säulen das Wachstum des Axons und führten zu dessen Ausrichtung entlang der Topographie. Dieser Effekt war für die hohen Säulen am stärksten und ließ mit abnehmender Säulenhöhe nach. Um dennoch eine Ausrichtung auch an den

niedrigen Strukturhöhen zu erreichen, wurden Gradientenstrukturen eingesetzt (1 µm und 4 µm Abstand zwischen den Säulen). Zuletzt wurden asymmetrische 3D Strukturen aus PPX-Polymer verwendet, die sich durch dicht gepackte, geneigte Pfeiler auszeichnen. Mit diesen konnte die Direktionalität der Axonbildung und –elongation beeinflusst werden. Zusammengefasst zeigen die Ergebnisse, dass durch die Vorgabe eines 3D Oberflächendesigns eine Kontrolle des neuronalen Wachstumsverhaltens erreicht werden kann.

Diese Arbeit trägt zum Verständnis der neuronalen Adhäsion, der Neuritenentwicklung und –elongation in Abhängigkeit der Oberflächenstruktur im Mikro- und Nanometerbereich bei. Die Erkenntnisse können zukünftig dazu genutzt werden die axonale Wachstumsrichtung durch geeignete Topographien (3D strukturierte Oberflächen) vorzugeben und bieten somit eine Grundlage für viele Anwendungen in der Biomedizin, wie beispielsweise die Regeneration von Nerven.

Table of contents

1. INTRODUCTION

Brain computer interfaces (BCI) are known as implantable devices, which can be connected to the nervous system helping people to restore neural functions.[1] Some of these devices are already in use such as cochlear implants in treating deafness[2] or deep brain stimulators used in treatment of neurodegenerative diseases, such as Parkinson's disease.[3] It was shown that cortically embedded intraparenchymal electrode arrays are capable of recording electrical activity from individual neurons in humans and monkeys with relatively large extracellular action potentials. However, a risk of central nervous system infections due to the local parenchymal damage is still present. Other drawbacks are the activation and migration of microglia and astrocytes around the electrodes causing neuronal cell death and recording decay.[4,5] Improvements should also relate to the spatial resolution and directionality.[6] Therefore, a comprehensive investigation is necessary to understand the development of neuronal cells on the implant surface in relation to its topography and chemo-physical properties. Nanotechnology provides the tools that allow interaction with cells and subcellular processes on the appropriate scale. Moreover, the number of electrodes per area can be enormously increased using nanotechnology, which is absolutely necessary considering the cellular and synaptic density in the brain. Since it is not possible (yet) to organize and mimic the three dimensional (3D) complexity of the brain, another strategy has been developed to derive information on signal processing in the nervous tissue. *In vitro* applications present an opportunity to explore fundamental theories behind regenerative medicine. Understanding which substrate features lead to the desired neuronal behavior will be fundamental for the future of cell culture and *in vitro* experimentation and improvement of implant surfaces. The goal of cell culture surfaces has been to provide an *in vitro* environment that generates cell responses as similar as possible to those found *in vivo*. 2D surfaces are inexpensive and accepted culture systems for cell comparison although the physiological relevance of cell behavior is lost in such systems. 3D matrices provide a more physiological environment, however there is no fabrication standard and cell behavior in different systems is difficult to quantify. Bridging the gap between cell analysis on 2D glass or polymer systems and analysis in a complex 3D matrix is made possible by equivocating surface modification to a 3D structured surface. The bio-interface at the substrate surface is an essential junction that provides environmental cues for cell signaling: chemical guidance cues, mechanical properties, and surface topography. Despite the increasing interest, it is still not possible to accurately predict cell responses to physical cues and elucidate the underlying mechanisms. Previous studies quantified neuronal responses induced by the substrate surfaces including: the number of cells forming neurites or axons; the average number of neurites per cell; the total neurite

extension length; the average neurite length per cell; the length of the longest neurite or axon; and the degree of neurite branching.[7] Furthermore, one important aspect is the neuronal growth guidance or alignment induced by the surface. The neuronal alignment can be measured for the cell soma, the cellular extensions, or both.[8] The cell response to the engineered substrates can confirm the biocompatibility of a material which can also induce and influence cell adhesion, control differentiation, or dictate cell outgrowth. The screening of how cells are affected by the interface with nanostructured materials can lead to a predictable correlation between the surface topography and cell response with a valuable role in cellular application development. In this regard, systematic investigations are necessary to allow the implementation of efficient topographical parameters (diameter, height, regularity, density, etc). First, the selection of suitable materials is crucial in order to obtain the physical and geometrical substrate requirements at different scales. Materials for cell culture studies should have acceptable chemical and physical properties in order to be biocompatible. Ideally, materials should have the approval of the Food and Drug Administration (FDA). Synthetic materials offer several benefits such as favorable cell responses, controllable chemical composition, tunable physical and mechanical properties, simplicity of synthesis and processing, and a compatibility with various fabrication techniques.[9] Here, two different materials (OrmoComp and parylene polymers) were used to fabricate both isotropic and anisotropic surfaces. OrmoComp material has received increased interest from the medical device community due to its biocompatibility[10] and controllable 3D environment fabrication.[4,5–9] Taking advantage of the favorable protein binding properties after polymerization,[11,12,14] OrmoComp was used to fabricate replicas with a wide range of dimensions (250 nm to 4 μm) and a reliable pattern fidelity over large distances (1 x 1 cm). On the other hand, parylene represents one of the most common polymers that has been already established in many clinical applications or in research and development and serves as a carrier or as an insulation material for neural implants.[16] Effective neural recording and stimulation have been demonstrated using electrodes coated with parylene C (PPX) polymer films.[17–20] Parylene deposition process can give different structures through its output: bulk parylene (planar-PPX), columnar-PPX, or more complex architectures.[21] In this thesis, bulk parylene used for replicas was compared with OrmoComp's chemical and topographical influence. Furthermore, the PPX deposition was engineered in order to create anisotropic textured of columnar-PPX nanopillars under a specific tilt angle.[22,23]

An important part of investigating cell responses is the actual interface, particularly for neural prosthesis and brain computer interfaces.[9,24] Visualization of cell–electrode interface at the nanoscale remains a big challenge for understanding how the cell attaches and responds to the device surface. Different techniques are used in literature such as fluorescence microscopy[25], surface plasmon microscopy[26], or electron microscopy.[27–29] The most promising technique represents the combination between focused ion beam (FIB) and scanning electron microscope (SEM).[30–32] However, a procedure of preparing biological

samples on planar and 3D nanostructures needed to be developed.[33] The preparation method was based on ultra-thin resin embedding of biological samples after fixation, dehydration, and staining. Resin embedding was shown to be a versatile preparation method for more than interface investigation. Fluorescence microscopy, SEM characterization of cell morphology with almost no resin over-embedding, could be followed by sequential cross sectioning of the cell-surface interface investigation.

A driving force for this study was to find suitably nano-modified surfaces for the construction of improved neural implants with enhanced resolution and biocompatibility. Therefore, an important part of the study focused on the big challenge of understanding how the cell attaches and responds to polymer surfaces. 3D vertical or tilted aligned nano- and micropillar large arrays were used for a comprehensive *in vitro* study of the development of primary cortical neurons. Neurons were cultured on two kinds of topographies (isotropic and anisotropic), and two types of biomaterials (OrmoComp and parylene C). A comprehensive *in vitro* study of the different topographies was performed in regards to neuron polarity in the early stages of development.[22,34–36] Nanotopography-cell interaction studies showed that morphological changes could be initiated. In comparison to planar samples the neuron-material nano-interface was shown to support neurite elongation and branching.[37,38] In the case of isotropic surface, accelerated neurite outgrowth and cell differentiation was observed on periodic structures with a pitch in range of a few microns down to sub-micron ranges.[39–41] Neurite elongation and polarization was shown to be increased for anisotropic surfaces with line-based patterns at the nanoscale.[42] Here, a linear gradient was designed in order to compare the influence of different interpillar distances on neuron alignment and polarization. The anisotropic surfaces are highly important in tissue regeneration, due to their ability to guide cell alignment.[43–46] However, accelerated neurite elongation and neuronal polarization observed still require a molecular understanding. In addition to previous studies,[47–51] the observed effects of these topographic surfaces present a way of improving cell adhesion, neurogenesis, and alignment.

The goal of this thesis was to establish a large-area screening of cellular interactions with surface topographies using 3D nanostructured substrates presented above. First, in chapter 2, the theoretical background of the topic discussed is given. The chemical, physical, and material compliance influencing neuronal responses were described in detail. Moreover, the principal techniques for 3D substrate fabrication and characterization of cell development are explained. An overview of the materials and methods used is given in chapter 3. This includes substrate fabrication, characterization techniques, and an introduction to the cell culture protocols for fluorescence and electron microscopy. The results of this thesis are presented and discussed in chapters 4-6. Chapter 4 was focused on the 3D OrmoComp isotropic and anisotropic replicas fabrication with different designs. Furthermore, the optimization of the ultra-thin resin embedding resin was described in chapter 5. The novel procedure was used for visualization of cell membrane wrapping

around the 3D structures at the nanoscale and quantification of the actual cell-surface interface. These results were used to develop a wrapping model that calculates the membrane deformation energy and adhesion energy for different geometries. Neuronal behavior on isotropic and anisotropic surfaces with different dimensions is shown and discussed (chapter 6). Geometrical cues and mechanical properties of the material were used to investigate neuronal development and adhesion interface. Furthermore, cell guidance was also quantified. In chapter 7, the conclusions of the overall work are presented with particular attention on the novelties and impulses for future investigations.

2. FUNDAMENTALS

2.1. Neural tissue

2.1.1. Overview of the nervous system

The level of complexity of the nervous system in living organisms ensures not only their survival but also organizes their interaction with the external environment. Its plasticity and development is often associated with the capability of acquiring new information and reaction to external stimuli. Nervous system of the vertebrate organism is composed of neural tissue, connective tissue, and blood vessels. It can be divided into two parts: central nervous system (CNS) and the peripheral nervous system (PNS). The CNS includes the brain and the spinal cord. The PNS is a mediator of information between the CNS and the peripheral tissue, delivering sensory information between them. The CNS is mainly composed of neurons and numerous glial cells that support the neurons.[52] Cells from the CNS were the focus of this work, specifically the neurons from the cerebral cortex while glial cells were suppressed during culture. Even though, neuroglia ensures the proper function of the neurons, only neurons can process information. This is important for neural implants since the formation of the glial scar reduces or eliminates long term stimulating/recording capabilities of these devices.[4]

2.1.2. Neural tissue anatomy

A typical mature neuron consists of a cell body or soma, an axon and multiple dendrites (Figure 2.1). Soma structures include: cell membrane, cytoplasm, and nucleus. Nucleus determines all cellular activities and stores DNA and RNA. The cell membrane is made of phospholipids, a combination of hydrophilic phosphate groups and hydrophobic lipids. This membrane is at the interface between the extracellular matrix (ECM) and the internal cytoplasm. The cytoplasm includes the cytoskeleton, Golgi apparatus, mitochondria, ribosomes. All of these components are responsible for cell activity and active responses in contact with external stimuli. Cell cytoskeleton is a highly dynamic, polymer-like structural mesh, responsible for cell architecture and internal tension balance. Another important role is maintaining the position of organelles and their reorganization during division, adhesion, migration, and intracellular transport.[53] Protein filaments such as microtubules, intermediate filaments, and actin filaments form the cell cytoskeleton. Many different proteins, called motor proteins, ensure filament cross-linking and sliding. Reorganization and adaptation of cell shape within living tissues is enabled by the molecular motors due to tension generation. Microtubules have a cylindrical shape with 25 nm diameter and a radial distribution from the centrosome to the plasma membrane. For this reason microtubules

play an important role in establishing and maintaining cell polarity.[54–56] Intermediate filaments are involved in maintaining cell shape and rigidity, and anchoring organelles such as the nucleus. They are typically 15 nm in diameter but have the ability to self-assemble in up to 812 nm wide filaments.[57–59] Actin filaments are even smaller in diameter, 7-9 nm. They are characterized by long semi-flexible polymer-like chains formed by repeating subunits of actin monomers. Actin filaments promote cell mobility by polymerization and depolymerization at the leading edge of the cell. This mechanism is possible due to the fact that actin filaments are linked to the plasma membrane through membrane-spanning proteins that allow the signals from the ECM to be transmitted to the cytoskeleton, and back. Dynamics of the actin cytoskeleton together with myosin II generate contractile forces that enable cells to move and contract.[60–63] Developed neurons are able to extend long and branching cellular processes from the cell body. These growing processes, neurites, are essential for intercellular communication and are divided into two types: axons and dendrites. Dendrites are shorter and highly branched, while axons are long processes with fewer branches. They transmit information to neighboring neurons through synaptic terminals, conducting electrical impulses. Dendrites can only receive electrochemical stimulation from other neurons and forward them to the soma. Each axon has a terminal process with fine extensions. During development, the axon terminus is called the growth cone. It ensures neurite guidance due through high dynamics and sensitivity towards chemical, topographical, and mechanical cues.[55] Structurally, a growth cone is composed of three areas that determine its shape and motion: a central zone filled with microtubules, an intermediary zone and a peripheral one, composed of the lamellipodium and filopodia.[64,65]
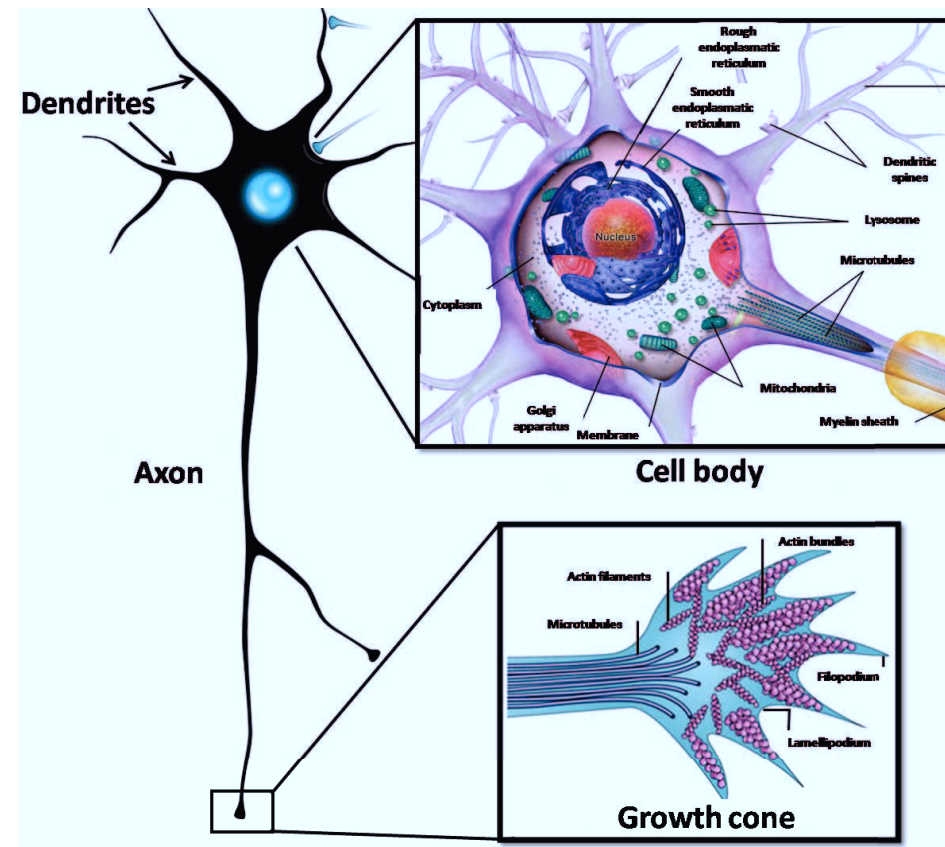
Figure 2.1. Structure of typical neuron, with detailed schematic representation of cell body[66] and growth cone.[67]

2.1.3. Development of neuronal cells

The studies exposed in this thesis have been performed using neurons from the cortex of rat embryos after 18 days of gestation. From a functional point of view, the cortex plays an important role in consciousness, memory, language, and thinking. Cerebral cortex encompasses about two-thirds of the brain mass.[68] *In vitro* development of embryonic neurons has been described in Arimura et al.[69] Morphological changes that occur during maturation are assigned to five separate stages of maturation (Figure 2.2).
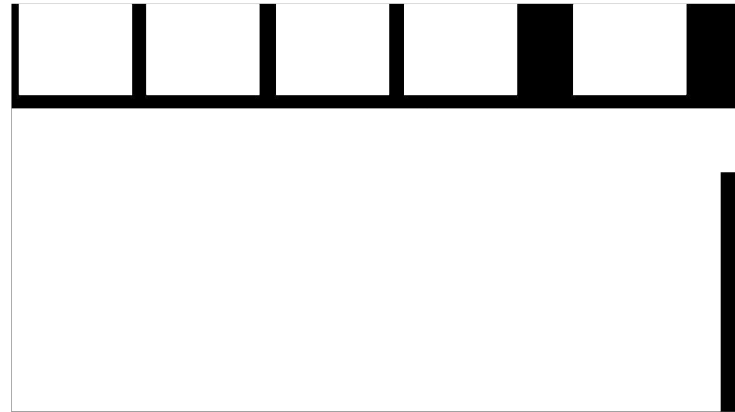
Figure 2.2. Neuronal maturation in *in vitro* cultures. During the first two stages of development, neurons present a number of minor processes which are morphologically equal. At Stage 3, one neurite breaks the symmetry and grows much faster than the others. A polar neuronal cell, with an axon and dendrites, is established at Stage 4. The formation of dendritic spines and synaptic connections happens at Stage 5 of development. Image adapted from Arimura et al.[69]

During Stage 1, soon after plating, short lamellipodia and filopodia processes are observed around the soma. After 1-2 DIV these processes become immature neurites. These changes are associated with Stage 2 of development. Breaking of symmetry between the neurites is mainly guided by the presence of the growth cone and takes place after 2-4 DIV. One of the neurite starts to elongate faster than the others (Stage 3). This longest neurite will acquire the molecular specificities of the axon while other neurites will differentiate into dendrites (Stage 4, 4-7 DIV). A fully mature and functional neuron will appear after 7 DIV (Stage 5). Spines are formed on dendrites that facilitate the connection between neighboring cells.[69]

2.2. Cell-surface relationship

2.2.1. Cell adhesion on artificial substrates

Immediately after plating, cells sink to the substrate and a nonspecific interaction is initially formed during adsorption. Cations from the medium (Ca^{2+}, Mg^{2+}) bridge the gap electrostatically between the negatively charged cell surface (glycocalyx) and, in this case, negatively charged substrate surface. The initial contacts are reinforced by ECM components. Few integrins secure the attachment points before connecting to microfilaments via a chain of proteins. Finally, when more integrins and microfilaments are recruited to the attachment sites, adhesion complexes form and the cytoskeleton reorganizes so that the cell can develop and migrate.

2.2.1.1. Cell interaction with the ECM

Connections between cells and the ECM are mediated by integrin dependent adhesion complexes. It is believed that adhesion receptors act as mechanosensors and these physical signals are further converted into biochemical ones. The biochemical signals are then propagated along the network of actin filaments and associated proteins. This leads to a physical ECM-cell linkage which regulates many cell morphological behaviors including actin organization and cell microenvironmental adaptation. The process is characterized by a continuous and bidirectional transduction of cytoskeleton generated forces in a dynamic reorganization.[70,71] ECM is a complex, hierarchically organized meshwork composed of many structural and nonstructural proteins assembled to support cells. Changes in the organization, amount, and type of proteins in the ECM is characteristic for different cell types.[72] It is well known that the ECM remodels cell behavior and morphology by imposing geometrical restriction, or stiffness.[73] Moreover, cells can also organize the ECM proteins which are secreted from the cell by exerting tension on the matrix.[74] The ECM contains a number of glycoproteins (fibronectin, lamininn, collagen) and proteoglycans (hyaluronan, heparin sulphate, chrondroitin sulfate) with multiple domains that have specific binding sites.[75] Although ECM proteins are widely used as *in vitro* adhesion proteins, non-specific adhesive molecules are also employed. Poly-L-lysine (PLL) and its enantiomer poly-D-lysine (PDL) are among the most commonly used. These positively charged adhesive molecules do not specifically bind receptors on the cell membrane, but form electrostatic interactions with the membrane.[76] The non-specific binding can result in a strong adhesion.[77,78]

2.2.1.2. Cell- ECM linkage: adhesion complexes

Cell adhesion on artificial surfaces occurs via several steps. Initially, the cells present nascent adhesions characterized by dot like structures less than 1 µm in diameter. These adhesion sites will eventually mature into adhesion complexes.[79] The formation of adhesion complexes is induced by the Rho-family GTPase Ras which are small structures between integrins, vinculin, and paxillin. Maturation of the adhesion complex is caused by Rho activation or external force.[80–82] Figure 2.3a shows the formation of an adhesion complex where integrins mediate the link between the substrate and the actin cytoskeleton through molecular adaptors such as vinculin, talin, and tensin.[83] When a cell takes a permanent position on an artificial surface, a mature adhesion complex forms (Figure 2.3b). During maturation, the level of cellular tension can affect the size of the complex. High stress levels induce large, supermatured adhesion complexes,[84] while in variable levels of stress the size of adhesion complexes reaches only 1 µm.[85] However, this correlation is only valid for early stages of cell adhesion (myosin mediated).[86] The size of completely matured adhesion complexes is in range of several square microns with a structural complex of macromolecules which crosslink the ECM to the cell interior via membrane bound receptors.
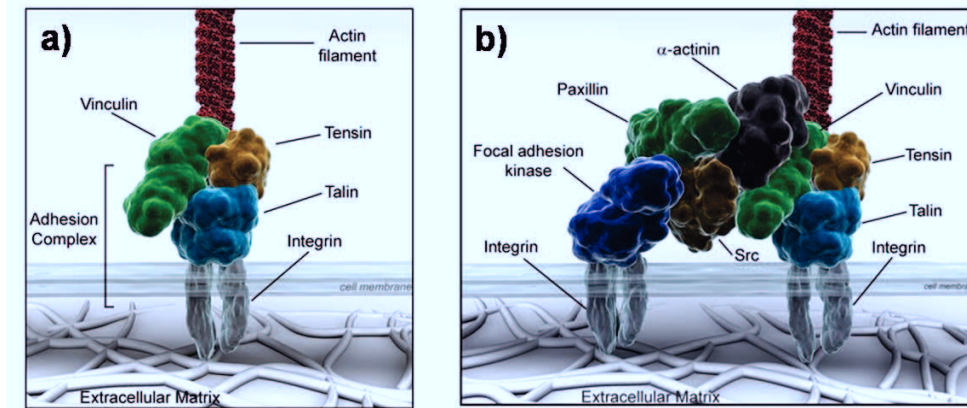
Figure 2.3. Structure of an adhesion complex (a) and a mature adhesion complex (b), adapted from [87].

Adhesion complexes play an important role in cell functions such as signaling or information processing. As highly dynamic structures, the adhesion complexes enable the cell to sense extracellular signals such as biochemical, mechanical, and geometrical.[73]

2.2.2. Neuronal guiding cues

The process of converting physical forces into biochemical signals that induce cellular responses is known as "mechanotransduction". During *in vivo* development, cells respond to physical cues by aligning and migrating along topographical features.[88] A step by step reconstruction of the microenvironment during *in vitro* neuronal guidance needs to be established. Directional cues are either repulsive or attractive, over a long or a short range. Migration and necessity of neurons to connect with each other involves guidance cues and sensory machinery located at the growth cone (extension of axon sensorial protrusions). Substrate surface modification used to change cell adhesion and development properties has been around for several decades.[89] However, despite the increasing interest, we still lack the ability to predict cell responses to physical cues and hopefully to elucidate the underlying mechanism. The three factors: chemical guidance cues, mechanical properties, and surface topography will be separately discussed in the following sub-sections (Figure 2.4).
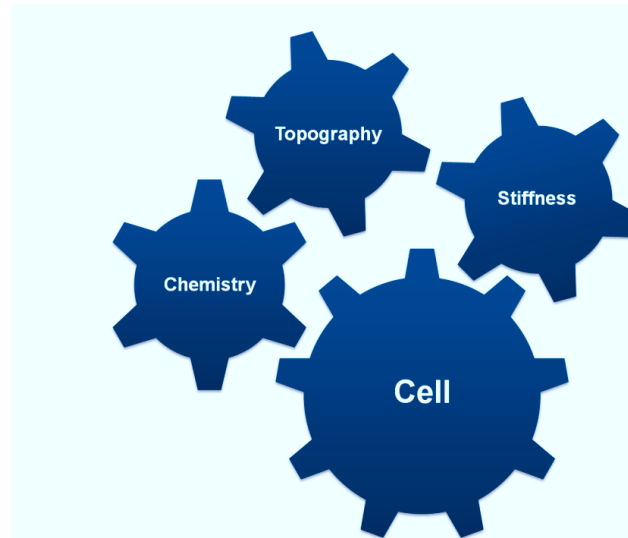
Figure 2.4. Cellular functions such as adhesion and development are affected by many factors of a substrate, including but not limited to exposed chemical groups, surface topography, and mechanical properties.

2.2.2.1. Chemical cues

Chemical cues represent the molecular interaction of cells with proteins that they encounter in the environment. During development, the axon is influenced by chemical signals such as: ECM and cell adhesion molecules, growth and neurotropic factors, immunoglobulin-like adhesion molecules (NCAM and L1), receptors (ephrins), neurotransmitters (acetylcholine).[90] Adhesion molecules such as L1 and NCAM were shown to promote neurite outgrowth and cell viability. In particular, L1 was used to induce a more specific attachment of neurons in detriment to astrocytes. Substrates patterned with gradients of ephrins receptors presented an interesting axon behavior. The axons grew in the direction of higher gradients but the growth stopped at higher densities, showing the ambiguous effect of these molecules in axon growth and guidance. On the other hand, neurotransmitters are vital to achieve a correct synapse formation and function. Moreover, if neurotransmitters were incorporated in different substrates, the cell cultures showed improvements in neuron survival and neurite extension.[90] The most common adhesive molecules are ECM proteins and cell-cell adhesion molecules. Examples of ECM proteins include fibronectin, laminin, and collagen. Instead of the whole proteins, specific sequences that correspond to the cell-binding sites of the proteins can be used. Some of the widely studied include: arginylglycylaspartic acid (RGD), Ile-Lys-Val-Ala-Val (IKVAV), PA22-2. These protein fragments are contributed to promoting cell adhesion and neurite outgrowth.[91] However, some surface modifications (high hydrophobicity) impaire the

ability of the protein to retain its native structure after adsorption producing significant changes in the protein conformation. These conformational changes can influence the recognition of a cell-binding site by integrin receptors.[92] For this reason, artificial growth-promoting molecules such as poly-L-lysine (PLL), poly-D-lysine (PDL),[93] and inhibitors such as polyethylene glycol (PEG) are commonly used.[94] In this case the molecules are physisorbed to the surface, through nonspecific anionic-cationic interactions. Although the interaction between polylysine and neurons is not mediated by cell surface receptors, PDL and PLL enantiomers generally promote cell adhesion and neurogenesis of neurons.[95] Another common method to study the effect of chemical modification of the surface without an alteration of the bulk properties is to use self-assembled monolayers (SAMs) and thin films. Self-assembly describes a process in which a disorganized system becomes organized through individual interactions between their components. This leads to a decrease of the surface free energy.[96] SAM surfaces are either used directly as biocompatible surfaces or undergo a secondary modification with biomolecules. Secondary modification can strongly influence the cell membrane binding and signaling. DNA, proteins, and other biologically active molecules are used to modify surfaces with functional biochemical moieties.[97] All molecules presented can be patterned onto surfaces with different techniques. Cell adhesive or non-adhesive regions are obtained on the substrate surface for metals, polymers, or glass. The presence of inhibitory regions is especially important to prevent non-specific binding of molecules and consequently cells. The synergistic action of both cues increases directional information on the neuronal cell body or neurites.[95,98–101]

2.2.2.2. Mechanical properties

Knowledge of mechanical properties of neurons or brain tissues would improve the biocompatibility and the electrical coupling of neuronal implants. Healthy tissue often reveals a distinct stiffness and mechanical sensitivity compared to diseased tissues. As a whole, the healthy brain stiffness has been estimated to be several hundred Pa.[102] An injured brain seems to be stiffer and has a higher number of glia cells.[103,104] Moreover, active forces inside the brain and mechanical properties of the ECM influence neuron development inducing elongation and guidance.[105,106] Natural or synthetic materials can be used to investigate the effect of substrate stiffness. Cross-linked natural polymers from the ECM like fibrin or collagen have the benefit of being biocompatible.[107] On the other hand, the ECM proteins can directly interact with the cell, which makes it difficult to discern if the cell response is due to substrate stiffness.[108] Synthetic polymers overcome these limitations. Materials used for fabrication of synthetic substrates are polymers, ceramics, and metals.[109] Synthetic polymers can possess a great variety of different chemical compositions and wide range of mechanical properties such as stiffness and Young's Modulus. The polymer network formation can be manipulated by the ratio of monomers and/or the amount of cross-linking agent and polymer blending.[107,108,110,111] One example of

a polymer with a wide range of Young's modulus (from 10 kPa to 1 MPa) is polydimethylsiloxane (PDMS). However, PDMS is not a good substrate for long term cell culture, due to its hydrophobicity and high chain mobility at the surface.[111,112] Hydrogels from bis-acrylamide cross-linked polyacrylamide were fabricated with a low rigidity in the range of 200 - 300 Pa. A comparison of this elastic soft substrate with a flat surface showed an increased neurite branching and neurite number on these substrates. Interestingly, no significant difference in neurite length was reported for this rigidity or even higher stiffness. Regarding cell spreading, it was observed that stiff gels induce an increase of cell body area.[113,114] An important role of stiffness consists in different neuronal responses compared with other types of cells, including astrocytes. F-actin polymerization on soft gels is more pronounced for neurons and this type of substrate can impair astrocyte proliferation.[115,116] The stiffness of a substrate not only affects the cell, but the cell can also respond and affect the material. As shown in Figure 2.5, the cells can respond differently according to substrate mechanical properties. For patterned surfaces, it was shown that stiffness can also depend on topography. Lower structures result in a rigid substrate and accordingly no input from cells (Figure 2.5a and c). In case of higher structures, the substrate can have softer compliance. Cells cultured on these structures can produce enough force to bend or deform the material (Figure 2.5b and d).[117,118]
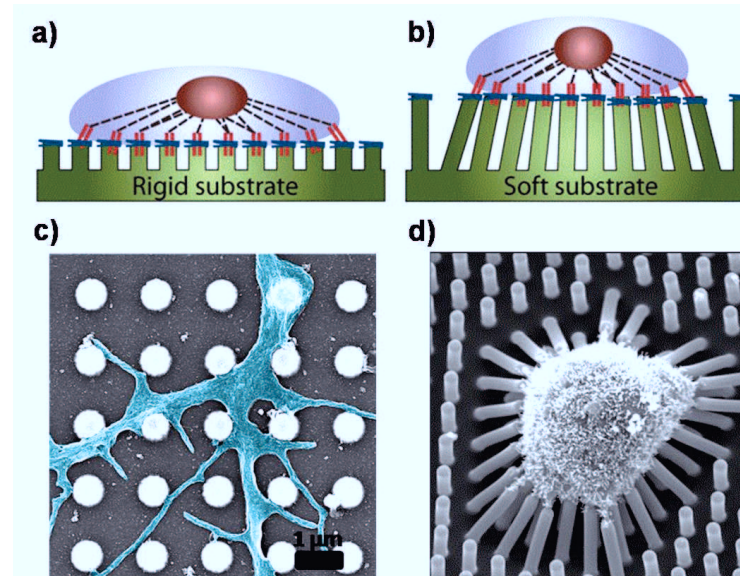
Figure 2.5. Cells sense and respond to external forces and changes in matrix mechanics by modulating their cytoskeletal contractility on a rigid substrate (a) and a soft substrate (b).[119] SEM pictures of cell interactions with a rigid pillar substrate (c) and a soft substrate (d). In soft microenvironments cells respond to mechanical forces and matrix mechanics through substrate deformation.[117]

2.2.2.3. Topography

Topography is characterized by depth, width, and pitch of the structures presented at the substrate surface. How cells respond to a wide range of pattern sizes and morphology has been investigated in numerous studies (Figure 2.6).[120] Patterns are divided in two categories: isotropic and anisotropic surfaces. Structures of isotopic patterns are uniform in all directions and can be well fabricated particles, dots, holes/pillars, nanorough surfaces. Anisotropic patterns are directionally dependent and include lines, grooves, aligned fibers, guidance conduits etc. Differences in cytoskeletal organization are related to actin polymerization, confined adhesion complexes formation and preferential protein adsorption and desorption.[121–123] All the effects of nano- and micropatterned topographies on cell responses have been studied extensively and will be presented in the following sub-sections.
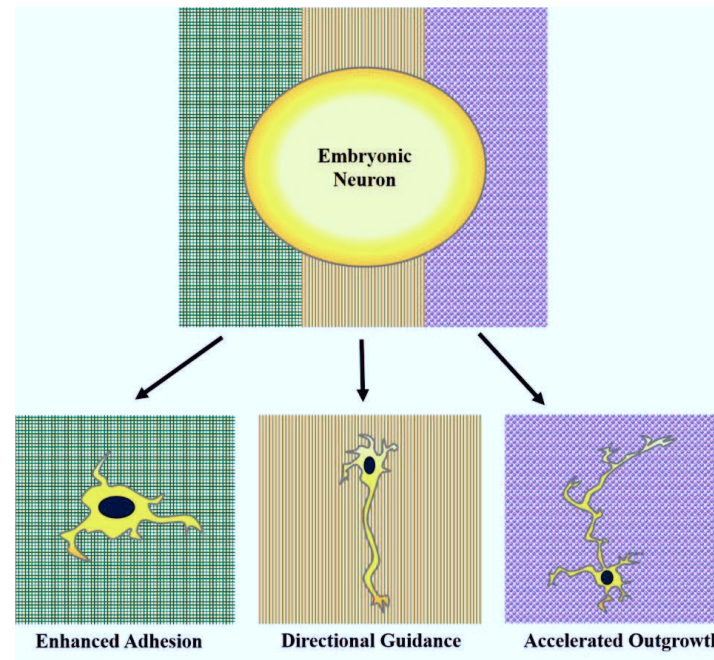
Figure 2.6. Neuronal behaviors on surface topographies: subcellular features of a substrate can exhibit a variety of different morphological and cellular changes.[120]

Anisotropic topography

In general, when cells are cultured on anisotropic topographies they tend to grow along the axis direction.[44,45] This phenomenon was first described by Harrison in 1912 and is known as topological or "contact guidance".[43] Groove patterns influence the cell orientation by width, depth, and spacing between the grooves.[46] A more pronounced orientation of cells cultured on grooved patterns was shown to increase with higher depths and decrease with increasing line width.[124] For larger line width, the cells attach to the flat surface between the grooves. When space between the grooves has a small width the adhesion complexes form and cells align along the pattern edges. The mechanism of contact guidance proposes that not only actin filaments and microtubules align along the grooves, but also adhesion complexes.[125–127] However, Walboomers et al.[128] observed that adhesion complexes may bend around grooves/ridges boundaries and may not follow the pattern geometry as in the case of actin filaments. At a shallow depth of only 14 nm and groove distances from 1 μm to 4 μm, neurons showed a parallel or perpendicular orientation to the groove direction.[42]

Other structures taken into consideration are those with a curvature. Introducing a structure with a curvature has the purpose of reproducing the specific curvatures of 3D brain structures like blood vessels, or myelinated bundled fibers. Sub-micrometric (150-400 nm) and micrometric fibers (up to 500 μm) can guide neurons along the tube's long axis. Noteworthy, small curvatures provide the largest discriminative effect between axon and dendrite outgrowth.[129] This happens because axons possess a higher tensile stress than minor processes on curvatures. A hypothesis by Siechen et al. proposed that the mechanical tension is the key factor for stabilization of axonal branches and can control signal modulation of synaptic contacts.[130]

Isotropic topography

In case of isotropic patterns the cell-surface interactions are much more complex. Surface roughness can also have an impact on cell adhesion and development. Artificial growth conditions obtained by micro- or nanopillared surfaces can reveal neuronal properties that would be hidden in a more conventional context. Therefore, it is important to create pseudo 3D environments when culturing neurons on pillars.[131]

Even a simple increase in the surface roughness can already enhance cell adhesion and viability in comparison to flat substrates. For 20-70 nm average roughness of Si substrate, no neuro-adhesive coating was needed for a healthy neuron culture (5 DIV). Interestingly, if the roughness varied over the surface, the neurons would even migrate to the part of the surface with a higher roughness.[132] Similar results were obtained from cortical neurons cultured on Si surfaces with three different roughnesses: 18, 64, and 204 nm. Best neural adhesion occurred on Si wafers with a surface roughness in the region of 64 nm.[133] However, if the substrate was gold, the neuronal adhesion was not promoted. Cell preferentially adhered on flat substrates rather than nanorough gold surfaces.[134] Going one

step further, to vertically grown nanowires, the biocompatibility of material-based nanowires including GaP, gold, Si, Ge, SiGe, and GaN for hippocampal neurons was tested. All materials showed a good biocompatibility. In some cases a complete penetration of cells by nanowires, without any coating was observed.[135,136] Taking advantage of the nanowire cell-penetrating ability, the substrates were also used to deliver exogeneous biomolecules into cells.[137] Increasing the diameter of these vertical nanowires (change in the aspect ratio) resulted in a drastic effect. The neurons were observed to navigate only on the top of the structures.[138] However, the axons extend to the bottom surface if the distance between the structures permitted such growth. More importantly, these neurons showed axonal elongation and differentiation earlier than those grown on flat silicon surfaces.[51] Accelerated neurite outgrowth and cell differentiation was observed on periodic structures with a pitch in range of a few microns down to sub-micron ranges.[39-41] Similar neuronal features have been observed on concave and convex surfaces created by closely packed silica beads monolayer when the periodicity was larger than the size of filopodia (200 nm).[39] Using anodized aluminum oxide (AAO) nanostructures, Choi et al. observed a threshold roughness that elicits developmental accelerations. Nanostructures with a pitch of 400 nm had an accelerating effect on neuronal polarization of primary hippocampal neurons, but not those with a 60 nm pitch. This indicated that neurons could not distinguish nanotopography with a pitch smaller than 60 nm from flat surfaces.[139] The accelerated neurite elongation and neuronal polarization observed still requires a molecular understanding. One of the hypothesis refers to the discontinuous adhesive path associated with all these microenvironments. In this way actin patches between which neurites might build mechanical forces are formed.[47] In case of pillar structures cells forms periodic actin rings along the axon.[48] It is also known that the axon elongates faster (relative to the other neuronal processes) since it has the highest tension.[49] The second hypothesis relies on a possible channeling effect provided by topographies. This reduces the time required for the growth cone decision–making and consequently might trigger a faster elongation rate.[47,51] However, a comprehensive model that explains the axon elongation should refer to all surface guidance cues: chemical, mechanical, and topographical cues. Kerstein et al. introduced such a model that considers the growth cone's traction forces. The forces generated by the F-actin retrograde flow are balanced by pushing forces and the cell migrates in the direction of the strongest substrate force. The strength of the traction forces generated by the cells and the growth cones increase on more rigid substrates due to integrin activity regulation, internalization and adhesion complexes formation. Fewer and shorter cell-substrate contacts on rigid and nanostructured ECM disrupt the clutching forces. This induces advancing protrusions at the leading edge of the growth cone and rapid outgrowth.[50]

Although, the mechanism behind cell-nanostructures interactions are not fully understood, these effects are already exploited in the design of implants. Implementation of topographic surfaces into neural interfaces was introduced as a promising approach to

regulate cell functions *in vitro* and improve performance of electrophysiological devices. For example, sub-micron structure arrays with spines, rods, or mushrooms shape were employed for improving cell adhesion to microelectrodes and creating neuronal networks, which can be used for electrophysiological devices.[140]

2.3 Selection of appropriate 3D materials

Recent developments in nanotechnology can improve organization and operation for a better understanding of the nervous system and for the development of future neural technologies. Materials for cell cultures studies need to present acceptable chemical and physical properties to promote biocompatibility. Ideally the materials should have the approval of the Food and Drug Administration (FDA). Synthetic materials offer several benefits, such as a favorable cell response, controllable chemical composition, tunable physical and mechanical properties, simplicity of synthesis and processing, and compatibility with various fabrication techniques.[9] There has been substantial progress in the fabrication of nanostructured 3D surfaces composed of various synthetic materials. Two examples of synthetic materials are described here, since they are in a close relation with the topic of this thesis: gold nanocone arrays and Au-SiO_2 hybrid spheres. The gold nanocone arrays present various geometries and were found to induce a neurite outgrowth of rat primary cortical neurons. The geometry of nanocone arrays including height and periodicity were simultaneously controlled by the size of polystyrene (PS) beads from 0.2 µm up to 2 µm and the etching time. The elongation of neurite was quantified for all dimensions and a maximization of neurite length was obtained on the nanocone structure with a pitch of 1 µm. Also, detailed neuron-nanocone interfaces were observed by SEM and FIB-SEM cross-sections. Interestingly, the cell bodies attachment only on the tips of nanocones without engulfment (Figure 2.7a, b). Following this results, a possible mechanism for neurite outgrowth was proposed. This correlates the morphological similarities of the nanocone structures to the neuronal processes, the available contacting area on the top of nanocone arrays for cell adhesion, together with the mechanical tensions which apply to the cell body and neurites.[41] The second material represent the hierarchical micro/nanostructured Au-SiO_2 spheres where 500 nm–1 µm sized SiO_2 spheres decorated with 5-10 nm sized Au nanoparticles on the outer surface. The Au nanoparticles act as attractive cues in a 3D space due to a ligand modification (Figure 2.7c, d). Accordingly, Au nanoparticles on SiO_2 spheres ensured an efficient and biocompatible hybrid structure with possible application in neuroengineering. Other application could be drug delivery since the FIB-SEM showed cellular engulfment of the hybrid particle.[141]
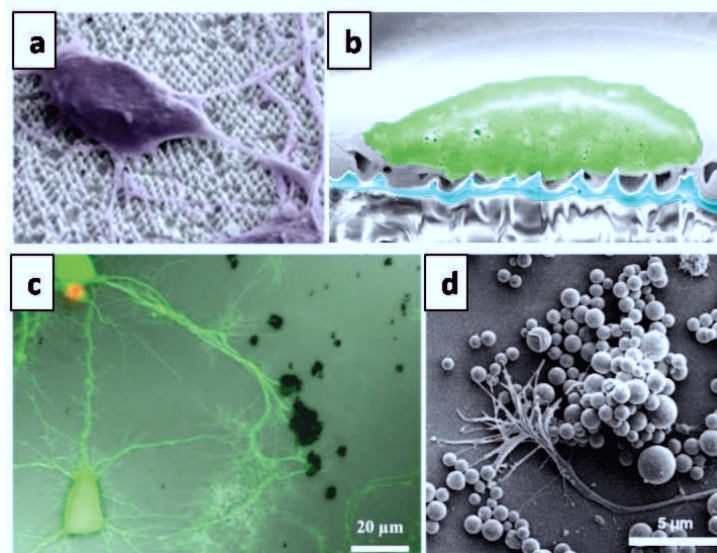
Figure 2.7. a), b) Gold nanocone arrays as a supporting substrate for neural culture. a) SEM image of a neuron on the gold nanocone array. b) FIB cross sectioning image showing the cell body and the nanocone interface.[41] c), d) Au-SiO$_2$ hybrid material on a flat surface can enhance the surface nanotopography and chemical cues for better neuronal attachment and guiding. c) Fluorescence image of neurites extending and attaching to the Au-SiO$_2$ spheres specifically. d) SEM characterization of a growth cone interaction with hybrid material.[141]

Finally, among all the materials used in literature, two materials are relevant for this thesis and are introduced in detail: OrmoComp and parylene polymer.

2.3.1. OrmoComp polymer

OrmoComp is a member of the inorganic (Si–O–Si)/organic hybrid polymer Ormocer family. Ormocer materials present exceptional chemical and thermal stability due to cross-linking of both organic and inorganic components. The chemical composition of these hybrid materials includes urethane- and thioether (meth)-acrylate alkoxysilanes, with strong covalent bonds between the ceramic and polymer components. The Young's modulus values of Ormocer materials varies between 11 to 17.000 MPa depending on the concentration of organic and inorganic network elements, the lengths of the groups that attach the organic and the inorganic crosslinking sites, and the concentration of filler materials. Ormocer-based matrix components and Ormocer-based light-curable dental composites have been used in restorative dentistry since 1988. Recently, Ormocers materials have also received increased interest from the biomedical community. Biological assays, including the ISO 10933–5 cytotoxicity assay, have shown that Ormocers materials

are nontoxic and biologically inert.[10] Beside these advantages, OrmoComp was used to fabricate controlled 3D cell culture microenvironments. Two-photon polymerization (2PP) technique was employed to create three-dimensional devices from OrmoComp as an innovative rapid prototyping method for the fabrication of arbitrary micro- and nano-architectures for cell culture.[4,5–9] Ormocomp was shown to possess good protein binding properties in its polymerized state. Geometric parameters of scaffolds for three-dimensional cell culture can be adjusted for the special needs of the target cell types. For example, elastic 3D OrmoComp 400 mm^2 and 900 mm^2 beam squares arrays with different spacing (20 mm, 30 mm) were fabricated to investigate nuclear and total cell volume. This research demonstrated that fibroblast-like and epithelial cells displayed similar cell and nuclear volume in 2D and 3D micro-environments.[11] Moreover, using 2PP technique, two different photoresist composite-polymer scaffolds with distinct mechanical and protein-binding properties can be fabricated. Protein-binding Ormocomp cubes with $1 \times 1 \times 2$ μm dimensions were attached to protein-repelling frameworks composed of the polyethylene glycol diacrylate monomer. Cells cultured on these scaffolds specifically form cell-adhesion sites on the OrmoComp cubes. Thus, cell adhesion and consequently cell shape can be fully controlled in 3D.[12,14]

2.3.2. Parylene

Since the discovery of the manufacturing process in the mid-20th century, polyparaxylylene (parylene) applications have become wider in several industries: aerospace and aviation industry, electrical industry, automobile industry. Moreover, parylene is one of the most common polymers that has been already established in many clinical applications or in research and development and serves as a carrier or as an insulation material for neural implants.[16] In particular, parylene has been widely used in biomedicine and nanobiotechnology (stents, cardiac pacemakers, neural electrodes), and in high-fidelity micropatterning of biomolecules.[142] Parylene C poly(dichloro-p-xylylene), PPX is the most popular parylene type for use in biomedical applications, due to its well suited combination of electrical and barrier properties. Parylene C has a good biocompatibility (FDA-approved and passed the ISO 10993-1/FDA) regarding cytotoxicity, intracutaneous reactivity and long term implantation.[142,143] Its chemical and biological inertness, good barrier properties, slippery surface and its functionality as an electrical insulator made parylene C an ideal material as a substrate or an encapsulation material in bioelectronical devices and electrical implants.[144–148] Effective neural recording and stimulation have been demonstrated using electrodes coated with PPX polymer films.[17–20] Successful applications of parylene C are related to its unique properties which also include, pin-hole free coating in thin layers, exact detailing in substrate topography and ability to penetrate through complex substrates. Typical layer thicknesses are in the range of a few hundred nanometers to several micrometers, depending on the coating machine. Parylene deposition process can give

different structures through its output: bulk parylene (planar-PPX), columnar-PPX, or more complex architectures such as helical and concave shaped PPX.[21] Parylene layers are deposited in a vapor deposition polymerization process, using the parylene corresponding dimer. This dimer is heated up until it vaporizes and later on splits into a monomeric gas. Finally, the monomers go through the nozzle bombarding the cold surface and polymerize on the substrate. Planar-PPX has no texture and can be deposited on any solid surface as a conformal coating. In case of columnar-PPX, the deposition was developed using the oblique angle method[149], at 10°. Concave and helical PPX structures were also formed using the oblique angle method, but samples were rotated during the deposition. For helical deposition, the substrate is fully rotated with 1 rpm speed. If the substrate is rotated 180° in a clockwise direction, then rotated 180° in the counter-clockwise direction, or vice versa, at 1 rpm speed, the resulting structures are similar to concave shapes. This versatility can be used to provide the best possible substrate and coating material for medical devices. Also, the structured PPX polymers have a large surface-to-volume ratio where the available surface area increases by over two orders of magnitude in relation to the bulk material (estimated 50% porosity). The chemistry can also be controlled, creating a possibility to engineer structured PPX from many combinations of monomers that have desired functional groups.[21] Furthermore, it has been demonstrated that anisotropic textured surfaces of columnar-PPX act as engineered ratchet surface. This ratchet mechanism has pinning and release functions. If the substrate is held 90° perpendicular to the ground, the pinning direction will hold a droplet at a critical volume whereas the same amount of water droplet will slide off the release direction. The substrates which presents ratchet surface can transport droplets unidirectionally, similar to butterfly wings and ryegrass leaves.[150] Capturing these natural features in biomimetic surfaces was actively used for cell culture, especially neuronal culture. Beighley et al. demonstrated that the columnar-PPX unidirectional surface can bias axonal growth. A unidirectional polarity of neurons and control of outgrowth direction of axons could be achieved at low cell densities.[22] Furthermore, Spedden et al. measured anisotropy in axonal outgrowth with the asymmetry in the growth cone surface coupling present due to variations in the ratchet topography. Different asymmetry parameters were investigated and a strategy to control neuronal growth showed that the asymmetry in the strength of cell-surface interactions is directly proportional to the asymmetry in the surface ratchet.[23]

2.4. Characterization of substrate surface and cell development

In the following subchapters, common techniques for the characterization of substrates and the interaction of cells with substrate topographies will be reviewed. These techniques include profilometry, atomic force microscopy, scanning electron microscopy, focus ion beam, and fluorescence microscopy for monitoring cell responses.

2.4.1. Profilometry

Profilometry allows the characterization of surface profile and roughness using a stylus or a laser.[151] Compared to other techniques, a profilometer does not need a special surface preparation and can be used for various materials. Compared with AFM characterization, a profilometer allows a large area scan in a short time. The stylus is moved around the surface by a motor and connected at one end to a transducer. The resulting height profile is then represented on a computer screen. The resolution profile depends on the diameter of the ball-tip place at the end of the stylus. In this study, the diameter of the ball was 12.5 μm. During measurements two types of errors can occur: stylus tilt error and stylus tip radius error. For an accurate measurement the stylus needs to be calibrated for each measurement. The stylus tilt error can appear by an improper alignment. In case the surface is curved, the stylus tip error will be unavoidable.

2.4.2. Atomic force microscopy (AFM)

AFM measures the sample surface morphology, roughness, chemistry and mechanical properties at a high resolution, down to the nano scale. Main parts of an AFM are the laser, cantilever, piezo-, and photo-detector. The cantilever has a sharp tip mounted on a lever. The cantilever is moved relative to the sample surface and bends under the force between the tip and the surface atoms. The cantilever deflection is detected by the photodiode via a displacement of the laser beam, which is reflected at the tip of the cantilever back during scanning. The signal received by the photodiode is processed by a computer and transferred into a morphology image. AFM operation is usually conducted by one of the following three modes: contact mode, non-contact mode, and tapping mode. In contact mode, the tip is brought into contact with the surface and the contour of the surface is measured using deflection of the cantilever at a given position. Contact mode is used for hard and stable samples and can create a high resolution image. In case of very soft specimens, the shear force generated by the tip may cause damages to the sample or atoms/molecules can be pulled out from the surface. For these soft samples, tapping mode can be used. The tip touches the surface only intermittently, because the cantilever is stimulated to vibrate near its resonance frequency (Figure 2.8). The oscillation amplitude is maintained constant by a feedback loop. In the non-contact mode the tip of the cantilever does not contact the sample surface. As in the case of the tapping mode, the cantilever is oscillating near its resonance frequency, brought into proximity of the surface, however without touching it. A constant distance is maintained by an electrical feedback loop. AFM characterization encounters several limitations such as restricted image size, slow scan speed, and imaging artifacts.[152]
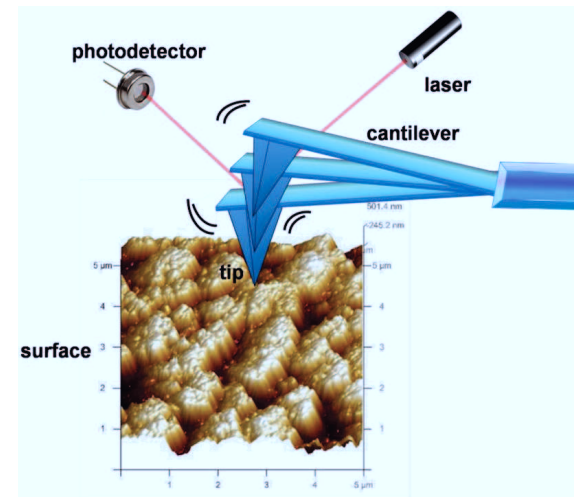
Figure 2.8. A schematic diagram of an AFM cantilever in motion during tapping mode.

2.4.3. Contact angle measurements

Contact angle measurement is a non-destructive, macroscopic technique used to characterize the free energy of a surface. A liquid drop deposited on a solid surface will form a contact angle (θ) at the interface between liquid-vapor and solid-liquid. If the liquid is water, then the surface provides information on the wettability of a solid. The angle, θ, at which the drop of water rests on the interface is measured (Figure 2.9). If θ = 0, the state is defined as complete wetting, any angle higher than 0 means that the surface presents a partially wetting equilibrium state. This wetting is described by Young's equation:

$$\gamma^{sv} = \gamma^{sl} + \gamma^{lv} \cos\theta$$

,where γ^{sl} denotes the interfacial energy of the solid-liquid, γ^{lv} the interfacial energy of the liquid-vapor, and γ^{sv} the interfacial energy of the solid-vapor. Changes in the interfacial energy variables result in changes in the measured contact angle. Contact angle less than 90° characterizes hydrophilic surfaces. Surfaces are considered as being hydrophobic, if the contact angle is higher than 90°, and superhydrophobic if it is over 150°.[153]
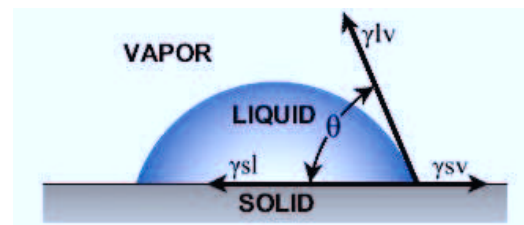
Figure 2.9. Contact angle (θ) of the three phase system solid/liquid/vapor with the interfacial energies of solid/vapor γ^{sv}, solid/liquid γ^{sl} and liquid/vapor γ^{lv}.

In the case of micro- and nanoscale modifications of substrate surfaces, other wetting models can be used to predict how the liquid is interacting with the sample surface. The most common models used are: Wenzel and Cassie-Baxter. In both of these models, surface roughness is taken into account. Wenzel model assumes there is no air underneath the droplet, and all pores are in complete contact with the water droplet (Figure 2.10a).[154] Cassie-Baxter model assumes that the surface roughness traps air pockets beneath the droplet. In this case, the water drops do not penetrate into the nano- or microstructure of the surface and therefore easily roll off (Figure 2.10b).[155] One example that corresponds to the Cassie-Baxter model are the surfaces of the lotus leaf or *Cicada orni*. The drop can also partially penetrate the surface as illustrated in Figure 2.10c.
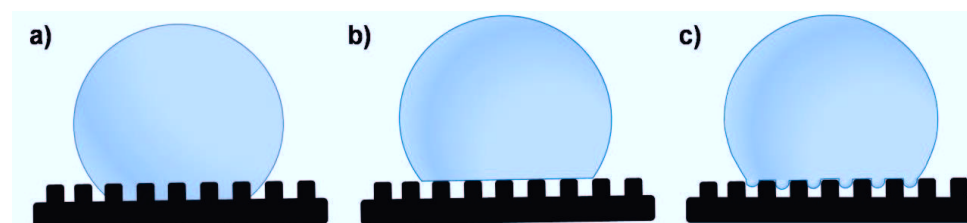
Figure 2.10. Models for wetting states on nano- and micrometer scale. (a) Wenzel wetting state. (b) Cassie-Baxter wetting state. (c) Hybrid wetting state where the liquid can partially penetrate air pockets in the surface.

2.4.4. Scanning electron microscopy (SEM)

The SEM is one of the most widely used tools in science for imaging surfaces of bulk samples using a finely focused beam of energetic electrons. One of the main limitations to resolution is the beam diameter, which can typically be demagnified to around 1-5 nm in high-resolution systems. The beam is generated from the electron gun and focused through the anode aperture (disk). Afterwards, the beam is demagnified through a series of electronic condenser lenses and a final objective lens. Scan coils are responsible for scanning the beam across the specimen surface. Magnification is produced by reducing the scan area on the specimen. Since the scanned area on the computer monitor stays the same, reducing the scanned area on the specimen increases magnification. Various signals are generated through the interaction of this beam with the sample. These signals may be collected or analyzed with the application of appropriate detectors. Two types of electron scattering are of primary importance in SEM imaging: elastic and inelastic scattering. Elastically scattered electrons, backscattered electrons (BSE), arise when an electron beam passes close to the positively charged nuclei of the atoms in the specimen. The electrons are deflected without much energy loss. BSEs are used for mapping surfaces containing very fine features. They are highly sensitive to changes in specimen atomic number and can be used to map the chemical composition of a finely polished specimen. Inelastic scattered

electrons experience a large loss of their energy when interacting with the surface. In this case secondary electrons are produced (SE). SEs are used to image surface topographies. The relatively low energy of SE restricts their mean free path to depths near the surface (10 nm). Other electron beam excitation products are Auger electrons, X-rays, photons which result from electron-specimen interactions. For example, when incident electrons excite core electrons then outer shell or valence electron drop down to the core levels and fill the vacancies. Excess energy is released as an x-ray, which is characteristic of the atomic number. Energy-dispersive X-ray spectroscopy (EDS) detector is used for elemental analysis or chemical characterization of a sample. Since each element has a unique atomic structure this will allow a unique set of peaks on its electromagnetic emission spectrum. Although the lateral resolution of EDS is limited in comparison to imaging SE, the technique was used in this thesis for a qualitative analysis of the chemical composition of specific specimens.[156]

2.4.5. Focus Ion Beam-Scanning electron microscopy (FIB-SEM)

Combinations of high resolution SEM and FIB have become powerful tools for material research. The potential of this technique ranges from the top-down structuring (etching or deposing of fine structures) to topographical characterization of the specimen. In a FIB workstation, a focused beam of gallium ions is used for ablation or deposition of material on the surface of a specimen. Secondary ions (i^+ or i^-), neutral atoms, and secondary electrons are produced when the beam of gallium ion hits the sample surface. An image can be processed by collecting the signals given by either ions or secondary electrons. Using a high beam current, material can be removed from the specimen. Cross-sections of a sample can be prepared with such methodology. In this thesis, not only nanostructure surface profiles were investigated but also cell-substrate interfaces. For biological samples a deposition of Pt was performed via ion beam induced deposition to compensate for surface charging and to protect the fragile components of the cells. The gas is introduced by a nozzle, which adsorbed on the surface of materials when the ion beam hits the surface. The secondary electrons will break the chemical bonds of the adsorbed gas molecule, which decomposes into volatile and non-volatile components. The non-volatile components of the gas deposit on the target area. FIB slice by slice cutting technique was used for milling, followed by high resolution SEM imaging. The slice by slice preparation technique is carried out by stepwise material ablation in only one direction to create parallel cross-sections of the sample. During this stepwise preparation process, cell-substrate interactions as well as cellular-nanostructures contacts can be studied. With the resulting stack of images it is possible to generate a 3D reconstruction of the observed object at high resolution.[27,31]

2.4.6. Fluorescence microscopy

In this thesis, fluorescence microscopy was used to study cell's viability and response to nano- and microstructured surface. Through fluorescence microscopy specific cell components can be visualized. The selective visualization is facilitated by specific binding between fluorescently labeled antibodies and the corresponding antigens. Basic function of fluorescence microscopy is to irradiate a sample with light of a specific wavelength, specific for a fluorophore adsorption. Then, the fluorescent marker emits light of a longer wave length. The fluorescent image is processed by separating the sample fluorescence from the excitation light. A common technique to image fluorescently labeled samples is the wide-field fluorescence microscopy. In this system a light source, usually a mercury lamp or an arc lamp, passes light through filters cubes. The microscope can accommodate several different cubes so that a variety of fluorophore wavelengths can be observed from a single sample. The light passes the excitation filter at desired wavelengths, and reaches the beam splitting dichromatic mirror. The mirror reflects the shorter wavelengths, while the longer wavelengths can pass through. Fluorophores in the labeled samples are excited and their emission light passes through the dichromatic mirror into the emission filter. The emission filter has the purpose of removing any residual excitation light that passed the mirror. However, wide-field fluorescence was shown to be limited for thicker samples. Secondary fluorescence emitted by the sample away from the region of interest can interfere with the focused image. This results in a low contrast and with no possibility to render 3D sample projections.[157] The elimination of light out of the focal plane can be done either optically (confocal) or mathematically (ApoTome). In this thesis, imaging of thicker specimens was done using the ApoTome function. For this, a grid was added in the illumination pathway of the conventional fluorescence microscope. During imaging, the grid changes its position and three raw projected images are obtained. The system then calculates the optical section from the three images and removes the out of focus light. Focus information is valid when the grid is visible. If not, that signal corresponds to out of focus light and is removed from the final image. Z-stacks can be calculated from ApoTome images by sequentially collecting multiple optical sections of the sample. A 3D image or movie of the sample can be built in this way.[158]

2.5. Micro- and nanofabrication

Topographical substrate modification includes treatments or patterning that change the physical aspect of the material surface. Micro- and nanoscale fabrication of structures with high precision plays a crucial role in the advancement of micro- and nanotechnology and neuroscience. Several alternative approaches towards nanostructures fabrication have been explored in the last years. These techniques include: deep-UV projection lithography, electron beam lithography (EBL), microcontact printing (or soft lithography), nanoimprint lithography (NIL), phase mask lithography, interference lithography, direct laser writing,

direct ink writing., The techniques that are used in the scope of this thesis and therefore further described are EBL and NIL.

2.5.1. Electron beam lithography (EBL)

EBL is a high resolution patterning technique where high energy electrons are focused to a fine beam to locally expose electron-sensitive resists. Energies of the electron beam (e-beam) range from 10 to 100 keV. For EBL no physical mask is required since the system software can be used to control the e-beam location. The e-beam is scanning across the entire sample (wafer) and transfers information into the resist according to specifications. The resolution of EBL depends on two characteristics: beam size and proximity effects. Beam sizes down to a few nm are used, since the EBL is a pixel-to-pixel serial technique. Proximity effects are primarily a mechanism of e-beam scattering in the resist, electron backscattering from the substrate, and the scattering of secondary electrons ejected from the resist. EBL can also be controlled by the energy and dosage (C/cm^2) of the external electric and magnetic fields. Choice of resist, exposure dosage, electron energy, feature density, *etc.*, contribute to the best obtainable resolution of EBL. The main drawback of EBL is its low-throughput since it is a serial direct-writing method and its high machine costs. For this reason, all structures in this thesis were replicated using NIL.[159]

2.5.2. Nanoimprint lithography (NIL)

NIL is considered a promising nanopatterning method with low cost, high throughput and high resolution for producing large-area micro/nano scale patterns, complex 3D structures, as well as high aspect ratio features. The principle of NIL is very simple. A rigid mold, created by other fabrication methods (here EBL) is used to emboss the pattern of the mold into a thin layer of an appropriate material. Inorganic materials, polymers, and biomaterials are used in the NIL process. There are different types of NIL, but two of them are most extensively used: thermal nanoimprint lithography (similar to hot embossing) and UV-NIL (use in this thesis). In case of thermal NIL the material is heated above the glass transition temperature so that it becomes deformable and able to replicate the topographic features of the mold. Sample and mold are pressed together at elevated temperatures and high pressures. After cooling them to room temperature, sample and mold are separated. The reverse pattern of the mold will be obtained on the sample. For an easy demold it is necessary to treat the surface of the mold with special lubricant (*e.g.* fluorinated silanes) to prevent sticking of the target substrate material to the mold after cooling. In UV-NIL, a substrate is coated with a viscous liquid-phase UV-curable material. The polymer is pressed against a mold and cured by irradiation with UV light. Because the materials typically patterned in UV-NIL have lower viscosities than those used in thermal NIL, feature resolutions are much higher and features with large aspect-ratios can be readily produced.[160]

3. MATERIALS AND METHODS

This chapter introduces the techniques used in this thesis. All materials, reagents and solution specifications are shown in Appendix B. Firstly, is presented the top-down fabrication of Si/SiO$_2$ molds performed in a class 100 cleanroom (permanent control of particles, humidity, and temperature). Then, surface modification is described for the mold replication process in order to obtain polymer substrates for cell culture experiments. A second approach (bottom-up) for the fabrication of polymer samples with nano-topographies is presented in detail. Consecutive paragraphs will focus on surface modification and primary neuronal cell culture on polymeric surfaces and control samples. For the cell-substrate interaction characterization techniques such as live-dead staining and immunofluorescence are provided. Lastly, cell preparation for electron microscopy is described for two types of protocols: critical point drying and resin embedding.

3.1. Substrate fabrication

Substrates for cell culture experiments were fabricated under two different approaches: top-down and bottom-up. Isotropic and well defined substrates were obtained using the top-down approach. Bottom-up fabrication was chosen to produce asymmetric nanotextured polymeric substrates.

3.1.1. Symmetric nanostructured fabrication (top-down approach)

3.1.1.1. Mold production

Molds with structured patterns made of rigid materials were used as an inexpensive and convenient route to fabricate nanostructured materials. In this thesis, the molds are made of Si/SiO$_2$ wafers and used for polymer replica fabrication by UV-NIL.

All Si wafers were purchased from Si-Mat with the following characteristics: 4 inch diameter, n-type, <100> orientation, 1-10 Ω cm, and 500-550 µm thickness. The wafers were oxidized to obtain a defined layer of SiO$_2$ (dry oxidation, Centrotherm CLV 200 oxidation chamber). Polymethylmethacrylate (PMMA, AR-P 669.04) resist was employed for electron beam lithography. Layouts were designed using CleWin 4 program. According to the layout EBPG 5000plus (Vistec B.V., now Raith B.V.) electron beam writer was used to transfer the pattern onto the resist. An acceleration voltage of 50 kV was chosen. SiO$_2$ was etched with CH$_3$/SF$_6$ plasma using reactive ion etching (RIE, Oxford Instruments). The final resist removal was done in the RIE chamber using O$_2$ plasma. Detailed fabrication flow is described in Chapter 4 and recipes can be found in Appendix C.

3.1.1.2. Surface modification for replica fabrication

The mold surface was passivated to facilitate removal after the replication process. For this purpose, molds were cleaned and activated using O_2 plasma (Plasma surface technology-Pico, Diener electronic) for 2 min at 200 W power and 1.4 mbar pressure. After oxygen plasma treatment, the contact angle was well below 10° (hydrophilic surface). Alternatively, the surface was activated by immersing the sample in a piranha solution (30% H_2O_2:96% H_2SO_4 = 1:4) for 1 min. The wafers were then transferred in an argon atmosphere glove box (99.99% argon atmosphere, MBraun) equipped with a desiccator for the silanization step. 40 µl of trichloro(1H,1H,2H,2H-perfluorooctyl)silane (FOTCS) was transferred to the gas phase at a pressure of 45 mbar and deposited on the surface for 1.5 h. The FOTCS molecules bind covalently with -OH groups of the SiO_2 surface. Therefore, the surface needs to be activated before silanization. The surface modification lowers the surface free energy and enhances hydrophobicity inducing a water repellent behavior. After surface modification, the wafers where reintroduced to the cleanroom and rinsed in acetone, isopropanol and water cascade before replication.

3.1.1.3. OrmoComp double replication

4 inch quartz wafers (thickness 525 ±10 µm, Plan Optics AG) were used as substrates for the OrmoComp resist coating. The quartz wafers were baked at 200°C for at least 10 min in order to remove any organics/water from the surface. An adhesive promoter, OrmoPrime, was deposited to facilitate adhesion of the OrmoComp polymer. OrmoPrime was spin coated at 4000 rpm for 45 sec and baked for 5 min at 150°C. Then, OrmoComp solution (OrmoComp:OrmoThin = 1:12) was used for final coating of the quartz wafer at a speed of 4000 rpm for 45 sec. Soft baking of the hybrid polymer was done at 80°C for 2 min. Nanoimprint lithography (NX-2000, Nanonex Corp) was used to produce the quartz/OrmoComp replica. The Si/SiO_2 mold and the quartz/OrmoComp wafer were placed together between two silicone foils and compressed by an air cushion principle. A pre-imprint lasting 1 min at 6.9 bar (100 psi) was necessary for stabilization and homogeneity of the process. The main imprint was performed for 5 min at 34.5 bar (500 psi), followed by a UV irradiation (365 nm of emitted light wavelength) for 1 min (Figure 3.2a). All the imprint processes were conducted at room temperature. One important challenge NIL still faces represents the ability to cleanly and easily separate the mold and the OrmoComp replica. In order to overcome this challenge, the wafers were separated softly with blades and isopropanol (which lowers the interfacing adhesion). The final step of replica fabrication was the hard baking of the quartz/OrmoComp replicas in an oven at 150°C for 16 h (Figure 3.2b).
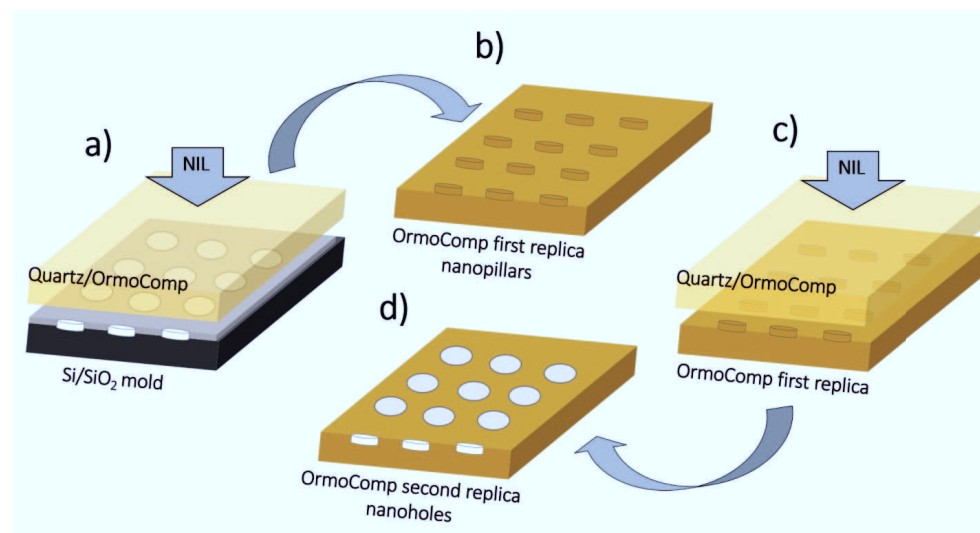
Figure 3.2. Double replica fabrication of OrmoComp hybrid polymer using NIL. Nanopillar structures are obtained after imprinting and UV curing of Si/SiO$_2$ molds and quartz/OrmoComp polymer substrates (a, b). A second replication using the same fabrication protocol is depicted in c), d) in which the first OrmoComp replica was used as a mold.

In order to obtain the second replication of the nanostructures (nanoholes), the first Ormocomp replica was used as a mold (Figure 3.2c, d). This aspect is important since the aim of fabrication was to employ the original structure and replica with the same surface chemistry for cell culture studies. First, OrmoComp replica was activated by O$_2$ plasma for a short time (30 sec) at 200 W and 1.4 mbar. Then, the FOTCS silanization was performed with the same parameters as for the Si/SiO$_2$ mold. The rest of the process is the same as presented above.

3.1.1.4. Parylene replica

Parylene C replicas fabrication were not obtained by means of any lithography steps. The Si/SiO$_2$ mold wafer was activated and a silanization step was performed as presented above. Figure 3.3 shows the steps of parylene replica fabrication. After silanization, a parylene film was deposited directly on the Si/SiO$_2$ mold with a thickness of 13 μm (PDS 2010 E Labcoter 1, details about parylene film deposition in Appendix C). The parylene films were cut by a sharp scalpel into pieces of 1 x 1 cm having nanostructured or non-structured areas. The film was peeled off using fine tweezers (Figure 3.3a). A glass slide was used as a substrate for spin coating PDMS 1:10 polymer solution at 3000 rpm for 45 sec. The peeled-off parylene films were placed with their backs (nanostructures up) on the prepared PDMS (Figure 3.3b).
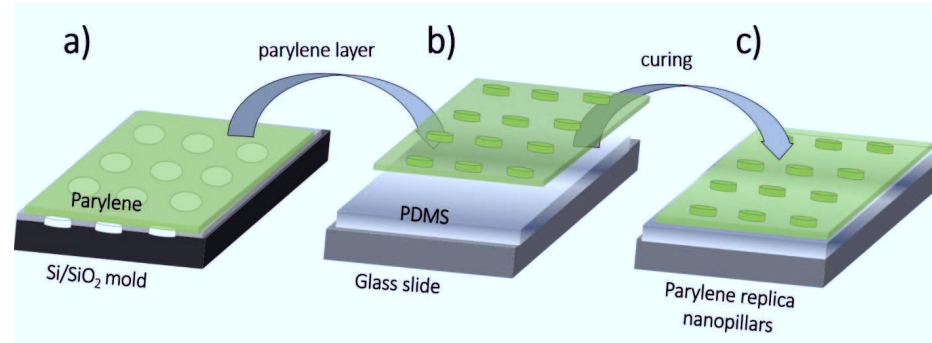
Figure 3.3. Parylene replica fabrication. a) Parylene film was deposited on the silanized Si/SiO$_2$ mold. b) The nanostructured areas were cut and placed on PDMS. After curing the parylene replica was obtain (c).

This method allows for a proper transfer of the parylene film with no wrinkles. Finally, the nanostructured parylene/PDMS stack was baked for 12 h at 60°C for PDMS curing (Figure 3.3c).

3.1.2. Asymmetric nanostructured fabrication (bottom-up approach)

The deposition process of columnar PPX films is illustrated in Figure 3.4 and was performed at Gazi University, Turkey. Si wafers (MT I, <001> crystallographic orientations) and glass slides (Isolab) were used as substrates for PPX nanostructured and flat film production. The substrates were cleaned by sonication in acetone and ethanol for 5 min each. A second surface cleaning was done in a solution of H$_2$SO$_4$ and H$_2$O$_2$ having a volume ratio of 3:1 at 70°C for 1 h. Substrates where rinsed with water and dried in N$_2$ gas. A UV/ozone treatment was applied for 10 min. Subsequently, the surface was modified by vinyltrimethoxysilane (1.0% (vol/vol) in toluene for 3h) to enhance the adhesion of the polymeric films. A detailed description of the experimental methods used for preparing parylene nanofibers using oblique angle deposition was reported by Gohkan et al.[161,162] Briefly, SCS-PDS2010 deposition system with a special nozzle for directing the monomeric vapor flux was used. Template free parylene films were deposited using dichloro-[2,2]paracyclophane as the precursor (~0.3 g) into an evacuated sublimator chamber. These monomers were then evaporated at ~175°C and converted to radical monomers by pyrolysis (~695°C). These radicals undergo polymerization on the substrates under ambient temperature (Figure 3.4a). During deposition, the flux of monomeric parylene was directed onto the substrates at 90° or 10° angles. The tilt angle is important for morphology control, since the substrate manipulation during oblique angle deposition can be used to obtain a wide variety of morphologies.[21]
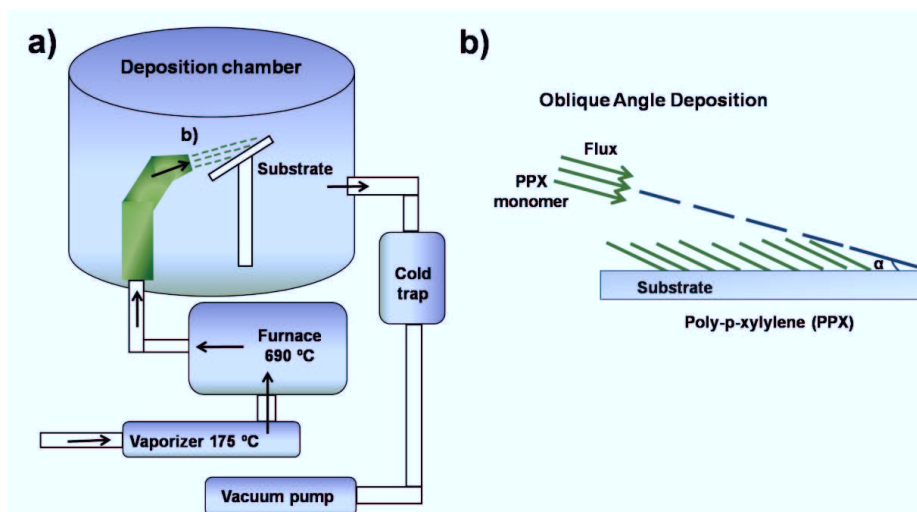
Figure 3.4. Schematic representation of oblique angle deposition of parylene C. a) Deposition of a PPX-derivative columnar thin film started with dimers and converted to a reactive vapor of monomers by pyrolysis. b) The deposition and polymerization has been performed at an oblique angle ($\alpha=10°$).[163,164]

Here, nanostructured columnar-PPX thin films were obtained on Si wafers and glass substrates under nozzle held at an angle $\alpha=10°$ (Figure 3.4b). For the deposition of planar films, coating system was operated in a normal configuration without using the nozzle to disperse the entering monomer vapor on substrates (perpendicular to the vapor flux).

3.2. Surface modification for cell culture experiments

Si, parylene, and glass cover slips substrates were processed for surface activation in an O_2 plasma chamber at 1.4 mbar pressure and 200 W power for 2 min. All the substrates prior to cell culture were sterilized under UV light (30 min, HS type, HERA safe) or dipped in 70% ethanol for 5 min. In addition, samples were coated with 10 mg/ml PLL diluted in Grey's Balance Salt Solution (GBSS) at room temperature for 1 h. Finally, samples were rinsed with GBSS shortly before cell seeding.

3.3. *In vitro* primary neuron culture

Primary cortical neuronal cultures were prepared by removing cortices from Wistars rat embryos at embryonic day 18.[95] The embryonic cortices were then immersed in hibernating solution for maximum 2 days before cell dissociation. Tissue dissociation was done enzymatically by incubating the cortices with 0.25% trypsin/ ethylenediaminetetraacetic acid (EDTA) in a Petri dish for 15 min at 37°C.
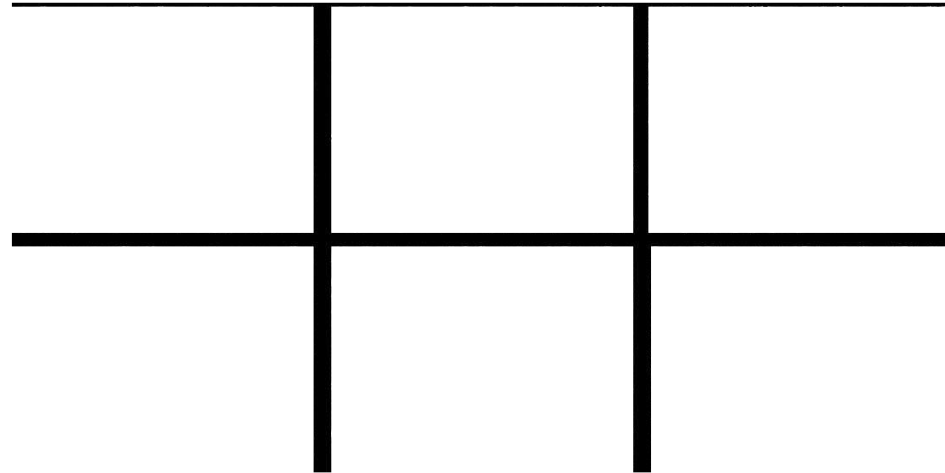
Figure 3.5. Primary cortical neurons *in vitro*: images of neuronal development from 3 h until 21 days after culture. Cells were seeded on glass cover slips, coated with PLL at a density of 2 x 10⁴ cell/ml.

After incubation, the solution consisting of tissue and trypsin/EDTA was transferred in a 2 ml plastic tube. The tissue was left to settle at the bottom of the tube and excess solution was removed gently. The neuronal pellet was diluted in Neurobasal medium with 1% (vol/vol) B-27 supplement, 0.25% (vol/vol) L-glutamine, and 0.1% (vol/vol) gentamycin antibiotic. Then, the tube was gently swirled by hand. This procedure was repeated 3 times. For all experiments a cell concentration of 2 x 10⁴ cells/ml was seeded. To calculate the cell concentration, a sample of re-suspended cells (10 μL) was extracted, diluted in 20 μL of supplemented Neurobasal media and 10 μL of trypan blue. This solution was placed in a cytometer (Neubauer chamber) to count live and dead cells. After counting, the remaining cells were re-suspended to a final concentration of 2 x 10⁴ cells/ml. Two to three hours after plating, the entire medium was replaced to remove cells that had not adhered to the substrates. Cells were kept at 37°C, 5% CO_2, and 100% humidity in the incubator. Subsequently, half of the media was exchanged with freshly-prepared warm (supplemented) Neurobasal® media. Typically, control cultures have been prepared on glass coverslips with PLL coating, and the cells were observed during maturation (Fig. 3.5).

3.4. Neuron staining

Fluorescent microscopy was used for visualization of cell viability, development, and morphological changes. Two different methods were used, depending on the experiment. For a simple and fast imaging of living cells, live-dead staining was performed by a calcein AM/ethidium homodimer assay. Protein specific staining was used to visualize the morphology of cell components such as axons and dendrites.

3.4.1. Live-dead staining

A standard calcein AM/ethidium homodimer assay was used to calculate the cell viability after 3 or 4 DIV. It is a two-color fluorescence assay that simultaneously stains live and dead cells. Cell viability is then calculated as the number of live cells divided by the total number of cells for each experiment. The calcein AM dye stains live cells and shows a strong green fluorescence (495 nm excitation wavelength and 515 nm emitted wavelength). Live cells have intracellular esterases that convert nonfluorescent, cell-permeable calcein acetoxymethyl to the intensely fluorescent calcein. Cleaved calcein is retained within cells. In case of dead cells, the ethidium homodimer enters damaged cells and is fluorescent when bound to nucleic acids. Ethidium homodimer produces a bright red fluorescence (excitation 528 nm/emission 617 nm) in damaged or dead cells. Before staining, cells were washed with preheated PBS at physiological pH. The live-dead assay was prepared in a 3 μM PBS buffer. The substrates were incubated for 15 min before imaging. The fluorescence images were acquired within maximum 1 h due to the dyes' toxicity (Figure 3.6).
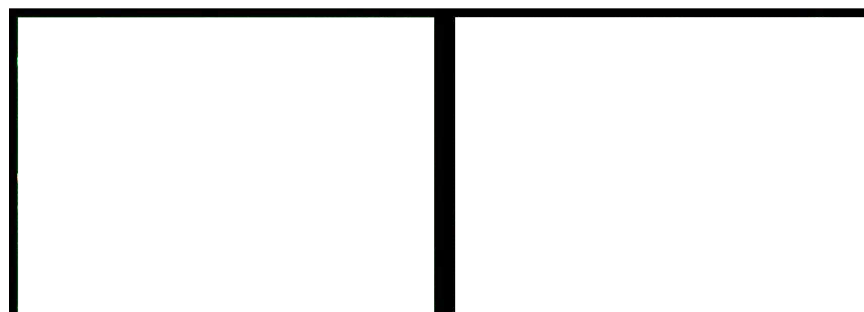
Figure 3.6. Live (green) and dead (red) staining of primary neurons after 4 DIV. a) Neuronal network cultured on typical PLL coated glass coverslips (control substrate). b) Fluorescent and DIC merge image of neurons interaction with structured pattern (2 μm diameter, 4 μm pitch, 100 nm high pillars).

3.4.2. Immunofluorescence staining

The antibody-based method of immunofluorescence staining is widely used to detect specific cell proteins. There are two types of immunofluorescence staining. Primary (direct) immunofluorescence uses a single, primary antibody, chemically linked to a fluorophore. The primary antibody recognizes the target molecule/protein and binds to a specific region. The attached fluorophore can be detected via fluorescent microscopy, by emitting at a specific wavelength of light once excited. Secondary (indirect) immunofluorescence uses two antibodies; an unlabeled first (primary) antibody that specifically binds the target molecule. Then, the secondary antibody, which carries the fluorophore, recognizes the primary antibody and binds to it. The protein of interest can be identified by the emission color in fluorescence microscopy. Multiple secondary antibodies can bind a single primary

antibody. Immunofluorescence can be used in combination with other, non-antibody methods of fluorescent staining, *eg.* DAPI.[165,166] In this thesis, only secondary immunofluorescence (indirect) was used in combination with DAPI and phalloidin staining. Before staining, all cell samples were fixed with 4% (w/v) paraformaldehyde (PFA) in phosphate buffered saline (PBS) for 12 min at room temperature. PFA is a polymerized form of formaldehyde that fixes tissues by cross-linking proteins, primarily the basic amino acid lysine.[167] Then, the samples were rinsed in PBS and a cell membrane permeabilization was done using 0.3% TritonX-100 in blocking buffer (BB, 2% bovine serum albumin and 2% heat inactivated goat serum diluted in PBS) for 15 min at room temperature. After rinsing again, blocking of unspecific bonding was performed over night by incubation with BB at 4 °C. After blocking, samples were washed three times and then incubated in primary antibody solution. Several different antibodies were used during the experiments. For cytoskeleton imaging two primary antibodies were used: against microtubule-associated protein 2 (MAP2, rabbit, 1:500 dilution in BB) and anti-β3 tubulin (rabbit, 1:500 dilution in BB). Anti-200 kD Neurofilament Heavy (NFH, chicken, 1:500 dilution in BB) and anti-Tau1 (mouse, 1:200 dilution in BB) were choose as axon specific primary antibodies. A drop of 70 ml of the antibody solution was applied to control coverslips and cell containing substrates (cells placed facing the droplet). The samples with primary antibodies were incubated for 1.5 h at RT in a wet and dark chamber. Afterwards, substrates were rinsed three times with PBS and incubated in secondary antibody solution for 1.5 h at room temperature inside a wet and dark chamber. All secondary antibody solutions contained Alexa Flour conjugated secondary antibodies in a 1:500 dilution in BB. The secondary antibodies were anti-rabbit for MAP2/β3 tubulin (Alexa Flour, AF 488), anti-chicken (AF 546), and anti-mouse (AF 546 or AF 633).

In some experiments, an additional phalloidin staining (emission wavelength 633 nm) of the filamentous actin (F-actin) was applied. Phalloidin binds and stabilize actin filaments and effectively prevents the depolymerization of the fibers. The incubation with phalloidin lasted for 45 min at 1:40 dilution in BB. Finally, 4',6-diamidino-2-phenylindole (DAPI) was used for all samples to visualize nuclear deoxyribonucleic acid (DNA). Usually, DAPI staining is applied together with the last antibody incubation in a 1:1000 in BB dilution. After immunofluorescence steps, substrates were rinsed once with PBS and twice with Milli-Q water before they were embedded in fluorescent mounting media and dried overnight. Fluorescence microscopy was performed using an ApoTome microscope (Carl Zeiss) and processed using ZEN blue software. Representative images of two secondary immunofluorescence staining (β3 tubulin-green, NFH-orange), non-antibody fluorescent staining (DAPI-blue, phalloidin-red), and DIC channels can be observed in Figure 3.7.
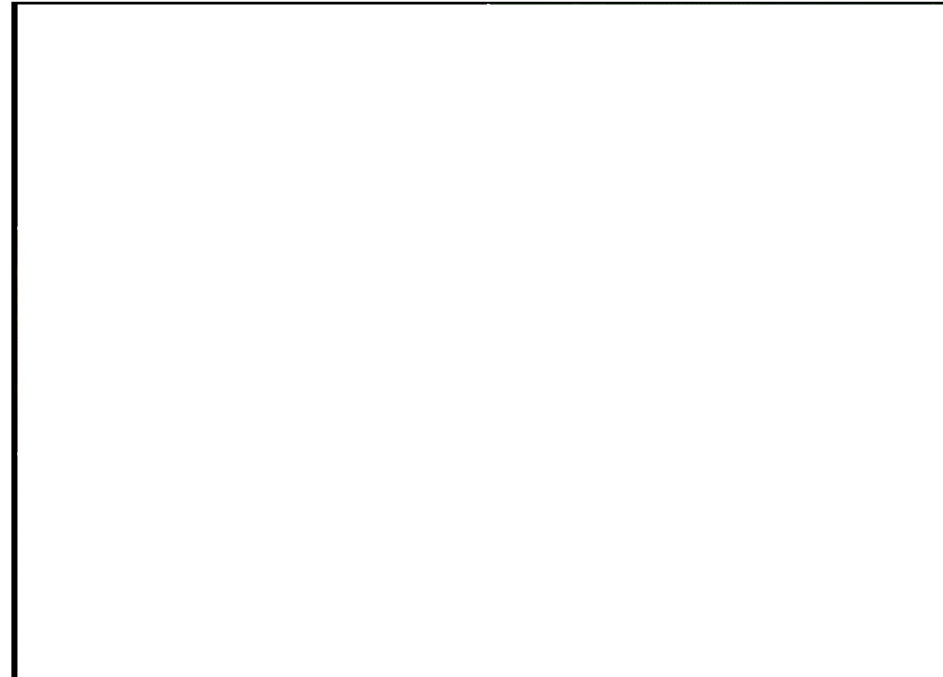
Figure 3.7. A representative immunostaining image of a cortical neuron on OrmoComp polymer substrate (100 height, 250 nm diameter, 1 μm pitch). The image is taken at the border between flat and nanopatterned surfaces after fixation. The cell is fluorescently labeled for: DAPI (blue), β3 tubulin (green), NFH (orange), and phalloidin (red). Scale bar: 10 μm.

Image J was used for analysis of cells including: soma area, neurite number, axon length, and axon branching. Images were manually analyzed with the free-hand tool or Neuron J plugin from Image J. Furthermore, axon initiation and path finding angles were investigated along with neuron guiding efficiency on specific substrates. Data was analyzed using Origin package. All data showed in the text are mean values ± standard deviation (SD). Plots were shown as columnar representation with SD bars or boxplots, Tukey type (median denoted as line and the mean as a square).

3.5. Sample preparation for electron microscopy

Technical fixation plays an important role in optimal electron microscopy investigations of biological specimens. In this thesis, two different approaches, critical point drying (CPD) and resin embedding, were utilized. We introduced the resin embedding method as an innovative procedure to prepare biological samples attached to planar substrates and substrates with 3D features for electron microscopy.[33] For this reason, the optimization steps are described in detail in Chapter 5, where a comparison between CPD and resin embedding method is presented as well.

3.5.1. Critical point drying technique

The samples were washed three times with warm PBS (37°C) followed by fixation with 3.2% glutaraldehyde solution in PBS (37°C) for 15 min at room temperature. Then, samples were rinsed with PBS and MilliQ water so fixatives' residues could be completely removed. Gradually, water was replaced with an intermediate medium (ethanol) starting from a concentration of 10% up to 95% (vol/vol) in MilliQ. Incubation in 10%, 30%, 50% ethanol solutions was done for 5 minutes at each step. Samples were then infiltrated in sequence starting with 70% ethanol solution for 15 minutes, followed by 90% and 95% for 5 minutes, 3 times repeated. In the end, samples were stored in 100% ethanol in a sealed dish at 4 °C. Samples were carefully transferred into the chamber of a critical point drying machine (CPD 030, BAL-TEC Company) filled with 100% ethanol. It is important that samples do not dry out during transfer. Once the samples are in the CPD chamber, the system is slowly cooled down to 10°C (typically 1°C/step). At this temperature, the ethanol is exchanged for liquid CO_2. The exchange process is repeated 10 times. Then, the chamber's temperature is increased until reaching a temperature of about 40°C. Simultaneously, the pressure is slowly increased. CO_2 in liquid form has typically a transition to vapor phase at around 31.1°C and 73.8 bar. After this transition, the chamber was evacuated and the cells were completely dehydrated.

3.5.2. Ultra-thin resin embedding method

In this subchapter, the second method of sample preparation using ultra-thin resin embedding is presented. Like in the case of the CPD method, the samples fixation and the dehydration was done with ethanol. For the resin protocol, a sodium cacodylate buffer [$Na(CH_3)_2 AsO_2 \cdot 3H_2O$] was used. The embedding polymer was freshly prepared each time by a mixture of Epon 812, DDSA, MNA, and DMP-30 solutions. A detailed preparation of resin embedding polymer is described in Appendix B. The samples were then gradually incubated in mixtures of ethanol and resin as listed in Table 3.1. At the end of the resin exchange, the samples were covered with pure resin.

Table 3.1. Incubation mixtures of ethanol-resin and corresponding times.

Ethanol : Resin	Incubation time
3 : 1	3 h
2 : 1	3 h
1 : 1	over night
1 : 2	3 h
1 : 3	3 h
100 % Resin	3h

The final step of the resin embedding method is the removal of excess resin surrounding the sample. The resin removal was done immediately after 3 h of pure resin incubation using absolute ethanol. A pipette with 5 ml or 10 ml was used to splash ethanol first on the back of the sample and afterwards on the substrate side where the cells adhered. A qualitative and quantitative analysis for this crucial step is presented in Chapter 5. Finally, resin polymerization was achieved by baking the samples for 24 h at 60°C.[33]

3.6. Neuron-surface interface characterization: SEM and FIB-SEM

In order to evaluate the interaction and interface between the cells and the surface, each sample was mounted on a typical electron microscopy stub using liquid silver paste. The mounting with silver from the top surface of the sample to the sample holder induces a conductive "bridge" that decreases the charge effects. For a complete elimination of charge effects, the samples were coated with a thin layer of iridium (15–30 sec deposition time, 15 mA current) via sputter deposition (K575X Sputter Coater, Quorum EMITECH). Samples were observed either with a single scanning electron beam (Magellan 400, FEI, and 1550VP, Zeiss) or, complementarily, with an electron and ion beam in a dual beam system (Helios 600i NanoLab Dual-beam, FEI). SEM pictures were taken from a top view and under different tilted angles using a detector for SE or BSE. Beam accelerations ranged from 3 kV to 10 kV.

For FIB cross-sections, the region of interest was first covered with a platinum protective layer deposited in two steps (Figure 3.8a). During the first step, a 0.5 μm thick layer of platinum was deposited via electron beam induced deposition (EBID) at 0° fixed stage. In the second step, 0.3-0.5 μm of platinum was deposited at 52° tilt via ion beam induced deposition (IBID). The deposition was performed with the respective beam perpendicular to the target area in both cases (Figure 3.8b). A first cross section was created by an ion beam milling procedure (at 30 kV and 0.23 or 0.74 nA) fixing a milling depth of 1 μm, nominally valid for silicon (Figure 3.8c). Finally, a fine polishing was

performed at 30 kV with a current of 80 pA (Figure 3.8d).[32] The imaging was done via the electron column using a detector for SE or BSE, both with a fix voltage of 3 kV.
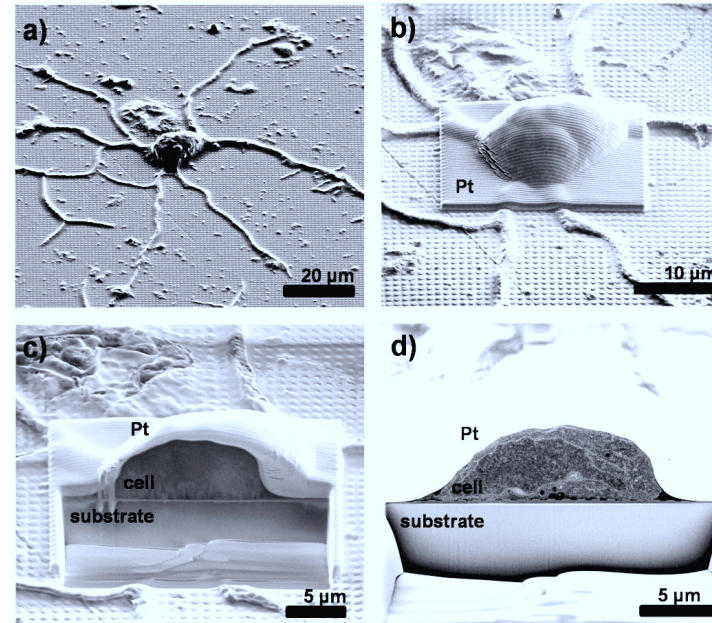
Figure 3.8. FIB cross section of a fixed, stained, and embedded neuron on a nanopatterned substrate. Example of a selected cell (a) covered with EBID (11 nA) and IBID (80 pA) platinum layers (b). Etched cross sections performed with a current of c) 0.74 nA, and a fine polishing with d) 80 pA. After cross-section, the cell-nanopatterned interface was imaged with high resolution SEM.

4. SUBSTRATE AND REPLICA FABRICATION

4.1. Design

In this thesis several mold designs were created using the program CleWin 4. The areas are described in Table 4.1 and were separated in three arrays:

- Arrays with a pitch double the diameter
- Arrays with constant pitch at increasing diameter
- Linear gradient

The pattern design was important to define the limitation of the mold fabrication. Large areas with different diameters (50 nm-2 µm), pitch (100 nm-4 µm), and linear gradient should be provided with reproducible fabrication parameters. A special design was developed to address problems associated with down scaling of structures below 100 nm fabrication (Figure 4.1).

Table 4.1. Dimensions for mold fabrication for the three array designs.

Array design	Name	Diameter (µm)	Pitch (µm)
A) Arrays with a pitch double the diameter	A0.05	0.05	0.1
	A0.1	0.1	0.2
	A0.25	0.25	0.5
	A0.5	0.5	1
	A0.75	0.75	1.5
	A1	1	2
	A2	2	4
B) Arrays with constant pitch at increasing diameter	B0.1	0.1	1
	B0.25	0.25	1
	B0.5=A0.5	0.5	1
	B0.75	0.75	1
	B0.9	0.9	1
C) Linear gradient	G1	0.25	0.5–1.25
	G4	0.25	0.5–4.25
	G10	0.25	0.5–10.25
	G20	0.25	0.5–20.25
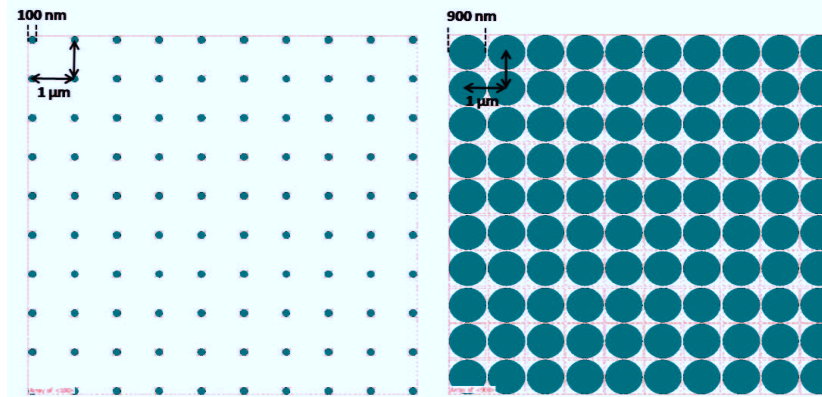
Figure 4.1. CleWin design for two arrays with 1 μm constant pitch.
In the left picture the structures have a 100 nm diameter and 1 μm pitch (B0.1). The right design is represented by the same pitch with a 100 nm space between the structures (900 nm structures diameter, B0.9).

4.2. Mold fabrication and characterization

Top-down fabrication approach was used to obtain molds with large scale arrays (1 x 1 cm) of nanoholes of different dimensions. The fabrication process flow forming Si/SiO$_2$ nanohole arrays is schematically illustrated in Figure 4.2.

4 inch Si wafers were used as main substrates for mold manufacturing. First, the Si wafer was oxidized to obtain a defined layer of SiO$_2$ (dry oxidation with 6 slm O$_2$, at 1100°C for 60 min) (Figure 4.2a). Then, PMMA (AR-P 669.04) resist was spin coated over the wafer homogeneously at 3000 rpm, for 45 sec and baked at 180°C, 5 min (Figure 4.2b). Using a design program (CleWin 4), the dimension of the structures in the PMMA resist was defined and transferred to the resist using EBL. The resist was exposed to an electron beam of 5 nm diameter, 2 nA beam current, 50 kV voltage, for fine pattern exposure. Furthermore, different doses were tested. The labels were processed using a 50 nm beam size, 150 nA beam current, and 250 μC/cm^2 dose (Figure 4.2c). After EBL, the exposed areas were dissolved by immersing the wafer in developer AR600-55 for 2 min. Then, the wafers were dipped in isopropanol for another 2 min in order to stop the development (Figure 4.2d). The rest of the PMMA layer acted as a mask during reactive ion etching (RIE). The recipe had CH$_3$/SF$_6$ (10/50 sccm) plasma chemistry (other parameters for etching will be described below and final recipes can be found in the Appendix C). The selected gases provide a sufficiently selective etching of SiO$_2$ over the resist (Figure 4.2e). After SiO$_2$ etching, the PMMA was etched too in the RIE chamber using O$_2$ plasma for 90 sec (Figure 4.2f).
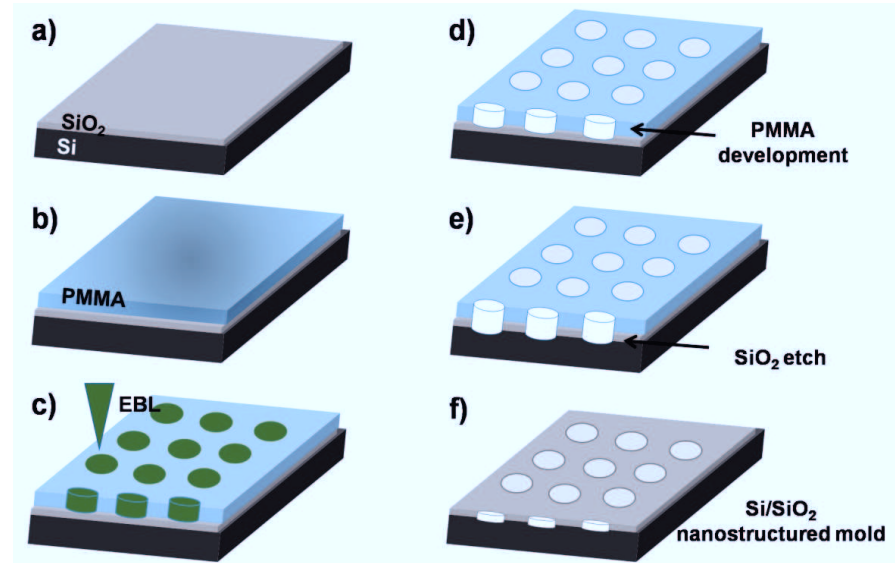
Figure 4.2. Schematic diagram of fabricating Si/SiO$_2$ nanohole arrays.

4.2.1. Optimization of fabrication parameters

In the first part of mold production all parameters were optimized for 100 nm structure depth. EBL was used as a lithography method due to the nanometer dimensions of the pattern. Due to high costs of EBL writing, the optimization of wafer fabrication was done for all structures on a small area (same wafer). For the first step in the lithography process the EBL dose was optimized. PMMA was used as an electron beam resist.[168] Before EBL, wafers were coated with a homogeneous 220 nm PMMA layer using spin coating. For all experiments, the acceleration voltage of the electron beam was fixed at 50 kV and a beam current of 2 nA was used. No proximity correction was needed because the pattern is homogeneous, covers a large area, and a small beam size was used (5 nm). Different doses were tested in order to obtain the dose suitable to write all dimensions, if possible. The doses varied between 190 μC/cm^2 and 325 μC/cm^2, with 15 μC/cm^2 increment (10 dose tests).
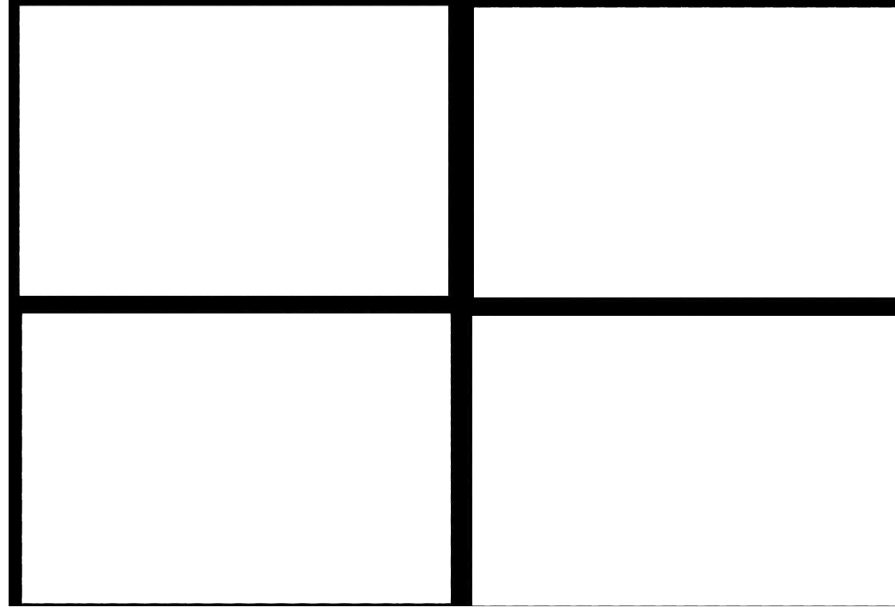
Figure 4.3. SEM images (0° tilt, 5 kV) of dose tests for B0.75 (a, b) and B0.9 (c, d) arrays. Image a) shows an underexposed pattern and non-symmetric structures obtained at a dose of 205 μC/cm². Image b) shows a perfectly developed pattern (dose 235 μC/cm²). Design B0.9 was fabricated with high quality at a dose of 220 μC/cm² (c). At higher doses (d) the circles are disconnected (overexposure).

Figure 4.2 shows SEM pictures that compare the dose effect of the structures with large diameter and small interdistance (B0.75 and B0.9). It can be observed that the pattern B0.75 (750 nm diameter, 1 μm pitch) was underexposed at a dose of 205 μC/cm² (Figure 4.3a). The structures did not have a symmetric shape in this case. If the dose was increased to 235 μC/cm², the structures showed smooth edges with diameters comparable to the ones designed with small standard deviation, 757 ± 3 nm (Figure 4.3b). On the other hand, if the distance between the structures was even smaller (B0.9, 900 nm diameter, 1 μm pitch) a dose of 220 μC/cm² was enough to obtain connected circles with 911 ± 40 nm diameter (Figure 4.3c). As the dose increased to 250 μC/cm², the resist was overexposed and homogeneous diamond-shape structures were obtained (Figure 4.3d). For bigger structures (or small structures, big interdistances), the dependence of PMMA on dose was not significant. Taking these results into account, a dose of 230 μC/cm² was chosen for the mold fabrication. With this dose, nanometer scale arrays were obtained, B0.1 (100 nm diameter, 200 nm pitch). Figure 4.4 shows the CleWin design and a representative SEM image. The structures diameter for this pattern was 124 ± 9.3 nm but the wafer reproducibility needed to be improved.
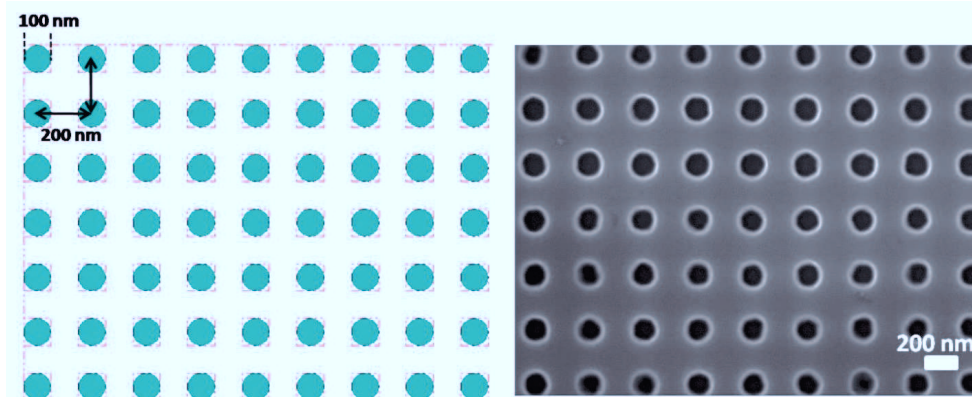
Figure 4.4. CleWin design (left) with SEM respective picture (right) of the A0.1 array (100 nm diameter, 200 nm pitch).

During development, the exposed resist from A0.05 and A0.1 was difficult to be removed completely since the developer solution has problems in penetrating the structures. Also, the etching was not reproducible during fabrication of A0.05 and A0.1 arrays. To overcome this problems a hard mask has been employed. The hard mask should improve the transfer of the resist patterns to SiO_2 layer with a small feature size during RIE.[169,170] First, the pattern was e-beam written in a positive resist and then transferred from resist to the metal mask by dry etching. A 20 nm Cr film was deposited onto SiO_2 (100 nm) layer by using an e-beam evaporation system (Pfeiffer PLS 570, 0.3 nm/sec). After Cr deposition, PMMA resist was spin coated (220 nm layer), followed by EBL and standard development (parameters described above). The wafer was etched for 8 min in the RIE chamber with O_2/Cl_2 (20/30 sccm) gas combination to specifically etch nanopatterns into Cr after PMMA development. Once the Cr hard mask was formed, the pattern was transferred to the SiO_2 layer using RIE (CHF_3/SF_6 50/10 sccm, RF 25, ICP 2006, Bias 30, , 24 sec, and 0°C temperature). After complete removal of PMMA and Cr mask, SEM and FIB-SEM characterization was performed (Figure 4.5). The fabricated structures exhibited a smaller diameter then designed (82.5 ± 3.8 nm). The pattern shape and the edges had some irregularities (Figure 4.5a, b). Importantly, straight sidewalls of the nanostructures were obtained using a Cr mask (Figure 4.5c, d). The fabrication technique including a Cr hard mask was suited for an anisotropy etching of nanostructures with a 0.8:1 aspect ratio (A0.1 array). A corresponding fabrication of A0.05 arrays did not show any improvement. Thinner PMMA layer (100 nm-double the structures diameter) should be used for future improvements of the array fabrication. Consequently, arrays as A0.05, A0.1, B0.1, and B0.9 were not used in further experiments due to low reproducibility.
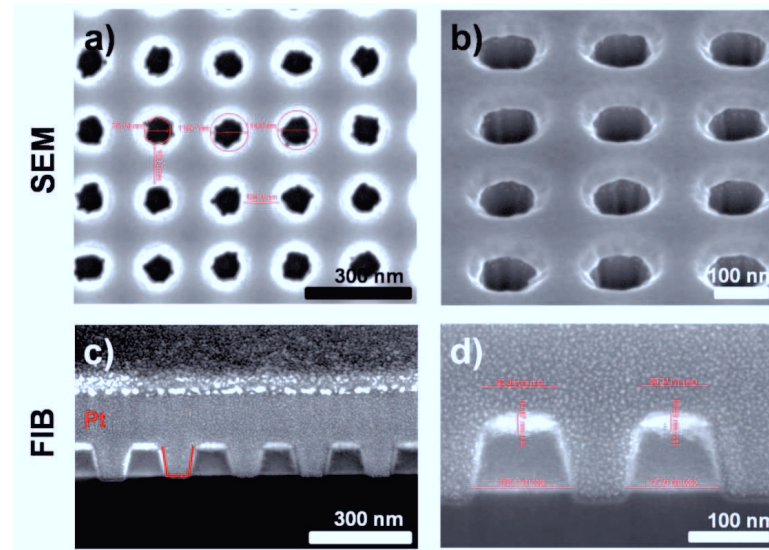
Figure 4.5. SEM and FIB cross section images of the A0.1 array using a Cr hard mask for mold fabrication. a) SEM image (0° tilt, 3kV) of nanostructures and a tilt view of them (b, 50° tilt, 3kV). c) FIB-SEM cross section through the nanoholes after Pt deposition (for protection); the shape of the nanohole was schematically shown with red lines together with a zoom-in (d).

4.2.2. Wafers with 100 nm structures depth

Out of the optimized structures, six of them in addition to the gradient were chosen for final wafer production. Table 4.2 presents the design dimension for the 100 nm depth of final arrays.

Table 4.2. The final structures after fabrication protocol optimization.

Final array design	Name	Diameter (µm)	Pitch (µm)
A) Arrays with pitch double the diameter	A0.5	0.5	1
	A0.75	0.75	1.5
	A1	1	2
	A2	2	4
B) Arrays with constant pitch	B0.25	0.25	1
	B0.75	0.75	1
C) Linear gradient	G1	0.25	0.5–1.25
	G4	0.25	0.5–4.25
	G10	0.25	0.5–10.25
	G20	0.25	0.5–20.25

Results obtained through the course of subchapter 4.2.1 showed that nanostructures with diameters ranging from 250 nm to 2 μm, and different distances could be produced using the same parameters. A single PMMA mask was used to produce nanostructures with a depth of 100 nm. All process parameters are shown once again in Appendix C. The A0.25 array (250 nm diameter, 500 nm pitch) was not produced due to the fact that these dimensions were already incorporated in the gradient. All arrays were fabricated with 1 x 1 cm size, with correspondent labeling and dash lines around the array. Using a Dektak profilometer (3030 Sloan/Veeco) on the labeling around the arrays we could characterize nanostructure depth after the fabrication process. Following parameters were used for measuring: 500 μm scan length, 15 sec scan duration with 0.1 resolution, stylus type radius 12.5 μm, and 3 mg stylus force. In terms of reproducibility of the nanostructure depth we observed a mean value 99.8 nm with a 4.4 nm deviation. Schematic and representative SEM pictures are depicted in Figure 4.6 for the isotropic 1 x 1 cm arrays A and B.
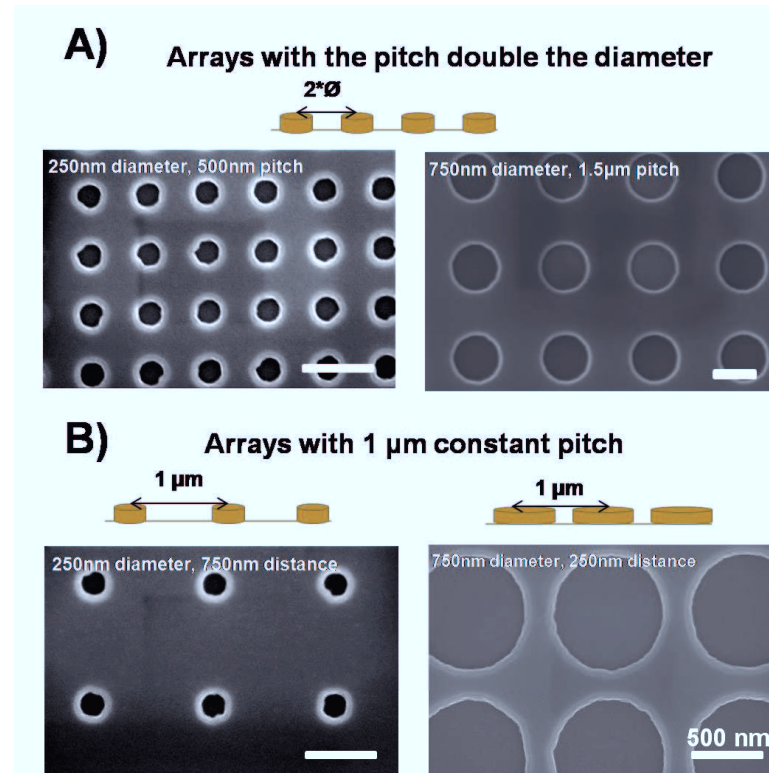
Figure 4.6. Representative schematic and SEM pictures for A) arrays with the pitch double the diameter (upper pictures) and B) arrays with a 1 μm constant pitch (bottom pictures). Structure dimensions are shown for each array, all SEM images were done at 0° tilt, 10 kV.

Together with the isotropic array, gradients with different slopes were produced, Figure 4.7. The 1 x 1 cm gradient area is divided into four different slopes of the structures. The diameter of structures (250 nm) and the pitch on the y axis (500nm) were constant. On the x axis, the slopes of nanostructure interdistance increased with different index in order to reach a distance at the final part of the array of 1 µm (slope $0.15 \cdot 10^{-3}$), 4 µm (slope $0.75 \cdot 10^{-3}$), 10 µm (slope $1.95 \cdot 10^{-3}$), and 20 µm ($3.95 \cdot 10^{-3}$). The slope was defined as the increased width of two neighboring structures (interpillar distance) divided by the area length (mm).
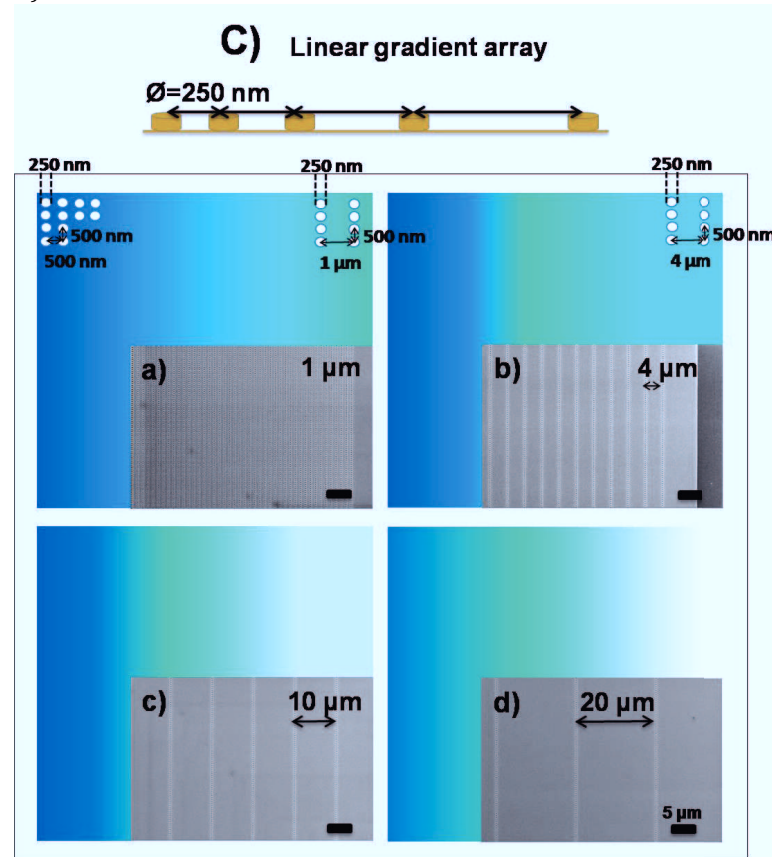
Figure 4.7. Graphical representation of the gradient and SEM micrographs of the four areas. The 1x1cm of gradient area is divided into four areas with different distance between the structures on the x-axis. The slopes increased until distance between the structures reached a) 1 µm, b) 4 µm, c) 10 µm, and d) 20 µm. For each array an inset of a SEM micrograph is presented showing the final distance on x axis (0° tilt, 10 kV). The schematic presented is not in scale.

4.2.3. Wafers with 400 nm structures depth

Another parameter influencing cell adhesion is the aspect ratio of the structures. Therefore, molds with the same structural elements as above but with a higher depth are fabricated for further investigations. The fabrication protocol for the wafers with an increase depth is shown in the Appendix C. Same design, materials, and process were used with only small changes. The 4 inch Si wafers were oxidized longer to obtain a thicker SiO_2-layer (525 nm). The PMMA resist layer thickness also needed to be increased. 424 nm PMMA was spin coated as a first layer, baked for 5 min at 180°C, and left to cool. Subsequently a second layer was spin coated and baked immediately afterwards. The parameters for EBL were kept the same. The development time and the RIE process were adapted according to the increased resist thickness and etching depth. Since the development time did not significantly influence the structure depth, the optimization focused on the etching process and time. The first step in this direction was to reduce the chamber temperature during etching to -100°C. It turned out that this could improve the stability of the PMMA layer for longer etching.[171] In Figure 4.8 the SEM images of the etching are shown after 1 min (a-c) and 3 min (d-e) for structures design a) and d) A1 (1 µm diameter, 2 µm pitch), b) and e) A0.5 (500 nm diameter, 1 µm pitch), and c) and f) A0.25 (250 nm diameter, 500 nm pitch). It can be observed that the SiO_2 layer is not etched more than 200 nm for 1 min etching time (a-c). Three minute etching resulted in a higher depth (300 nm) for all structure dimensions (d-f). On the other hand, a funnel shape was obtained in the long etching especially for small structures (f). According to these results, the etching time applied for the wafer production was 90 sec. Dektak measurements showed a 414 ± 6 nm depth of the structures. The detailed recipe is shown in Appendix C.
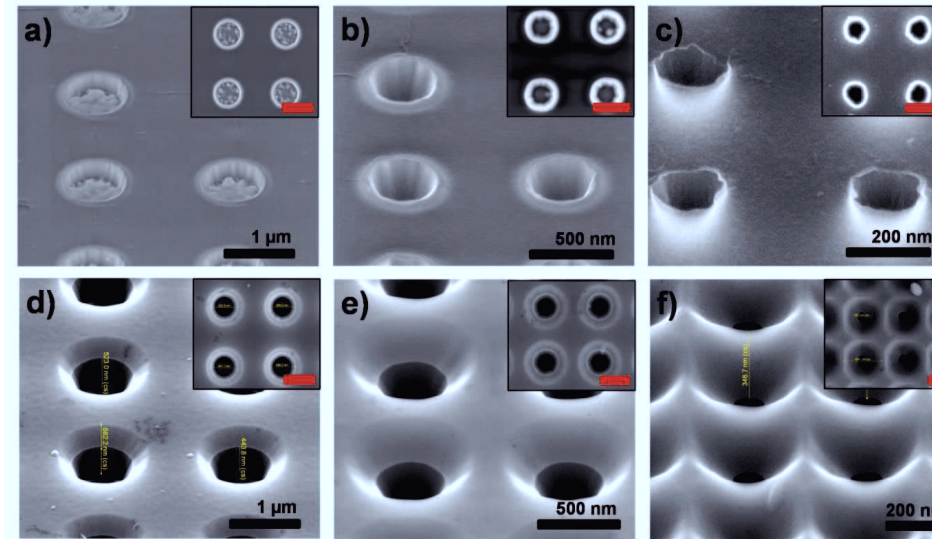
Figure 4.8. SEM images of etch time comparisons for structures design A1 (a, d), A0.5 (b, e, A0.25 (c, f). a) – c) etch time 1 min; d) – f) etch time 3 min. All insets from top-right of images shows a top view (0° tilt) of the respective etching test, and present the same scale bar.

Table 4.3. The calculated diameter of structures for all final arrays before replication.

Array	Designed diameter (nm)	Measured diameter (nm) 100 nm depth wafers	Measured diameter (nm) 400 nm depth wafers
A0.5	500	497 ± 3	506 ± 3.6
A0.75	750	761 ± 8.1	741 ± 60
A1	1000	1034 ± 10	985 ± 68
A2	2000	2036 ± 25	2038 ± 17
B0.25	250	224 ± 6.5	-
B0.75	750	801 ± 9.8	-
Gradient	250	264 ± 21	290 ± 23

4.3. OrmoComp single and double replication

OrmoComp hybrid polymer is proposed to be a reproducible, inexpensive material for NIL.[172–175] Using a quartz wafer as a substrate, we produced a transparent, mechanically strong, and durable replica. Furthermore, these replicas could be reused as molds for second replicas. Other polymers, like PDMS have disadvantages in the fabrication of nanopatterns with a high density and nanometer scale resolution because of the low Young's and tensile modulus.[176] Molds with both 100 nm and 400 nm depth were used for

replica production. The replication process is described in detail in Chapter 3. Figure 4.9 shows SEM images of mold A0.5 (Figure 4.9a, b) with a corresponding first replica (Figure 4.9c, d) and a second replica in the same hybrid polymer OrmoComp (Figure 4.9e, f). According to the properties of the polymer after polymerization (UV), the OrmoComp replica exhibits a shrinkage of around 6%.[173] The FIB cross section reveals that the pillar had a 352 nm diameter with around 60 nm height, Figure 4.9d. SEM and cross-section image of the second replica revealed a polymer depth of 58 nm after imprint. The nanohole has a top width of 570 nm and the bottom width of 420 nm. Here, the shrinkage is significantly larger (around 25%). The SEM of the replicas indicates a porous surface due to O_2 plasma probably caused by an oxidative decomposition of the polymer.[177] This could also be the reason of the shrinkage since the polymer surface was modified and a second replica applied (SEM characterization was performed after the double replication). The O_2 plasma modification was required to activate the surface for FOTCS silanization. For future experiments a liquid phase silanization should be considered to avoid the O_2 plasma activation.
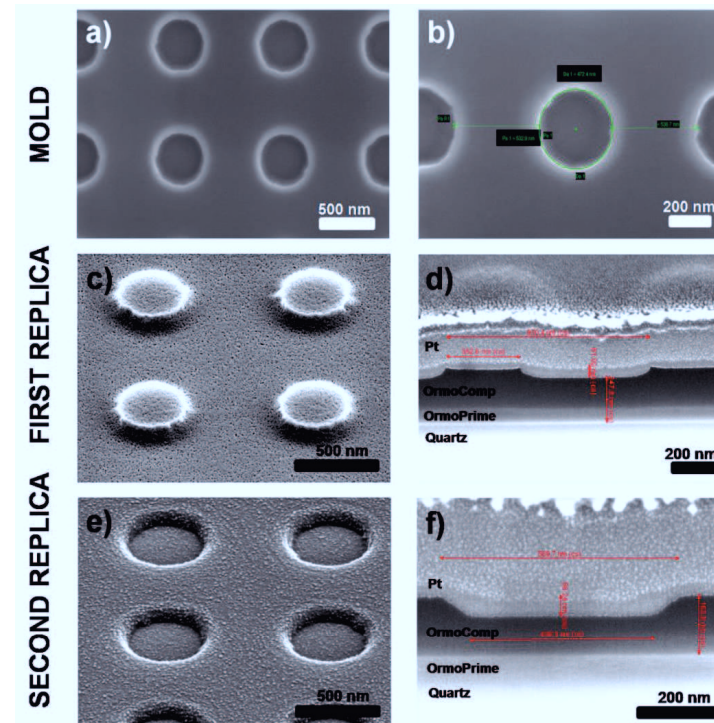
Figure 4.9. SEM and FIB sectioning after NIL double replication of the A0.5 array (500 nm diameter, 1 μm pitch). a) SEM image of the mold with a zoom-in showing measurements (b). c) First Ormocomp replica with correspondent FIB sectioning d). e) The second replica in OrmoComp and FIB cross sectioning (f).

Replicas with 400 nm structures height was also successfully produced on a large scale. The SEM pictures in Figure 4.10 show the three-dimensional microscale patterns of the master and the corresponding replica. The replicated structures exhibited excellent uniformity over a large area 1 x 1 cm. In this case, the mold height was 425 nm, while the cured replica was characterized by Dektak profilometer as 400 nm. This indicates a shrinkage of 7%, in concordance with polymer specification.[173] An analysis regarding the widths of the frustums at the top and bottom was performed to see how slated the walls of the pillars are. All structures present similar tilt angle, 145°. The fabricated pillars had dimensions that were reasonably close to these target values.
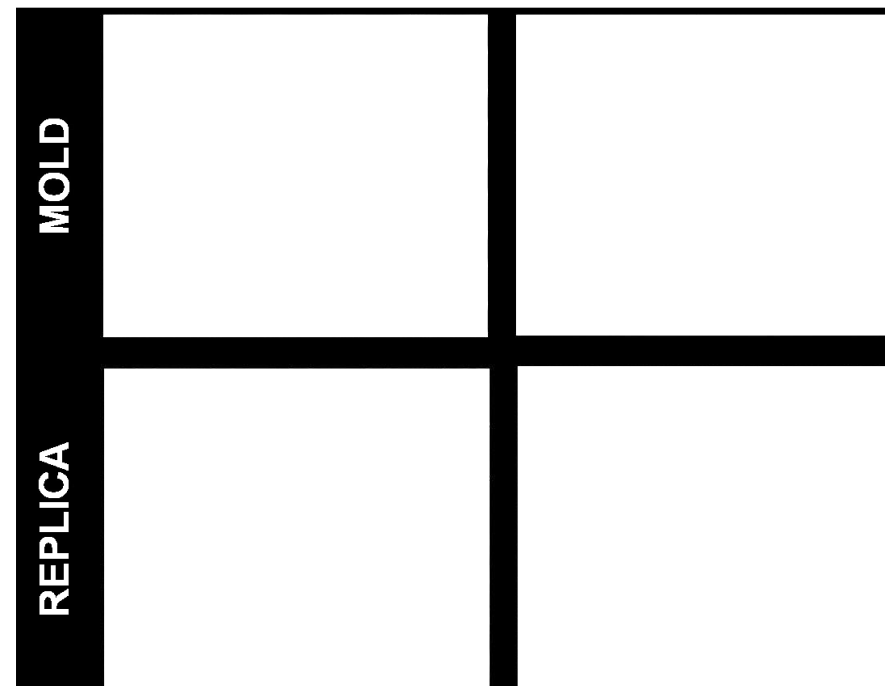
Figure 4.10. Mold and replica SEM characterization of the A0.75 array (750 nm diameter, 1.5 μm pitch). a, b) SEM images under 0° tilt angle showing the round shape of the structure and the smooth surface. OrmoComp replication on the large scale c) reveals a frustum shape of the structures with a 740 nm base and 335 nm top d).

5. CHARACTERIZATION OF CELL-SURFACE INTERFACE

In this chapter, a novel procedure of preparing biological samples on planar and 3D nanostructures is presented. First, the resin embedding approach is investigated by different excess layer of material. Then, the visualization of the actual interface was improved by cell staining. Finally, the development of advanced cell-substrate interface investigation techniques is described. The final method is based on a combination of fluorescence microscopy followed by FIB-SEM characterization of 3D sample structures in conjunction with cells.

5.1. Cell–3D interface investigation by fluorescence and electron microscopy

Neuroengineering of efficient neural interfaces is crucial for the development of long-lasting neural prosthesis and brain computer interfaces.[9,24] For example, structured microelectrodes arrays (MEAs) with spines, rods, or mushrooms shape were employed to improve cell adhesion to microelectrodes and create neuronal networks, which can be used for electrophysiological devices.[140] These 3D micro- and nanostructures are also capable of influencing the directional outgrowth of cells as well as minimize the cleft at the cell–electrode interface and thus, increase the seal resistance of the system at the nanoscale.[178] Cell response to engineered substrates can be investigated by standard techniques such as fluorescence microscopy[25], surface plasmon microscopy[26], or electron microscopy.[27–29] Investigation of cell–electrode interface at the nanoscale remains a big challenge for understanding how the cell attaches and responds to the device surface. Cell biology offers hints towards mechanisms that may mediate useful interactions between these substrate-mediated effects on cell phenotype. Perhaps the simplest method by which the substrate nanotopography influences cell responses would be the increase in available surface area arising from the feature sidewalls. Cells cultured on a certain topography have to expose an increased proportion of their membrane creating a larger area for adhesion complexes to attach and internalize the 3D structures. By linking actin dynamics to extracellular components, integrins are involved in a wide range of cellular processes that are associated with or require cytoskeletal remodeling and cell-shape changes. One such integrin-dependent process is phagocytosis, a process that involves specific cell-surface receptors and signaling cascades with the formation of cell membrane protrusions that eventually envelop the external micrometer cargo (>1 μm).[179] Since the 3D MEAs are not detachable from the surface (pseudo-3D), the cell responds by an engulfment-like event to these 3D

51

electrode topographies, similar to phagocytosis. Cells' actin filaments wrap around the 3D structure to mechanically stabilize the junctional membrane providing a tight contact.[180] Current approaches in 3D-cell interface imaging include fluorescence microscopy and electron microscopy. Fluorescence microscopy has been largely involved in visualizing the cell response and evaluating the biocompatibility of 3D structured substrates. However, fluorophores are difficult to visualize in close proximity of a metal surface. Furthermore, fluorescence microscopy does not achieve high resolution in all three space dimensions at the nanoscale. For this reason, transmission electron microscopy (TEM) was used to visualize detailed ultrastructural information in biological specimens with sub-micron resolution.[27,28,30,180,181] However, the samples require long time preparation. Thin samples are typically cut by an ultramicrotome and for composite samples containing glass or silicon substrates there is a risk of delamination and distortions during ultramicrotomy. Alternatively, substrates can be sectioned by focused ion beam (FIB) and the interface studied by a scanning electron microscope (SEM).[30–32] The FIB-SEM represents the most promising technique at the moment due to: i) faster sectioning in sample preparation (compared with microtome/TEM); ii) the possibility of sequential sectioning; iii) the high spatial resolution control (down to 50-100 nm).[31,182–185]

As presented above, the sample preparation is very important. In the following subsections, different preparation methodologies are described in detailed. Critical point drying (CPD) is commonly used for samples investigated with a scanning electron beam, whereas resin-infiltration is typically used for TEM. Later, the novel ultra-thin resin method is presented and highlighted in contrast to these standard methods.

5.2. Resin embedding method

Usually, biological samples require an extensive preparation protocol to stabilize the sample for electron microscopy and to preserve the delicate ultrastructure. In most cases this involves embedding into a block of resin, which is later trimmed in such a way that the structures of interest become located close to the surface of the block. Often it can happen that no region of interest can be identified within the large resin block. In some cases, the resin is first polymerized and then mechanically removed (*i.e.* using microtomes). The novelty in this method is the removal of excess resin before polymerization.[33] Suitable ultra-thin resin thickness was the first step in optimizing the embedding protocol. Planar Si/SiO_2 substrates were used for neuron culture. After 3 DIV, cells were chemically fixed. Among all the fixative solutions, glutaraldehyde is the most effective in preserving the fine structures because it is cross-linking proteins effectively and irreversibly. Glutaraldehyde stabilizes intracellular systems such as microtubules, microfilaments, rough and smooth endoplasmic reticulum, vesicles, *etc*. Conformational and biological activity of proteins does not cause significant protein conformational changes after their moderate cross-linking by glutaraldehyde. A possible reason for this phenomenon is related to the fact that amino

groups, which are the primary target of glutaraldehyde, are usually abundant on the surface of proteins. The rate of penetration depends on the solution concentration, the ambient temperature, and the type of buffer used. Using cacodylate as a buffer, additional phosphates are avoided during sample preparations. Organelles, such as mitochondria can be damaged when exposed to high concentrations of phosphate buffers.[186]

After fixation, the cells were dehydrated in ethanol since the resin composition is not miscible with water. Further, the ethanol was gradually exchanged with resin. The two-component epoxy-base and the catalyst were mixed avoiding the formation of air bubbles until color of the solution changed from red/orange to yellow. After substrate embedding, the resin was removed using ethanol splashing. Ethanol rinsing of the sample is the critical parameter of sample preparation for this method. Using quick sequential splashing with ethanol the excess resin layer was removed. A nominal ethanol volume of 5 ml was used for each splashing repetition. Four different volumes of ethanol were used to quantify the effective resin's thickness: 5 ml, 25 ml, 50 ml, and 150 ml on an overall substrate area of 1.2 cm^2. Figure 5.1 shows resin layer thickness as function of the ethanol volume used for rinsing. Low amount of ethanol (5 ml, Figure 5.1a) was not enough to remove sufficient amount of the resin to clearly identify the neuronal cell body perimeter and neurites even at high acceleration voltages. The residual resin layer possessed a thickness of about 1 μm. A decrease of residual resin thickness to 500 nm was obtained using a nominal ethanol volume of 25 ml (Figure 5.1b). Under these conditions, it was possible to clearly identify single cells on the substrate and, thus, several regions of interest for imaging. An optimal resin thickness for topographical characterization of neurons was achieved for an ethanol volume of 50 ml. An ultra-thin layer of about 5 nm allows a clear visualization of small neurites, filopodia or neurites branching without artefacts (Figure 5.1c). In contrast to that, the neuronal cell membrane and neurites exhibited damages for 150 ml volume of ethanol. A high amount of ethanol could remove a part of the resin embedded at the cell surface. During polymerization (at 60°C), this induced structural damages due to fast ethanol evaporation. In several cases, partial or total detachment of cells from the culture was observed (Figure 5.1d). In addition to SEM topographical investigation, FIB transversal sectioning was performed for evaluating the resin infiltration. All resin thicknesses considered did not alter the attachment conditions of cell-substrates interaction (Fig. 5.1, right insets).
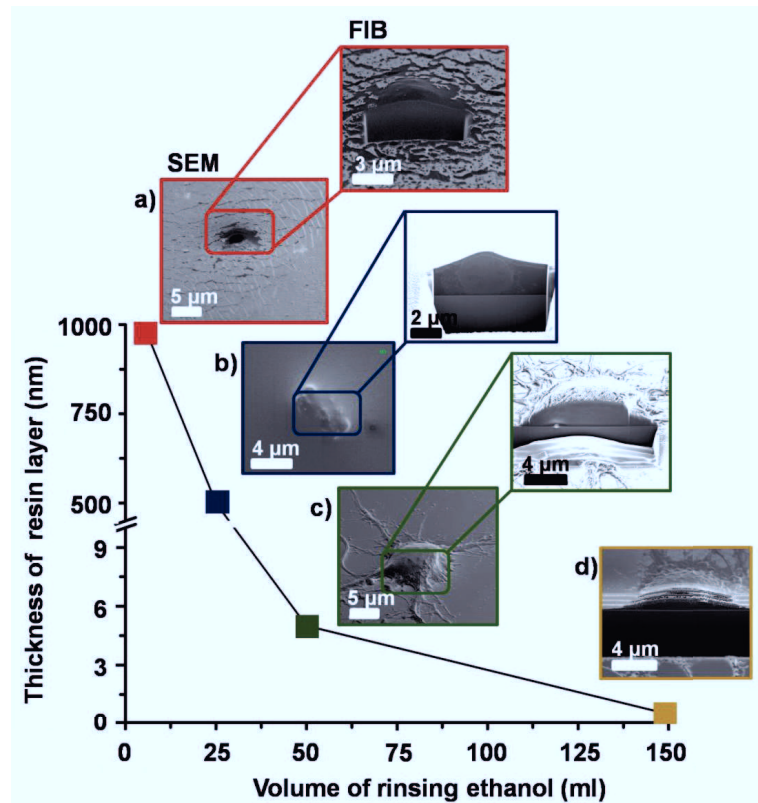
Figure 5.1. Resin layer thickness in dependence on the amount of ethanol used to remove the resin excess from the specimens. SEM and corresponding FIB-SEM results of resin embedded cortical neurons with gradually less resin covering the cells: a) 5 ml (about 1 μm thickness); b) 25 ml (500 nm layer reveals first cellular outlines); c) 50 ml (nearly all cellular features can be observed with obtained 5 nm-thick resin layer); d) 150 ml (damaged neuron and flat, but still compact cell-substrate interface).[33]

5.3. Optimization protocol for neuron-surface interface characterization

Despite the potential advantages of the ultra-thin resin preparation for FIB-SEM in biological interfacing, it is still not possible to visualize the cell-surface interface with high resolution. FIB-SEM imaging of the actual contact of the interaction and adhesion, together with cells' body components represents a great interest of cell-3D nanostructures investigations.[33] For this reason, further optimization of biological specimens had to be improved by cell staining. The protocol for sample preparation using fixation, staining, and ultra-thin resin embedding is presented in Figure 5.2.
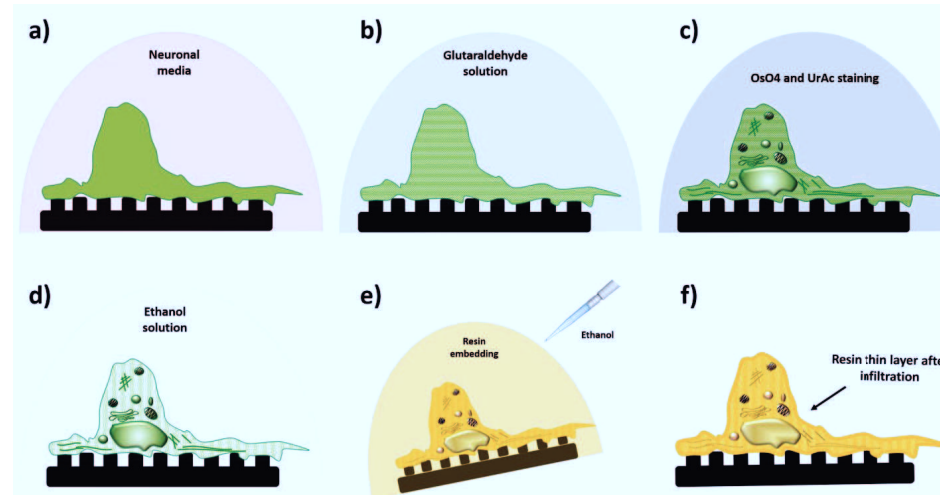
Figure 5.2. Preparation of biological samples for electron and ion microscopy using optimized resin embedding procedure. Schematic representation of: a) Primary neurons in media; b) Fixation of cells with a glutaraldehyde solution; c) Secondary fixation and staining of cells with osmium tetroxide (OsO_4) and uranyl acetate (UrAc); d) Replacement of the medium with increasing series of ethanol solution; e) Resin embedding and excess resin removal after embedding procedure with ethanol; f) Polymerization of resin-embedded samples using thermal treatment.

First, sample fixation was achieved with a 3.2% glutaraldehyde solution in the cacodylate buffer (37°C) for 30 min at room temperature (Figure 5.2b). Then, samples were rinsed twice in cacodylate buffer and osmium tetroxide (OsO_4) post-fixation was performed. A 2% OsO_4 aqueous solution was diluted to a concentration of 1% (vol/vol) in cacodylate buffer. The samples were immersed in the solution for 2 h, on ice. OsO_4 penetrates into tissues, cells, and organelles and acts not only as a fixative but also as an electron stain. The bifunctional effect of OsO_4 preserves many lipids and is able to stabilize some proteins into clear gels, without destroying many of the structural features. In this way, the membrane fluidity is reduced to zero. Also, OsO_4 increases the electron density to cell components.[186] Then, samples were rinsed five times with Milli-Q water for 2 min each time at room temperature. The samples were transferred to a 1% (wt/vol) tannic acid in Milli-Q solution for 30 min at room temperature. The solution was always prepared shortly before usage. Tannic acid main purpose is due to its mordant property. A mordant facilitates the binding of heavy metal stains to biological structures, enhancing their contrast in electron microscopy investigations. Being hydrolysable, its molecule is capable of multiple ligand-mediated interactions. It interacts with osmium bonds in membranes and facilitates binding of uranyl ions. Membrane treated with tannic acid bind more uranyl

acetate (UrAc) than untreated cells. Another advantage of using tannic acid is the fact that certain types of cellular proteins and ECM proteins become less prone to damage by the electron beam during imaging.[186,187] The final step in cell staining is the introduction of UrAc. A 2% solution of UrAc in water (depleted uranium) was used to treat cells for 5 h at 4°C (Figure 5.2c). Treatment with aqueous uranyl acetate following double fixation with glutaraldehyde and OsO_4 strongly improves the staining of the cell membrane and other cell structures. Uranium, with atomic number 92, is the heaviest metal used as an electron stain. Even few uranyl ions or complex ions bound on macromolecules are enough to visualize them by electron microscopy. The staining and fixative properties of UrAc are based on its capability to react with various species and both negatively and positively charged side chains on proteins.[186] After fixation and staining, cells were washed with Milli-Q water. Later, the cells were dehydrated via the same ethanol rinsing series as for the CPD procedure: 10%-100% ethanol solutions in Milli-Q water (Figure 5.2d). A resin solution was freshly prepared each time. Its preparation is described in Appendix B (mixture of solution Epon 812, DDSA, MNA, and DMP-30 catalyst). The samples were then gradually incubated in mixtures of ethanol and resin. At the end of the resin exchange, the samples were covered with pure resin (Figure 5.2e). The critical step of the resin embedding method represents the removal of excess resin surrounding the sample and was discussed in the subchapter above. Finally, resin polymerization was achieved by baking the samples for 24 h at 60°C (Figure 5.2f).

5.3.1. Comparison of critical point drying *vs.* resin embedding method

A direct comparison of CPD and thin-layer resin embedding preparation effects using single neuron culture and network formation is described in this subchapter. Instead of resin embedding, cells can be treated with CPD or air drying process. After CPD, cells can be sectioned by FIB and the interface be studied using SEM.[29,182,188] However, a typical shrinkage of up to 20% can be visible in air or CPD prepared cells.[189] The physiological cell volume results decreases due to liquid-gas transition and surface tension during the CPD process.[183,189] Cells prepared with this technique usually present a sponge-like intracellular morphology.[182] On the other hand, resin embedding method favors cell volume preservation while avoiding structural and morphological artifacts due to the fact that the water components in the cell are basically replaced with infiltrated resin. After optimization of the resin excess layer, an artifact-free preparation for SEM topographical characterization was obtained (Figure 5.3b). Red arrows point out the connections between two cells. Cells prepared via CPD clearly have destroyed connective points between adjacent cells (Figure 5.3a). During transition of liquid CO_2 to gaseous phase, the damage occurred due to the tension formed. In contrast, resin embedded neuronal cells showed continuous and intact connection points without any visible damage as highlighted by the red arrows in Figure 5.3b.
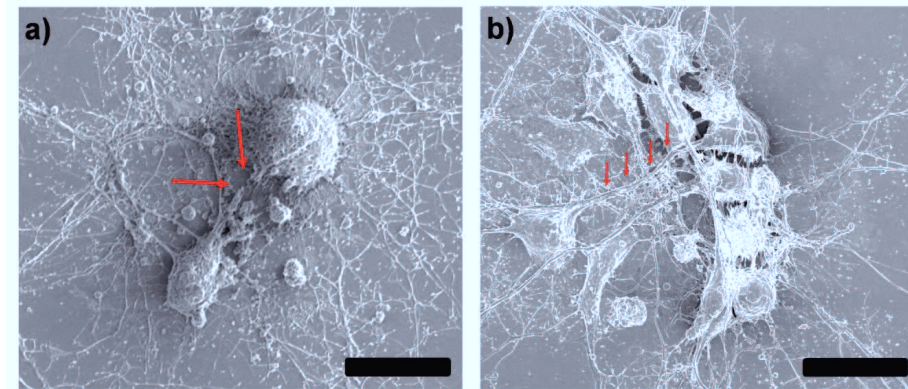
Figure 5.3. SEM images of neuron-neuron interaction prepared with a) CPD and b) ultra-thin resin embedding method. Scale bars: 10 μm.

Another point of interest was the integrity of cell volume and small protrusions during preparation (Figure 5.4). In particular, small cellular structures need to be preserved to understanding cell-cell (*i.e.* dendritic spines) and cell-substrate interaction (*i.e.* growth cones). For this reason, a particular attention was given to neuronal growth cones (Figure 5.3a-d). Growth cones of CPD prepared cells showed extremely porous membrane residues and several cracked protrusions (red arrow, Figure 5.4a, b). Resin embedded neuronal cells revealed complete protrusions and a less porous growth cone membrane adhering on the substrate. Furthermore, it was also possible to observe (Figure 5.4c, d) that the membrane was better preserved in terms of volume and membrane protrusions (red arrows). Moreover, resin embedding showed a significant improvement in transversal sectioning of neurons compared with standard CPD preparation (Figure 5.4e, f). CPD cells had a sponge-like morphology so the observation of the interaction with the planar substrate or 3D nanostructures is limited (Figure 5.4e).[33] On the other hand, resin embedding procedure, after the staining optimization step, was used to observe cell contact with the artificial solid surfaces, Figure 5.4f. The actual contact between neurons and nanostructures can be observed, as well as the cell nucleus and other small components.
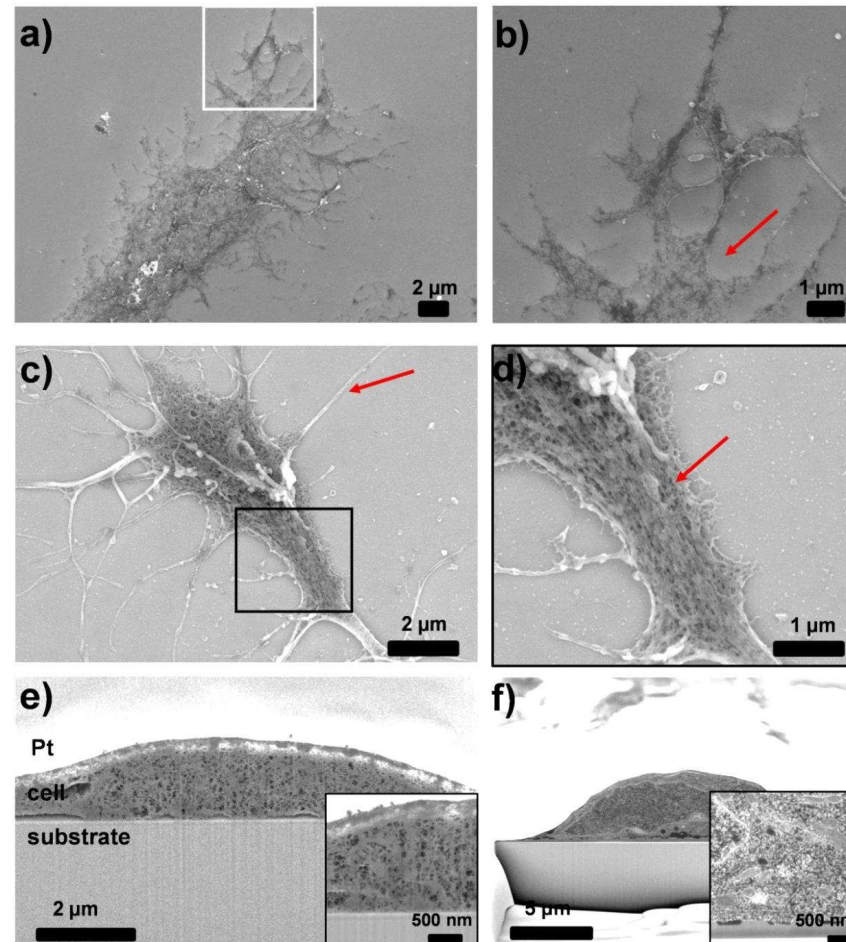
Figure 5.3. Comparison of CPD and resin embedding preparations on artificial substrates. a) Neuron growth cones have a porous structure when prepared with CPD. c) SEM image shows the neurite integrity after resin preparation. b) and d) are enlarged areas in a) and c) marked with a rectangle. e, f) Cross sections of neuron cell bodies after CPD and resin preparation. CPD preparation produced a sponge-like morphology of the cell soma (e), while resin preparation lead to interface and small cell characterization without artefacts (f). Insets in (e, f) are high magnification images of the soma-artificial surface interface.

SEM investigation of single cells with almost no resin over-embedding preserves the original volume of the cell and, in particular, small cell features do not break or get 'porous' as in traditional SEM preparation techniques (CPD method).[29] The innovative resin embedding procedure enables performing electron and ion microscopy investigations for the same specimen.

5.3.2. Fluorescence and electron microscopy investigation of cell-surface interface
A final question arose after the resin preparation method was optimized regarding fixation and staining: Would it be possible to prevent artifacts even after cell characterization with fluorescence microscopy? Although conventional fluorescence microscopy does not allow to achieve nanoscale resolution it is widely used to understand cell-nanostructured interactions. For this purpose, fluorescence microscopy was used to visualize specific neuronal morphologies based on staining individual cell components such as nuclei (DAPI-blue color), neurites (β3 tubulin-green color), and F-actin distribution (phalloidin-red color), Figure 5.5b. For immunostaining, the cells cultured for 3 DIV (Figure 5.5a) were fixed with 4% (w/v) PFA in PBS for 12 min at room temperature. Then, permeabilization and blocking for unspecific binding to cell membrane was done with 0.3% TritonX-100 and blocking buffer, respectively. Samples were then incubated with DAPI, β3 tubulin, and phalloidin solution. The fluorescence protocol and imaging was described in Chapter 3. After imaging, the cells were chemically fixed for the second time with 3.2% glutaraldehyde at room temperature for 30 min. Then, the samples were stained with OsO_4, tannic acid, UrAc, and embedded gradually in resin media. The excess resin layer was removed with optimal ethanol volume (protocol above). Optical micrographs (Figure 5.5c, d) showed that cells preserve their volume and morphological characteristics. Moreover, a selected cell from the same sample was sectioned with FIB (Figure 5.5e, f). No artifacts were observed and intracellular structures were imaged at a nanoscale resolution. The immunostaining was used to evaluate typical morphological aspects in this stage of development. Moreover, phalloidin staining can be used to investigate cell adhesion by fluorescence intensity. A correlation between cell surface contacts and the distribution of cytoskeletal proteins can be made. In conclusion, the resin embedding procedure in combination and with fluorescence imaging and high-resolution electron microscopy leads to a comprehensive characterization of cell topography.
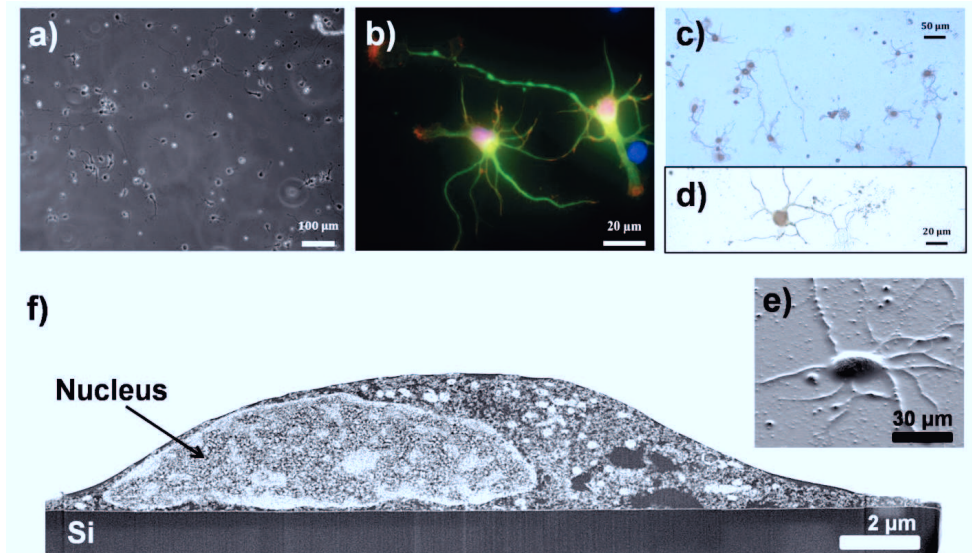
Figure 5.5. Versatility of the ultra-thin resin embedding method. A comprehensive investigation of the same specimen was achieved using optical and electron microscopy for cell-surface investigation. a) *In-vitro* neuron culture after 4 DIV before fixation. b) Immunofluorescence staining of nuclei (blue), neurites (green), and actin (red). Optical micrographs after resin embedding method of cell network (c) and single cell (d). e) SEM characterization, followed by a cross-sectioning of the same neuron (f). FIB-SEM of the neuronal cells shows a complete cell staining and cell contact with the planar Si substrate.

The advantage of the resin embedding consists in the fact that this method is versatile. First, resin embedding procedure was optimized in order to enable SEM investigations of single cells or cell - cell interactions with almost no resin over-embedding. Furthermore, a complete staining of the cell membrane and intracellular structures was performed. The cell membrane conformation around the nanostructures was imaged with a high resolution and contrast. This can be used to perform sequential cross sectioning of resin-embedded individual cells aiming to obtain a 3D reconstruction of the cell-surface interface. Moreover, the combination of fluorescence microscopy followed by electron microscopy studies of the same sample after imaging, fixation, dehydration, staining, and resin embedding was demonstrated for the first time.

6. NEURONAL RESPONSES ON 3D POLYMER NANOSTRUCTURES

In this chapter, three-dimensional (3D) vertically or tilted aligned nano- and micropillars large arrays were used for a comprehensive *in vitro* study of the development of primary cortical neurons. Neurons were cultured on two types of topographies: isotropic and anisotropic, and two types of biomaterials: OrmoComp and parylene C (PPX). First, the OrmoComp isotropic surfaces were taken under consideration. Nano- and micropillar arrays consisting of vertical pillars with 100 nm and 400 nm heights were used for investigating structured surface-cell interactions. The arrays had either a pitch twice as large as the diameter (diameter identical with the interpillar distance) or a constant pitch (center to center distance) with a varying diameter. Next, anisotropic surfaces were used to investigate the development of neurons. A well-controlled linear gradient of nanostructures (constant height, constant structures diameter, increasing interpillar distances on *y* axis) on both OrmoComp and parylene C surfaces were employed for cell culture. Then, tilted nanotextured parylene was used for a comprehensive exploration of single cell behaviors at large array interfaces. Fluorescence microscopy and high-resolution SEM, FIB-SEM techniques were used for quantification of neuronal viability, adhesions, development, and cell-surface interface. Guiding effects of neuron outgrowth were also observed and characterized.

6.1. Interactions of neurons with isotropic structures

Nanopatterned substrates were fabricated from OrmoComp hybrid polymer using the previously described protocol, outlined in Chapter 4. For arrays A (arrays with the pitch double the diameter) two heights of the structures were used for cell culture experiments: 100 nm and 400 nm. B arrays (1 µm contact pitch) had a constant height of 100 nm (Table 6.1).

Table 6.1. Dimension of the isotropic nanostructures design.

Array design	Name	Diameter (µm)	Pitch (µm)
A) Arrays with pitch double the diameter **(Heights: H100 nm and H400 nm)**	A0.5	0.5	1
	A0.75	0.75	1.5
	A1	1	2
	A2	2	4
B) Arrays with constant pitch (H100 nm)	B0.25	0.25	1
	B0.5=A0.5	0.5	1
	B0.75	0.75	1

6.1.1. Neuronal viability

To assess the neural response to different surface topographies, primary cortical neurons were seeded on control coverslips, flat, and patterned OrmoComp surfaces. Before protein coating, the samples were investigated regarding surface wettability. Static contact angles for each surface were measured. The contact angles for the flat surface were 70 ± 3°, while the pattern OrmoComp surfaces had a higher contact angle (80 ± 5°, mean of all different topographies). The surface composition and chemistry remained the same between the flat and nanotextured OrmoComp, therefore the increase in hydrophobicity of the nanostructured OrmoComp is attributed to its higher surface roughness. After PLL coating, the contact angles decrease to <10° for all surface types.

Biocompatibility of OrmoComp surfaces was evaluated and compared with glass coverslip controls. Neurons were imaged every day from seeding until 9 DIV in order to observe long time culture. Figure 6.1 shows representative images of cells during development from 1, 3, 6, and 9 DIV. As presented in Chapter 2, the neuronal maturation was characterized according to the five stages of development introduced by Arimura et al.[69] At first, dissociated neurons settle to the surface of the substrate where they form thin filopodia, hair-like sprouts, on the outside of their membranes (Stage 1) and start their development. In the second step (1-2 DIV) immature neurites are formed with the same length, morphologically equal (Stage 2). For both, control and OrmoComp patterned surface, cells were in Stage 2 development after 1 DIV (Figure 6.1, 1 DIV). Stage 3 of development is representative for 2-4 DIV and characterized by a break of the cell symmetry. One of the neurites starts to elongate faster than the others, a fact observable also in Figure 6.1, 3 DIV. The longest neurite acquires the molecular specificities of the axon while other neurites differentiate into dendrites. Neurons between 4-7 DIV are defined as Stage 4 of development. For neuronal density used in this thesis (2 x 10^4 cells/ml), it was observed that after 6 DIV the cultured cells form networks (Figure 6.1). In the last stage, Stage 5, dendritic spines are formed. Fully mature and functional dendrites facilitate the connection between neighboring cells and thereby enable the communication among single neurons in a network (Figure 6.1, 9 DIV). Axon development in all stages is indicated with red arrows (Figure 6.1).
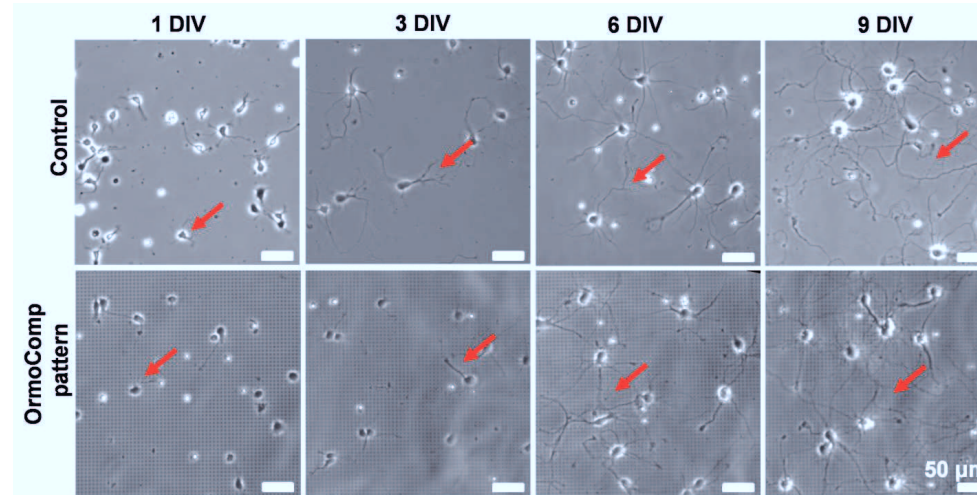
Figure 6.1. DIC micrographs of neuronal cells in culture from day 1 until day 9 in culture. Nanopatterned OrmoComp substrates presented in the images correspond to A2 array (2 μm structures diameter, 4 μm pitch, and 100 nm height). Red arrows mark the axon development during culture: immature neurites, morphologically equal (1 DIV, Stage 2); breaking of neurite symmetry into axon and dentrites (3 DIV, Stage 3); neurite branching and elongation (6 DIV, Stage 4); synaptic contacts are formed via dendritic spines and axon terminals assemble a mature neuronal network (9 DIV, Stage 5).

To achieve the purpose of this thesis the neuron were investigated in the Stage 3 of development (3-4 DIV). Investigation of neurons at 3 DIV present the following benefits: i) single cell investigation is possible for higher densities cell cultures before cell-cell signaling becomes influential; ii) investigation of neuronal polarity. Purpose of using high cell densities was to adapt the *in vitro* cell culture as much as possible to cell studies and tissue in contact with implants. Higher cell densities commonly allow long-term culture, network formation and synaptogenesis. As Figure 6.1 shows, cells will form networks for longer cultures than 3 DIV. This leads to a decrease in topographical influence, which is compensated by chemical cues (neuronal signaling).[22,34–36] Stage 3 of development was shown to be the most critical in neuronal polarity formation. Breaking the symmetry and axon differentiation is important to investigate since nanotopography-cell interaction studies showed that this can lead to morphological changes. In comparison to planar samples the neuron-material nano-interface was shown to support neurite elongation and branching.[37,38]

Cell viability was evaluated for all substrates at 3 DIV and control coverslip samples. Three independent cell cultures were performed for the viability study. No significant differences compared with control substrates were observed (Figure 6.2).
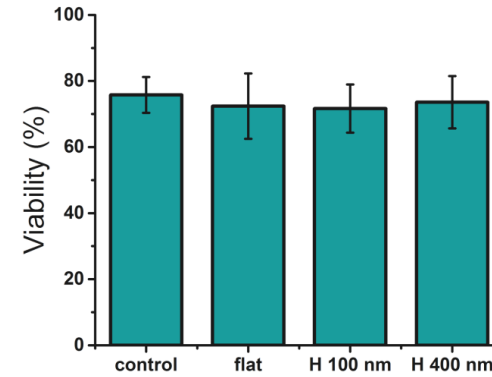
Figure 6.2. Neuronal viability in a series of independent experiments after 3 DIV.

The observed viability validates the biocompatibility of OrmoComp substrate[10,11,15,190,191] for neuronal culture. Moreover, OrmoComp substrate topography with 100 and 400 nm height pillars did not show any significant effects on neuronal survival rate.

6.1.2. Influence of isotropic nanopillars on neuronal development

Substrate micro- and nano-topography, independent of substrate biochemistry, appears to have an effect on cell behavior such as attachment, cell orientation, morphology, and cytoskeleton arrangements.[120,192–194] In comparison to planar sample, the neuron-material nano-interface was shown to support neurite elongation and branching.[37,38] In this regard, morphological features including soma area, axonal length, neurite number, axonal branching and axonal turns of neurons were investigated. Neurons growing on nanostructured substrates were compared to those on flat polymer surfaces. Control substrates were not plotted since the values obtained were similar to planar polymer substrates. All isotropic surfaces were produced using OrmoComp polymer as a material for replicas.
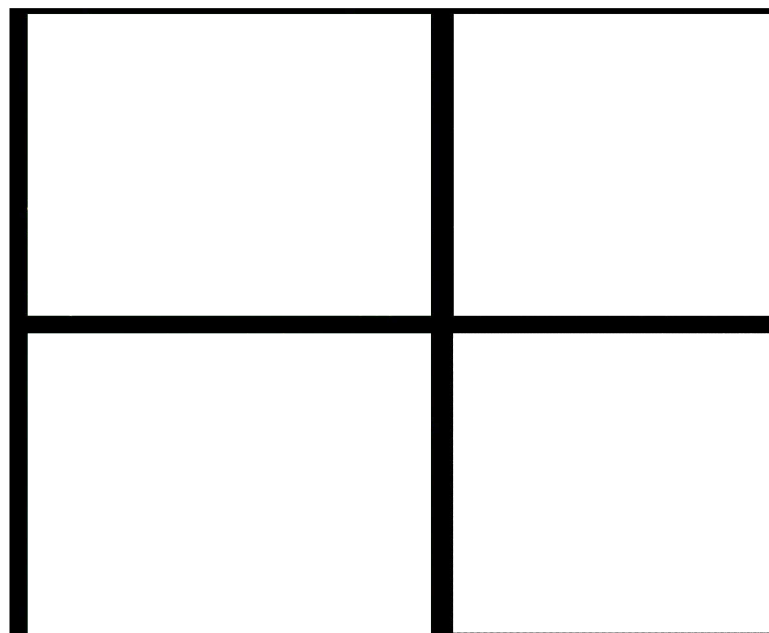
Figure 6.3. Fluorescence and SEM micrographs of neuron cultures on planar (a, b) and nanotextured OrmoComp surface, 100 nm height (c, d). Fluorescence images show nuclei in blue, cytoskeleton staining in orange and axon specific staining in green. Axon directionality can be observed for nanotextured surface, indicated by the red arrow (c). (b, d) SEM characterization of cell-structure interaction shows the cell adhesion on flat (b) and nanostructure surface (d). Before imaging cell were prepared by CPD and imaged under 0° tilt with 3 kV.

A representative fluorescence image of neurons cultured on flat and nanotextured OrmoComp is shown in Figure 6.3a, c. Subsequently, the same samples were investigated by higher resolution SEM (Figure 6.3b, d). Size and shape of the cell body and neurite outgrowth are comparable to those on planar substrates. However, for a comprehensive analysis of cell morphological changes all surfaces were investigated using fluorescence microscopy, followed by subsequent image processing. Axon development was investigated by staining of neurofilament subunits, which are incorporated all along the axon in the outgrowth process (NFH, green color). Microtubules staining was used to observe the cytoskeleton and quantify the soma area and neurite number (β3 tubulin, orange color). Cell nuclei were imaged using DAPI staining (blue color). Neurons staining divided by different fluorescent channels is shown in Figure 6.4 along with the composite image and a z-stack representation of the same neuron. The z-stack was composed of 21 images in z direction which are merged into a single image with a height of 4.6 μm. The z-stack characterization can be used to analyze the cells' vertical profile.
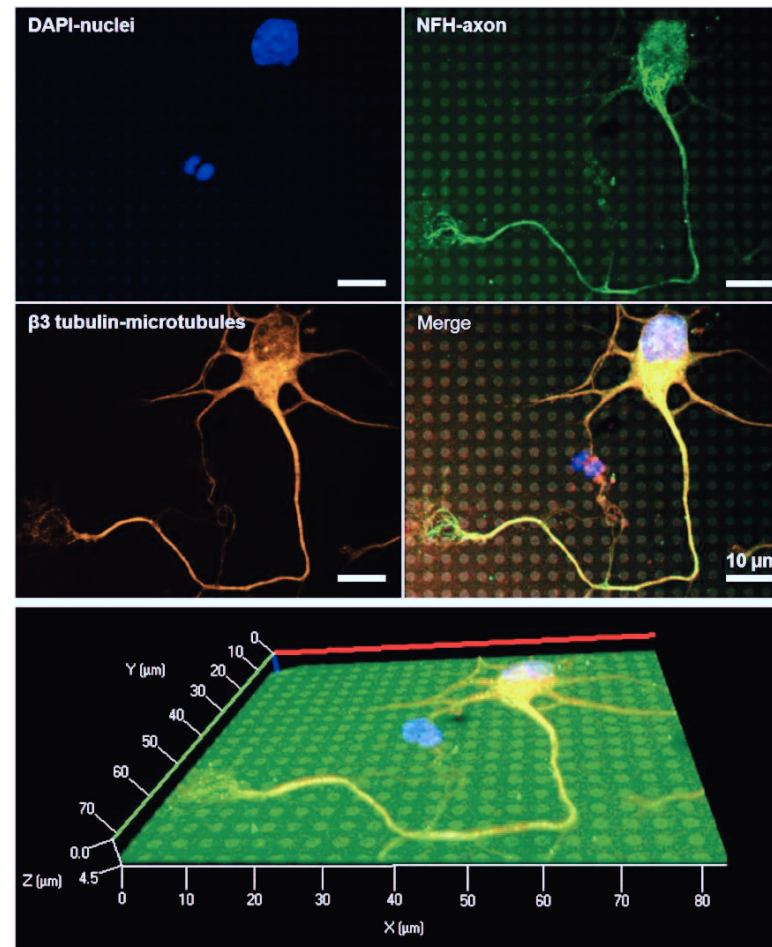
Figure 6.4. Fluorescent staining of a neuron grown on 100 nm high array A1 (1 μm diameter, 2 μm pitch). The top images show a neuron stained for DAPI (blue), NFH (green), β3 tubulin (orange), along with the merged image. In the lower image a 3D visualization of the same neuron was composed from 21 image stacks on z axis.

Cell adhesion on each of the topographies was determined by analyzing the soma area on the flat and patterned surfaces 3 DIV after seeding (Figure 6.5). The quantification of the cell adhesion was plotted for isotropic surfaces of arrays with 1 μm constant pitch at singular 100 nm height (B0.25, B0.5, B0.75, Figure 6.5a). Arrays with the pitch double the diameter (A0.5, A0.75, A1, A2) were used with 100 nm and 400 nm pillars height (Figure 6.5b). Soma areas on flat surfaces have the highest mean value (195.8 μm^2), but also a high error bar (62.1 μm^2). The trend shows that the adhesion area decreases on all 100 nm height (H 100 nm) structures with a mean value of 170.5 ± 47 μm^2. Moreover, significantly

lower soma area values were observed for nanostructures with 400 nm height (H 400 nm, 146.05 ± 39.4 μm^2). Distribution of soma areas on nanostructured OrmoComp substrates was much narrower when compared to cell soma areas on flat substrates. These results show that nanopatterned surfaces influence cell adhesion, an effect confirmed in many previous studies.[120,192,193] Neurons are not restrained by surface topography on flat OrmoComp surfaces. This leads to soma spreading with larger geometric areas as well as a greater range of areas. On nanostructured surfaces, the cells do not spread across the features, especially for the increased height (H 400 nm, Figure 6.5b). The nanostructures induce geometric constrains restraining the soma spreading. Z-stack images of the cell body and neurites are shown in Figure 6.5c-d. The 400 nm high arrays A0.5 (c), A0.75 (d), A1 (e), and A2 (f) influence the soma spreading on the surface. Vertical cell profiles show how cell bodies attach on the nanostructured arrays. Due to large area dimension (>100 μm^2) cell somas interact with the top of the structures, but also flat surfaces between the pillars. Figure 6.5e, f shows that neurites prefere to interact only with the flat surface between the pillars. In case of Figure 6.5c, d it seems that the neurite interacts also with the pillars tops, but this is not a conclusive affirmation due to poor resolution. A detailed investigation at higher resolution (SEM, FIB-SEM) of soma-pillars and neurite-pillars interaction will be discussed in the following part of this subchapter.
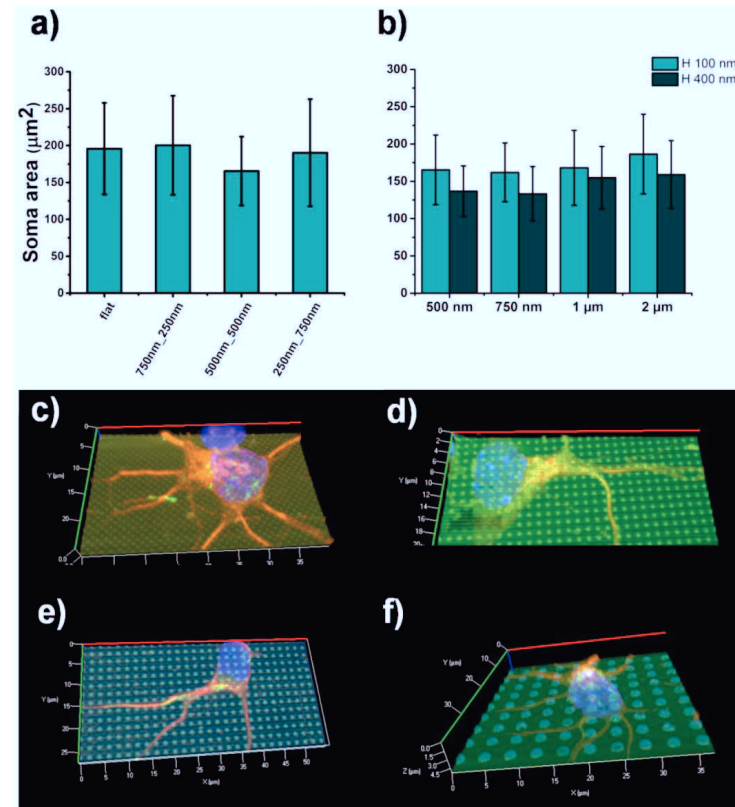
Figure 6.5. A quantitative and qualitative analysis of neuronal soma areas. The neuronal soma area quantification for flat and nanotextured surfaces with different heights (100 nm and 400 nm) and different dimensions: a) Arrays with 1 μm constant pitch (H 100 nm) and b) Arrays with pitch double the diameter (H 100 nm, H 400 nm). c-f) Z-stack compositions of cell soma on arrays with 400 nm high structures. Vertical profiles of cell somas show the cell-surface interaction with arrays: c) A0.5, d) A0.75, e) A1, f) A2.

Neuronal axon growth was also affected by nanostructured surfaces, Figure 6.6. It appears that neurons show a slight decrease in axon length (144.6 ± 54 μm) for all 100 nm high pillars compared to the flat polymer substrate, 169.4 ± 86.5 μm. This effect was opposite for 400 nm high structures, where longer axons were observed (213.8 ± 101 μm). Axon elongation increased with the increase in pillar size, and maximized on the A1 array (1 μm diameter, 2 μm pitch, H 400 nm). For A1 array, the axon length was twice as large as that on the flat surface. These results indicate a significant acceleration of axon outgrowth on the nanopatterned surfaces.
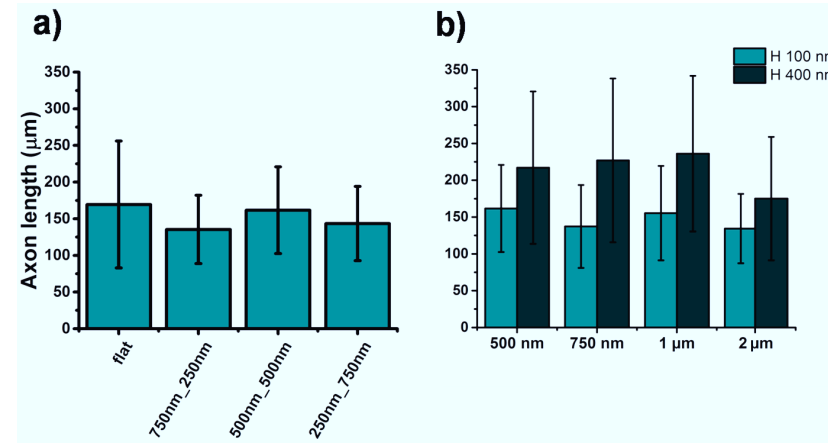
Figure 6.6. Characterization of neural development at 3 DIV regarding axon length for a) 100 nm high pillars with 1 μm constant pitch arrays and b) 100 nm and 400 nm height structures with pitch double the diameter.

Other neuronal morphological characteristics (neurite number, axon branching, and axon number of turns) were plotted in a 2D color code map for an easier observation of cell responses on all structures (Figure 6.7). The overall investigation showed a clear effect of the nanostructured surfaces compared to the flat OrmoComp. The neurite number was reduced on nanotopographic patterns (Figure 6.7a). The strongest deviation from planar samples, and therefore the strongest topographical effect was observed on the A1 array (H 100 nm). Interestingly, the same pillar design but 400 nm height (A1/H 400 nm) had values similar to the planar surface. However, all 100 nm height structures, except the A0.5 array, showed a lower neurite number then planar surfaces or higher pillars (H 400 nm). Regarding axon development, topographical effect induced an increase in both axon branching and axon turns (Figure 6.7b, c). Here, the A0.75/H 400 nm array exhibited the strongest deviation from the planar substrate, while B0.75/H 100 nm showed similar values (branching and turns). A clear tendency can be observed for all H 400 nm arrays which showed an increase in the number of axon turns, compared with all H 100 nm arrays and planar surfaces (Figure 6.7c).
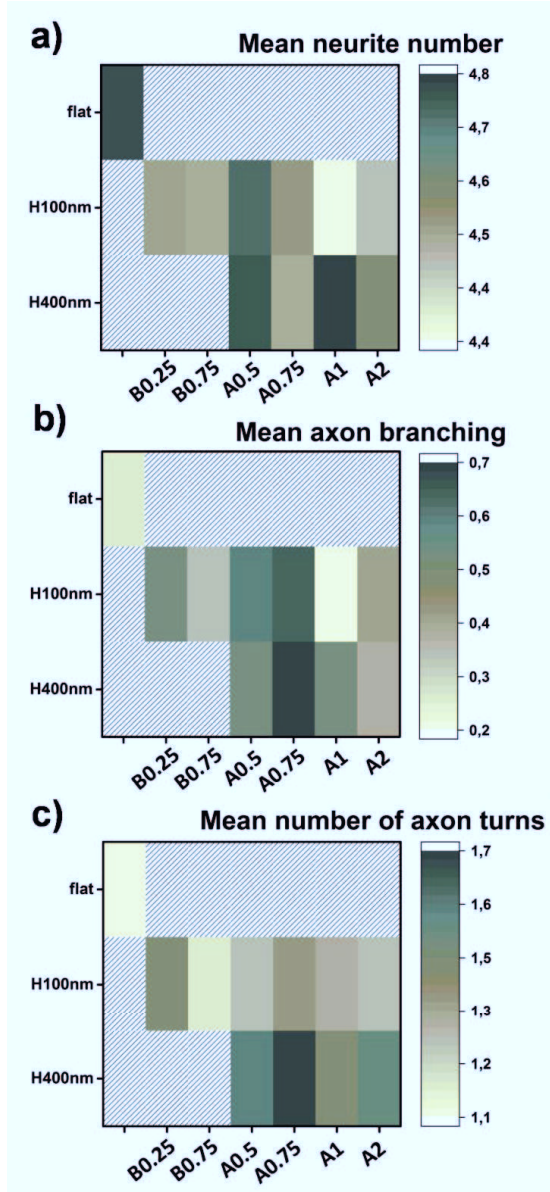
Figure 6.7. Analysis of neuronal growth regarding a) neurite number, b) axon branching, and c) number of axon turns. Surface topography induced a lower number of neurites on nanostructures, compares with the flat surface. Axon branching and turns were increased with the height of topographical structures.

The effect of isotropic topography on growth and its connection with different nanopillar heights was also characterized by SEM microscopy. The increased resolution provided additional data for describing the distribution of neural processes, growth, and interactions with pillars. Moreover, SEM characterization of the surface enabled the quantification of the increase in surface area by 3D structures. The total surface area is given by formula:

$$A_{total} = \frac{A_{lateral\ surface\ pillar}}{l^2} + 1$$

where l represents the pitch (center to center distance of two adjacent pillars) and the lateral surface area of the pillars ($A_{lateral\ surface\ pillar}$) was calculated with respect to their geometry. The structures with 100 nm height had a cylindrical shape, while the 400 nm height structures had a frustum-like geometry (Chapter 4). The lateral surface area of the H 100 nm pillars was $A_{lateral\ surface\ pillar} = 2\pi\ r\ h$ (where r=radius, h=height) and $A_{lateral\ surface\ pillar} = \pi\ h(R + r)$ for 400 nm height structures (h=height, r=radius at top, R=radius at bottom). As an example, the A1 pattern (1 µm diameter, 2 µm pitch) had a surface area increase of 8% for H 100 nm and 22% increase for H 400 nm, compared to the flat surface. Filopodia mainly interacted with the top of the pillars and upper pillar edges on 100 nm high structures, Figure 6.8 left image. In the case of 400 nm high nanostructures, the neurites interacted with the planar surfaces in between the pillars and they also adhered to the sidewalls (lateral surface) of the frustum (Figure 6.8). A detailed discussion on the influence of structure height with a focus on axon guidance is presented in the following subchapter).
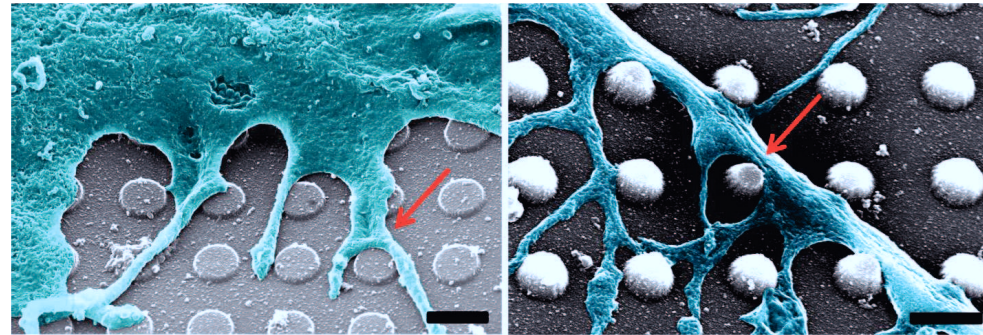
Figure 6.8. SEM micrographs of neurons cultured on 100 nm (left) and 400 nm high structures (right). Small projections react differently to the topographies: lower structure heights induce a wrapping of the pillar at the top, while for high structures the wrapping is done at the bottom sidewall (red arrows).

6.1.3. Axon initiation and path finding angle

Axon polarization is highly relevant in studies of topographical effects on neuronal morphology. Axon position defines the axis of neuronal migration, and it is important for the proper organization of the brain.[195] The effect of topography on axon guidance was assessed using neuronal cultures on different structures. Since the axon is highly dynamic throughout its development, so far it remains unclear whether this guiding effect originates from the oriented axon initiation or occurs later during axonal path finding. For this reason, the axon initiation angles were determined and compared with the final axonal alignment on the patterned surfaces. The initiation and path finding angles were measured using axon specific stained images (NFH staining) of single neurons, no networks or cell-cell connection were taken under investigation. Initiation angle was defined as the angle before the first change of axon direction. The angle of the axon's distal end was measured as the path finding angle. The analyses revealed that the presence of topographical signals causes a different response in the measured angles of the axon. Table 6.2 summarizes the initiation and path finding angle distribution.

Table 6.2. Polar plots of the initiation and path finding angles for all arrays. Counts are shown on the *y* axis scale with a maximum value of 60 for H 100 nm, and 90 for H 400 nm, n=200.

Array	Initiation angle		Path finding angle	
	H 100 nm	H 400 nm	H 100 nm	H 400 nm
A0.5				
A0.75				
A1				
A2				
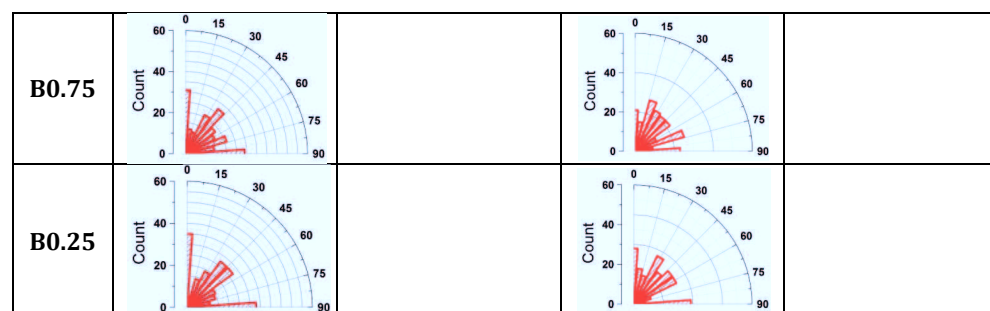
As shown in Table 6.2, a significant difference in axon distribution (initiation and path finding angle) was obtained for the two pillar heights. Cells were considered aligned if they had a 0° or 90° orientation. Flat substrates showed a random distribution (data presented below). On the other hand, nanostructured substrates showed an axonal outgrowth in a preferential direction. In the case of 100 nm high pillars, an orientation effect can be observed for axon initiation angle. The orientation effect is present for all the arrays, except A0.5, for at least 30 counted neurons at 0° or 90°. Cells tended to lose this orientation at the axon distal ends. Three of the arrays with the pitch double the diameter (A0.75, A1, A2) still induced an axon orientation relative to the pattern for at least 30 counts. Axons extending on higher pillars (400 nm) showed a directional preference with growth along the topographical features for all pattern designs. The axons demonstrated an orthogonal orientation (sharp peaks at 0° and 90°). For all arrays, the axons were mostly aligned to the orthogonal axes of the pillar areas. Moreover, the orientation was similar for the path finding angles. 400 nm high pillars showed a stronger guidance effect than the 100 nm high pillars.

6.1.4. Neurons alignment for different pillar heights

To understand the relevance of quantitative variation in topographical cues, neurons cultured on substrates were analyzed regarding the axon alignment. Since a significant difference was not observed for structures dimensions (diameter, pitch), but for the pillar height the investigation was focused on comparing the two structure heights. The length of the axon which followed the structures was quantified as a percentage of the total axon length. Axons were considered aligned to the pattern if the angles were 0° or 90° relative to the direction of the pattern.
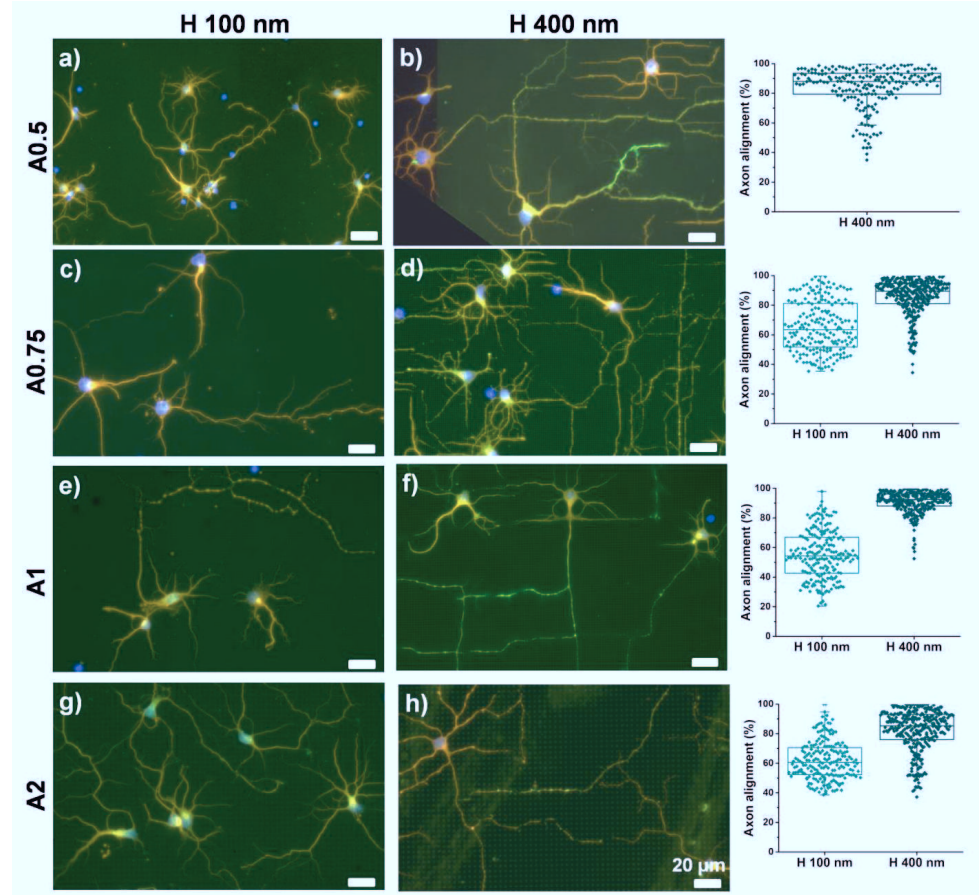
Figure 6.9. Qualitative and quantitative effects of the surface topography on the axon orientation. Fluorescence images of neurons on arrays with 100 nm: a) A0.5, c) A0.75, e) A1, g) A2 and 400 nm structures: b) A0.5, d) A0.75, f) A1, h) A2. The orientation of axons was plotted in the right part as axon alignment (%).

The effect of topography (pillar height) can be clearly observed from the fluorescence images in Figure 6.9a-h. Statistical analyses of the images are shown in the right part of Figure 6.9 for each array, except A0.5/H 100 nm array due to technical reason (low resolution). All 100 nm high pillars caused a lower value of axon alignment on the patterned surface (60.8 ± 15.5%) compared with the 400 nm pillars. For the latter, a mean value of 85.8 ± 12.1% demonstrates that axons followed the topographical cues with high fidelity. Best alignment was observed for the A1 array, with 91 ± 7.5% of the axon aligned with pillars surrounding. Here, the pattern has a square lattice which means the nearest neighbor and unit cell size (n) is located in the 90° direction and the distance to the second

nearest neighbor in the 45° direction is √2n. Since the only difference between the 100 nm pillars and 400 nm pillars is their height, understanding the guidance effect provided by the higher pillars is of great interest.

Figure 6.10 shows representative images of 100 nm and 400 nm structures and their influence on neurite contact. It appears that the growth cone explores mostly the upper part of the pillars for 100nm structures, Figure 6.10a, b. For 400 nm high structures, neurites grow and interact with the bottom of the structures and their walls. The SEM picture of 400 nm structures suggests the formation of small cell protrusions attached to the pillars and their involvement in the regulation of directionality (red arrow Figure 6.10c, d). The exploration of cell protrusions of their surroundings is connected to the topographical cues. If the next cue is close enough, the extension will be to that cue and so on. As a result, all 400 nm high structures induced protrusions and neurite alignment in the direction of the pattern since the pillars act as geometrical constraints providing directional guidance.
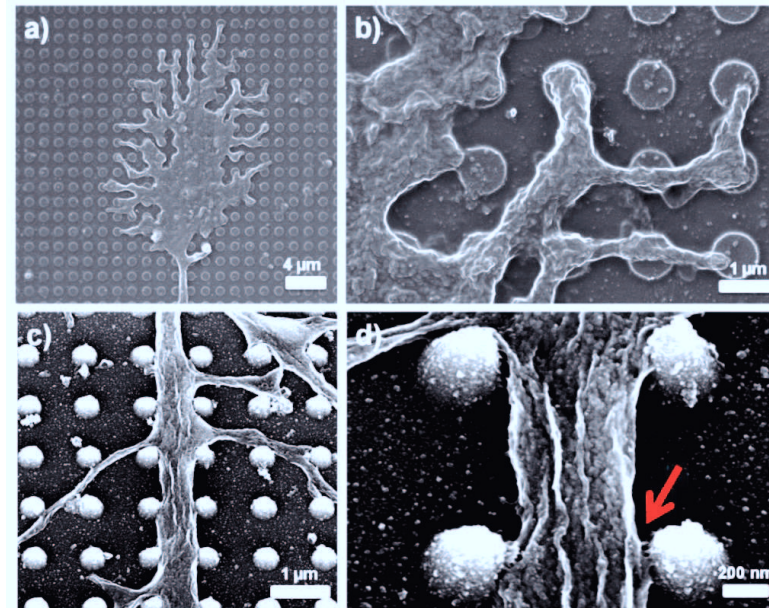
Figure 6.10. SEM micrographs of neurite exploration of 100 and 400 nm high structures. a) Growth cone interacts with the upper part of 100 nm high pillars. b) Zoom-in image of the alignment of cell filopodia relative to the topography. c) For 400 nm high structures, neurites interact mostly with the flat surface between the pillars and form adhesion contacts with the pillar walls. The red arrow indicates the contact between the cell's nanometer range protrusions and the pillar wall. Cells were fixated according to the resin protocol and imaged with 10 kV at 0° for a, b, and 30° for c, d.

6.1.5. Exploring the cell-nanostructure interface

SEM and FIB-SEM cross-sections were used to characterize the regions of the neuron-nanopillar interface. While the morphology of the cells can be easily imaged with optical microscopy, the real strength of the FIB-SEM method is the capability of 3D imaging cell adhesion to substrates and its interaction with nanopillars. Using ultra-thin resin embedding protocol, the 100 nm height structures were investigated (detailed description of protocol in Chapter 5).
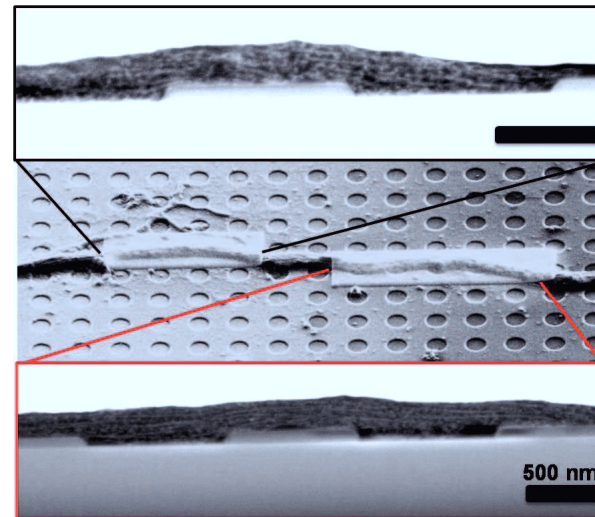
Figure 6.11. FIB cross-section of a neurite interaction with A1 array with 100 nm height.

Interestingly, cross-sections through neurites in contact with nanostructures revealed the microtubules orientation inside. Neurites formed a conformal contact with the top of the structures. However, this was not always the case for the bottom area of the structures. Here, the microtubules grow from top to top of the structures and only partially protrude to the bottom (Figure 6.11). Noteworthy, stained cytoskeletal protein fibers were aligned parallelly with the surface while showing deviations at the pattern edges. The contact between cell soma and nanostructure will be discussed in more detail for the different patterns as a function of their dimensions.

6.1.5.1. Arrays with pitch double the diameter

After FIB cross-sections, the cell soma-nanopillar interface was inspected using high resolution SEM. Due to the cell staining obtained through resin preparation, the cell membrane could be clearly defined and further analyzed.
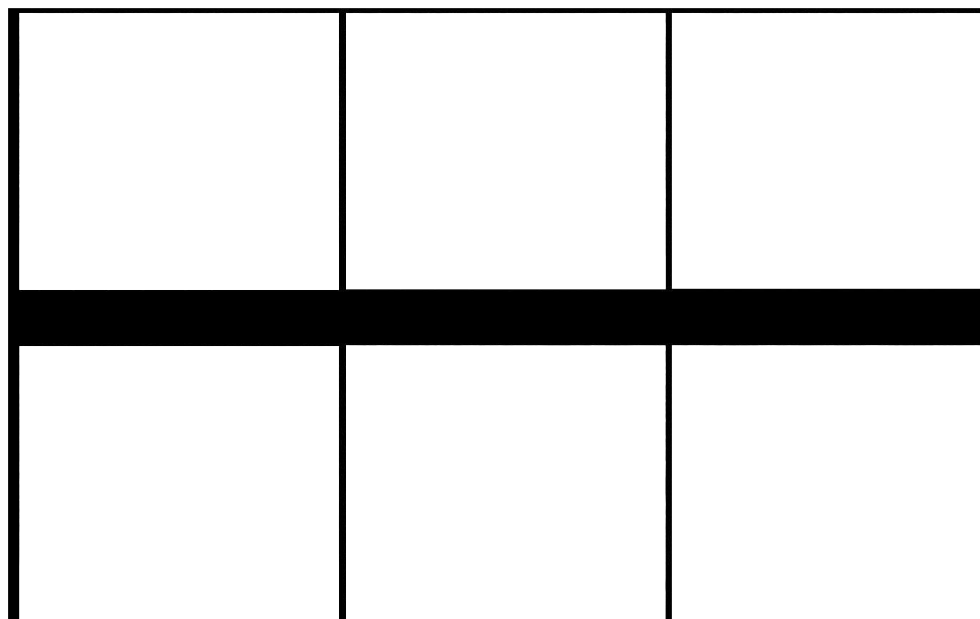
Figure 6.12. Cross-section images of flat surface (a) and 100 nm high structures interacting with the neuronal soma (b-f). The cells display a different cell membrane interaction on different pillar dimensions: b) A0.25, c) A0.5, d) A0.75, e) A1, f) A2.

The cell membrane interaction with 100 nm height structures (A arrays - pitch double the diameter) and flat surface is shown in Figure 6.12. Membrane did not adhere in a conformal way to the profile of the surface contours on flat surfaces. The adhesion contact was formed via discrete points, which maintained adhesion and cell morphology development. For the smallest dimensions (A0.25 array), the cell membrane did not to bend into the space between the nanostructures. The cells rather exhibited a close contact only to the top of the structures. Starting with A0.5 array, the cell membrane showed an increase interaction with the flat surface between the pillars. A quantitative analysis of cell membrane interaction with nanostructures is showed in Figure 6.13.

As shown in the schematic in Figure 6.13a the cell membrane was divided into four categories: membrane not in contact with the surface - "rest membrane" (grey color); membrane in contact with the pillars upper part - "top contact" (green); membrane in contact with the flat surface between the pillars - "bottom contact" (blue), and membrane that bends in between the pillars - "bending membrane" (orange). The bending was counted no matter if the membrane was in contact with the pillar sidewalls or suspended between the pillars. Quantification of the cell membrane bending was taken under investigation due to the fact that even if the membrane is not in conformal contact, the penetration of the membrane can still induce a high sealing resistance. This effect was observed when MEA-

based nanocavities were introduced. The nanocavities on microelectrode arrays was shown to obtain promising results in comparison to standard planar MEA systems. In particular, the nanocavities decrease signal loss by a high sealing resistance formed by cells covering the electrodes.[196,197] For an easier understanding of the array dimensions, the aspect ratio between the width and depth of the interpillar distance (nanoholes/nanocavities) will be given.

Cell membrane distribution was first characterized after normalization to the total membrane length (Figure 6.13b). The flat surface induced a membrane-surface contact of 48.6 % of the total soma membrane. This result shows that only 50% of the total membrane is in contact with the surface which is sufficient to provide stable cell adhesion.[26] For A0.25 (AR=2.5, width/height interpillar cavity) arrays, the membrane interacts preferentially with the top (33.2%), exhibits low bending (7.8%) and rarely contacts the surface between the pillars (1.7%). In the case of A0.5 (AR=5) array, the top contact dominates (26.7%), but an increase in bending (17.4%) and bottom contact (8.6%) was also observed.
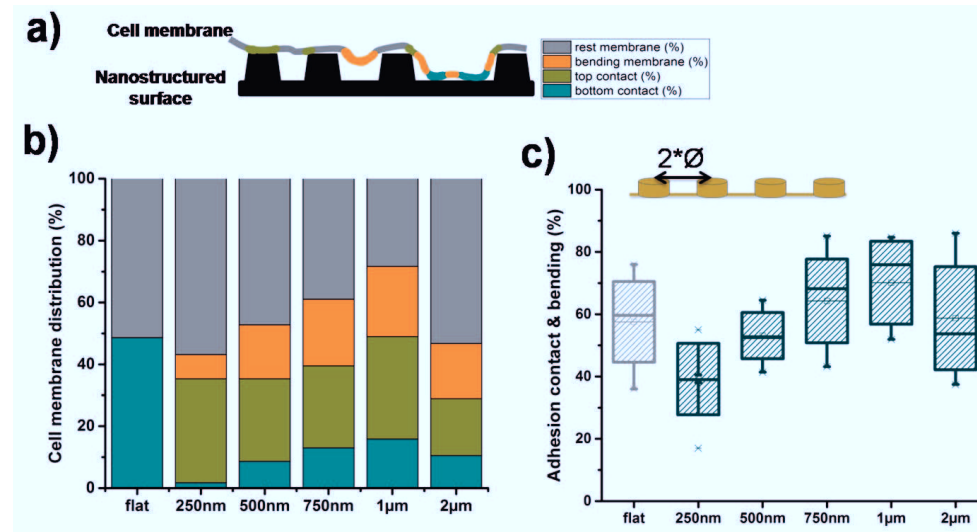
Figure 6.13. Quantification of the surface topography effects on the cell-surface adhesion contact. a) A schematic representation of the cell membrane interaction using color code. b) Cell membrane distribution after normalization to the total membrane length for different patterns. c) Surface area increased by the nanopillars (calculated from FIB cross-sections, $A_{FIB} = A_{flat} + A_{width \, x \, length \, pillar}$) was considered in quantification. The increased surface area of A0.25 area (20%) compared with flat surface did not lead to a better cellular contact, while for A1 array (5% surface area increase) 70% of the surface showed cell contact or bending between the pillars.

Increasing the structure dimensions (A0.75, AR=7.5) lead to an almost equal contact to the pillars' top (26.5%) and bending (21.5%). The contact with the surface between the pillars was also increased to 13%. The best result of membrane-surface interaction was obtained for A1 (AR=10) structures. Only 28.3% of the membrane was not in contact with the surface. The top contact reached a value of 33.1%, while the bottom contact showed an increase to 15.9%. The value for the bending was close to that of the A0.75 array with 22.6% of the membrane interaction. A reversion of the trends was obtained for the biggest structures dimensions A2 (AR=20). Although, A2 array induced an equal distribution for the membrane contact (18.4% top contact, 17.8% bending, and 10.5% bottom contact), it did not improve the cell-structures contact. Since the aim of the nanotopography implementation is often to increase the cell-surface contact area, the next quantification was normalized to the total surface length (Figure 6.13c). The larger surface area can provide more contact area for cells to adhere. The total surface area was calculated for each structure using the 2D FIB cross-sections by adding the length related to the pillars sidewalls (width x height) to the length of the flat surface:$A_{FIB} = A_{flat} + A_{width\ x\ length\ pillar}$. The flat surface showed a 57.5 ± 13% coverage of the cell membrane in contact. Highest surface area (+ 20% compared with the flat surface) was achieved by fabrication of A0.25 array. Unfortunately, the increased surface area did not lead to an increased cellular contact. Only 39.2 ± 11.5% of surface was in contact with the cell membrane. A small increase in surface area was shown for A0.5 array (surface area increased by 10% compared with the flat surface). Even though 53.1 ± 7.4% of the surface was in contact with cell membrane, the value was still smaller compared with the flat surface. This threshold was exceeded for A0.75 array (surface area increase of 8%) with 64.3 ± 13.4%, and A1 array (surface area + 5%) with 70.1 ± 13.3% of surface length in contact or bending between the pillars. A2 array (+ 3% surface area) showed a value closer to the flat surface (58.7 ± 16.5%). Again, the biggest adhesion area was obtained for A1 array. In the presented quantitative analysis, the effect of the surface area on the cell membrane response can be easily observed. Moreover, the high increase of surface area was shown not to improve the cellular adhesion on the nanometer scale structures and could be related to the low aspect ratio of the interpillar cavity (AR=2.5).

6.1.5.2. Arrays with constant pitch
Above, the effect of arrays with same pillar diameter and interpillar distance was investigated. However, changing the ratio between the diameter and the interpillar distance gives the opportunity to investigate the cell-nanostructures interface for another perspective. Therefore, nanopillars with increasing diameter but constant pitch were used.
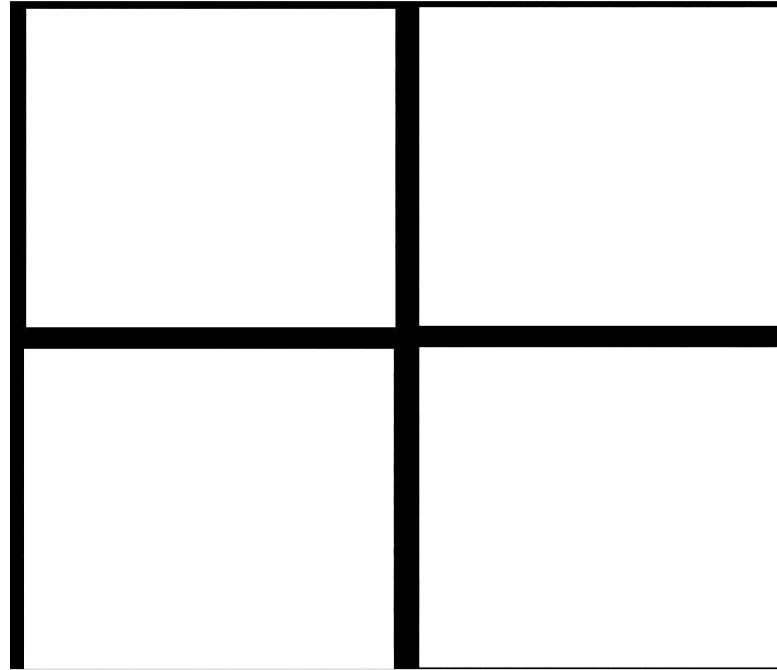
Figure 6.14. Cross-section of the neuronal interface with the flat surface and (a) 100 nm high structures: b) B0.75, c) B0.5, and d) B0.25.

For these structures, the surface area of all nanopatterned substrates is equal and 10% larger than for the planar surface. The array A0.5 (here B0.5) was used as an intermediate between B0.25 (250 nm diameter, 750 nm interpillar distance) and B0.75 (750 nm diameter, 250 nm interpillar distance) structures. The FIB cross-section of the cell-surface interface shows the cell membrane mainly had a close contact with the surfaces of all nanostructures (Figure 6.14). Small interpillar distances for B0.75 (AR=0.25) appeared not to induce membrane bending (Figure 6.14b). On the other hand, large interpillar distances (B0.25, AR=7.5) showed a distinct bending of the cell membrane between the pillars and an increased bottom contact compared with the other two patterned surfaces, Figure 6.14d.
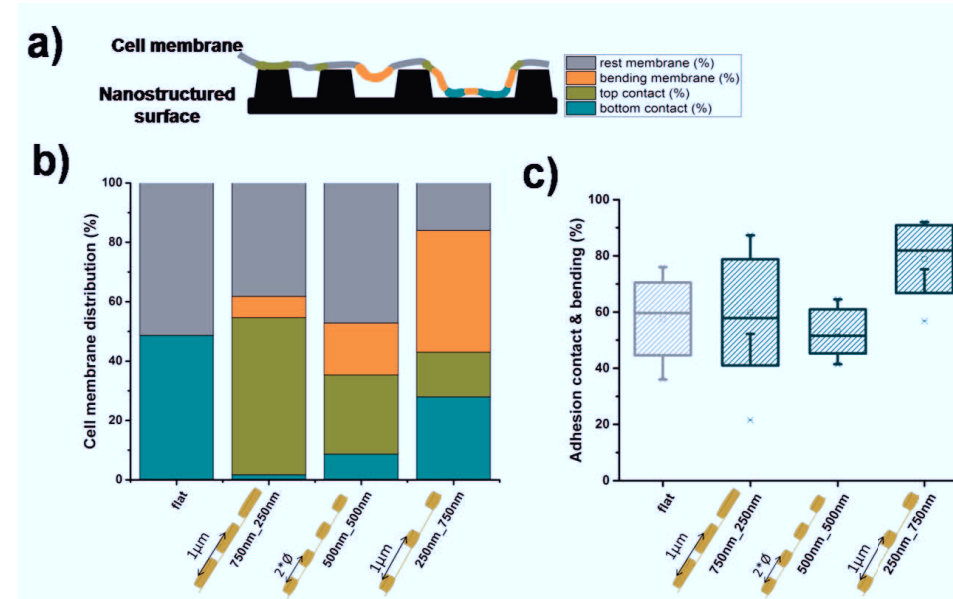
Figure 6.15. Quantification of the surface topography effects on the cell-surface adhesion contact. a) A schematic representation of the cell membrane interaction using color code. b) Cell membrane distribution after normalization to the total membrane length. c) Surface area was used for normalization and shows that the nanotopography (10% area increase) can increase the adhesion contact.

Same normalization as the arrays with pitch double the diameter was done considering the total cell membrane and surface area. Schematic representation of the cell membrane interaction with the surface is shown in Figure 6.15a. In this case, cell membrane contact normalized by the total length showed the strongest adhesion for B0.25 array (Figure 6.15b). 15.1% of the cell membrane interacted with the pillars' upper part, 27.9% with the flat surface between the pillars, and 40.9% of the membrane length bent between the pillars or pillars' wall. Opposite results were observed for cells interacting with larger diameter pillars (750 nm) with small interpillar distance (250 nm). The membrane interacted mainly with the top part of the pillars (52.9%) while its bending (7.1%) and interaction with the bottom parts (1.7%) were far less pronounced. Still, both of the arrays (B0.25 and B0.75) showed a bigger adhesion contact then B0.5 array (26.7% top contact, 17.4% bending membrane and bottom contact 8.6%). The quantification regarding surface area was also an important point of the presented investigation (Figure 6.15c). In all three cases, the nanostructured surface had the same increase in the surface area compared with the flat surface (+10%). Nanostructured surfaces increased cell adhesion on B0.75 and B0.25 arrays, while the B0.5 showed similar adhesion values as the flat surface. Flat surfaces induce an area coverage of 57.5 ± 12.9%. B0.5 had a small decrease in membrane

adhesion (53.1 ± 7.4%). Since B0.75 array mainly showed an adhesion contact on the large pillar top, a value close to that on flat surfaces was obtained, 59.9 ± 18.9%. These results can be correlated with the low aspect ratio (2.5), as in the case of A0.25 array. A large improvement was shown for B0.25 array. 78.8 ± 12% of the surface was covered by the soma by either a conformal contact or bending (between the pillars). It was interesting to observe the bending membrane for the three topographies. The bending increased 17 times for B0.25 array, compared with B0.75 demonstrating the importance of the pillar diameter and interpillar distance.

An extensive investigation of the morphological responses such as neuronal adhesion and development on isotropic surfaces was performed in this subchapter. The results indicate a distinct morphological response of each array separately, but an obvious difference was confirmed for the structure height while for the structure diameter and pitch the difference was far less pronounced. In general, chemical, topographical, and mechanical cues can strongly influence the neurogenesis caused by biochemical signaling and force generation.[36] Here, the chemical and mechanical cues were minimized in order to observe the neuronal response to the specific topography systematic investigation. The PLL coating facilitates cell adhesion through unspecific electrostatic interactions with the glycocalyx of the cell membrane without being involved in chemical signaling.[198] The change of the stiffness OrmoComp material due to the nanostructures can be considered insignificant, due to the low aspect ratio of structures (height to diameter). One of the advantages of using OrmoComp polymer replica is its biocompatibility resulting in high cell viability. No significant changes were observed compared with typically used control substrates even for long term primary neuronal cultures. The quantification of cell viability showed the same values independent of the surface topography. This can be related to the surface wettability. The surface contact angles showed similar values: 70° for planar and 80° for patterned surfaces. No surface modification was applied before PLL coating (no O_2 plasma).

The planar surface was taken as a relative standard (2D *in vitro*). In general, cells change their morphology according to the topography of their surroundings. The most common morphological changes in neurons cultured on patterned substrates are increased neurite length and alignment, decreased number of neurites, and faster development.[199,200] These enhancing properties of nano- and micro-structures on neurite development were previously reported for various 3D-geometries such as beads,[39] pillars,[47] fibers,[201] or posts.[202] Similar responses were observed in the presented experiments with a clear difference for structures height. First, the nano-topography caused a reduction of the cell-surface contact area. Cell adhesion on nanopatterned surfaces stabilized the actin assembly, thereby reducing the need to spread across the surface. Cell soma size showed a reduction of 25% for 400 nm high structure arrays compared with flat surfaces. An inhibition of neurite formation and branching was also observed. The reduced soma size and neurite number was further correlated to the enhancement of neurite outgrowth.[37,38] The axon

related statistics were found to be significantly increased on 400 nm high pillar arrays. Increased axon lengths with a higher number of branches and turns was observed compared with flat and 100 nm surfaces. These results can be related to the total surface area increased by the 3D structures due to pillar sidewalls (cylindrical and frustum geometry). For 400 nm nanopillars, the topographical information given was significantly larger than in the case of corresponding 100 nm nanopillars. The topography height-sensing ability of neurites arises from the interplay between filopodia adhesion and neurite bending.[50] Sufficient adhesion of the filopodia onto the substrate (represented by a threshold number of contacting filopodia) is a pre-condition for advancement of the growth cone. It was clearly observed that, on 400 nm high pillars, the growth cone migrates onto the flat surface between the pillars but forms firm adhesion points with the nanopillars walls. These adhesion points generate internal traction stress through substrate adhesion and cytoskeleton contraction, which balances the neurite tension pulling on the growth cone.[115] In case of 100 nm high pillars the growth cone interacts mainly with the upper part of the pillars. Moreover, the axons on 400 nm high structures had a good alignment and a high fidelity orthogonal orientation on the pattern. Interestingly, the increasing neurite extension and alignment were observed to saturate on A1 array (1 µm diameter, 2 µm pitch). The higher axon alignment on high pillars can be induced by the local membrane deformation initiated by the mechanical strain. The F-actin adhesions can then be concentrated at the pillar sides due to receptors triggered by mechanical forces clustering.[115] In this case, the formation of a robust F-actin network might allow to counteract the actin retrograde flow in the aligned filopodium, leading to its stabilization.[50]

A systematic investigation of the actual interface between the cell soma and 100 nm nanostructures was performed. For small, dense nanostructured surface (A0.25, AR=2.5, width/height interpillar cavity) the preferred interaction of the cell membrane occurred via the top of the pillars. For larger arrays (A0.5, AR=5) or larger interpillar distances (B0.25, AR=7.5) the cell membrane showed an increased contact with the flat surface between the pillars. Investigation of the cell membrane showed that it formed strong adhesions on flat areas as well as the nanopillar sidewalls and wrapped around these nanopillars, exception A0.25 area. The B0.25 geometry induced a considerable increase of the adhesion contact by 55% compared to the A0.25 array, and 40% compared to the flat surface.

The theoretical calculation addresses the engulfment-like process of the 3D nanostructures by the cell membrane exploring the characteristics that effect wrapping and compare to the experimental results. Details about calculation method can be found in Karandeep et al.[203] The model of nanopillar wrapping of neuronal membrane was developed using a continuum model in order to obtain the different wrapping transitions after calculation of membrane deformation energy and adhesion energy. The deformation energy of the lipid bilayer was calculated using Helfrich's curvature-elasticity Hamiltonian,[204]

$$E_d = \int_{A_{total}} dA \left(\frac{\kappa}{2} (2H + c_0)^2 + \bar{\kappa} K \right) + \sigma \int_{A_{total}} dA$$

with bending rigidity κ, Gaussian saddle splay modulus $\bar{\kappa}$, membrane surface tension sigma, and spontaneous curvature c_0. The mean curvature $H = (c_1 + c_2)/2$ and the Gaussian curvature $K = c_1 c_2$ can be obtained from the two principal curvatures c_1 and c_2 at each point of the membrane. The Gaussian saddle splay modulus is only relevant if topological changes occur, e.g. if nanopillars detach from the membrane. The direct contribution of the shear modulus for cytoskeleton on nanopillar adhesion was ignored. Moreover, was assumed as flat membrane and hence c_0 = 0. The deformation-energy cost for the membrane was necessary to be overcomed by the adhesion-energy gain for the contact between the nanopillars and the membrane E_{adh}:

$$E_{adh} = -w \int_{A_{adh}} dA$$

with adhesion strength w of the membrane. The adhesion energy gain depends on the physico-chemical properties of the nanopillar surface, and the biochemical composition of the membrane. For the radius r of the nanopillar, pitch l (center to center distance of two adjacent pillars), height h, and the wrapped nanopillar height z (Figure 6.16a),

$$E_d = \frac{\kappa \pi z}{r} + \sigma (l^2 + 2\pi r z)$$

and

$$E_{adh} = -w(\pi r^2 + 2\pi r z)$$

Wrapping fraction f_w (adhered nanopillar area/total area) for the nanopillar was introduced:

$$f_w = \frac{\pi r^2 + 2\pi r z}{l^2 + 2\pi r h}$$

Minimization of the total free energy $E_t = E_d + E_{adh}$ as function of f_w with $c_0 = 0$ showed the optimal wrapping state of a nanopillar. For constant σ, l, r, and h, wrapping energies as a function of f_w were calculated. No wrapping was obtained for w = 0, where the membrane was hovering on the nanopillar. For $w > 0$, the membrane covers only the top surface of nanopillars, characteristic to a partially-wrapped state (PW). Increasing the adhesion strength led to the envelopment transition from the partially-wrapped to the completely-wrapped state (CW) at adhesion strength w_2. For 0 $<w <$ w_2, a stable PW states was observed, characterised by the global minimum of the energy. For $w > w_2$, a stable CW state was found. The transition between the PW and CW state is indicated by W_2, and characterized by an energy barrier $\Delta E_{barrier}$. As w increase, the energy barrier between the PW state and the CW state vanishes, characterised by the spinodal S_{22}. Beyond the value w_2, membrane spontaneously wraps. The wrapping energy as a function of f_w was plotted, Figure 6.16b. The blue line represents the W_2 transition, when the energy of the PW state is

equal to the CW state at $f_w = 1$, as shown by the upper blue dot. The orange line represents the spinodal S_{22}, when the energy barrier vanishes and the membrane spontaneously wraps, as shown by the lower blue dot at $f_w = 1$. The height of the energy barrier, $\Delta E_{barrier}$, can be characterised by barrier height for $w = w_2$. Moreover, the energy barrier can be calculated by subtracting the difference between the wrapping energies when the curved part of the nanopillar is wrapped and when just the top surface is covered by the membrane, at $w = w_2$.[203]
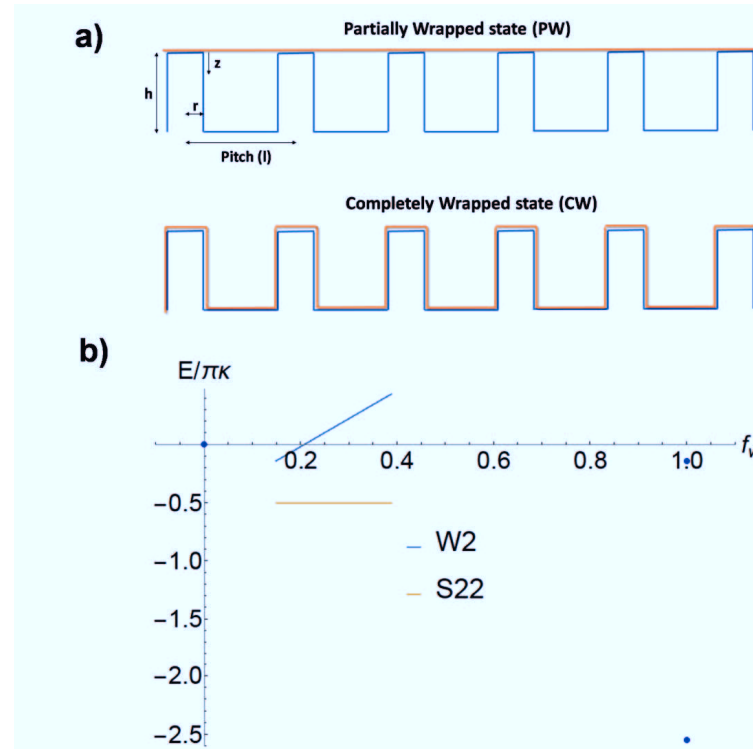
Figure 6.16. a) Schematic representation of partially-wrapped (PW) and completely-wrapped (CW) for pillar geometries where r represents the radius of the nanopillar, l the pitch (center to center distance of two adjacent pillars), h -height, and z the wrapped nanopillar height. b) Wrapping energy as a function of wrapping fraction for (PW) to the (CW) state transition.

Using the wrapping energy diagram, wrapping phase diagram for surface tension σ and adhesion strength w for different experimental geometries was obtained, Figure 6.17. Lines with a higher slope require a lower adhesion strength w to completely wrap of a nanopillar. States to the left of a line are PW, while on right of a line the CW state are shown.

As observed in the plot, the W_2 for B0.25 was observed to be the easiest to wrap amongst the four geometries.
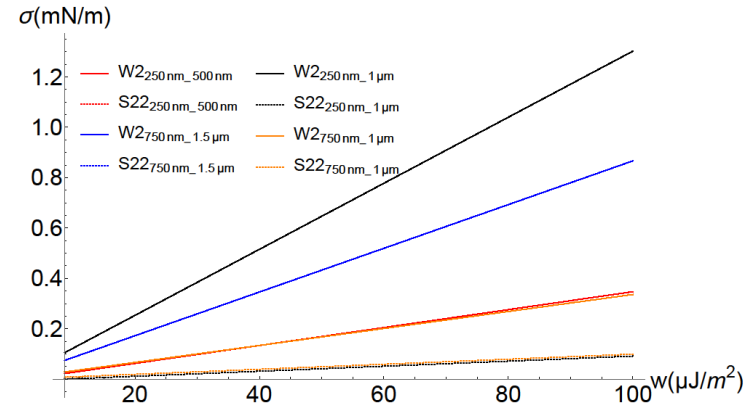
Figure 6.17. Phase diagram for the W_2 transitions (from PW to CW) for different experimental geometries. The dotted lines represent S_{22} transitions. The larger the slope of the line, the less w the membrane requires to wrap the nanopillar completely.

Further, a wrapping phase diagram was obtained for adhesion strength w as a function of pitch l and radius of the nanopillar r. The membrane surface tension was constant $\sigma = 0.12$ mN/m,[205,206] with a bending rigidity $\kappa = 66$ kT,[207] and height of the nanopillar $h = 100$ nm. Figure 6.18 plot different w values (lines), w=10, 20, 30, 50, and 100 μJ/m^2, [208,209] from left to right respectively, indicating the PW and the CW states in the wrapping diagram. The states which are on left to a black line are CW and to the right are the PW corresponding to that adhesion strength w. Marked yellow points are the combinations of l and r values obtained in experimental study. Depending on the w values, the geometries used in experimental studies could be PW or CW. For example, if $w = 30$ μJ/m^2, B0.25, A0.5/B0.5, and A0.75 present CW states, while the other geometries are PW.
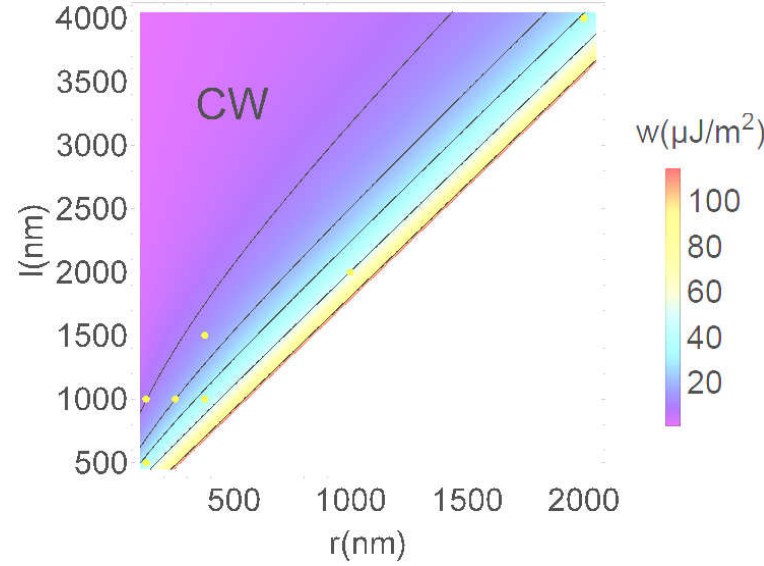
Figure 6.17. Adhesion energy (*w*) as a function of pitch (*l*), and radius of the nanopillar (*r*). Black lines represent contours for different *w* values, viz., *w*=10, 20, 30, 50, and 100 µJ/m², from left to right respectively. Left of the black line is a CW and to the right is a PW state. Yellow dots indicate the experimental geometries.

Hence, a continuous increase of *l* can induce a complete wrapping. However, from experimental studies was observed that the degree of wrapping decrease for A2 area, where the surface is closed to the flat substrate. For this reason, the surface area was taken under investigation and the adhesion energy was reploted, Figure 6.18. The relative nanopillar adherent area as compared with the slat surface area is given by the formula:

$$A_{adh} = \frac{2\pi r h}{l^2} + 1$$

As above, the black lines represent contours for different *w* values, viz., *w*=10, 20, 30, 50, and 100 µJ/m², from left to right respectively. States left to the line are PW and right to the line are CW states. Yellow points indicate the geometries used for experimental study. White area on the right represents the inaccessible region due to geometrical constraints. We also plot maximum adhered area contours for corresponding *w* contours, as shown by white lines in the plot. A_{adh} present maximum values for low *r* and low *l*. Increasing *r* and *l*, the approach the flat surface regime was implemented. For example, if *w* = 30 µJ/m², B0.25, A0.5/B0.5, and A0.75 are all CW states, but A0.5/B0.5 has the maximum nanopillar area adhered, relative to the flat surface area, followed by B0.25 and A0.75, respectively. Similarly, for the PW states, A0.25 area has the maximum A_{adh}. In conclusion the wrapping model fits with the experimental observations convincingly. Furthermore, a prediction for other geometries could be calculated for best possible wrapping.[203]
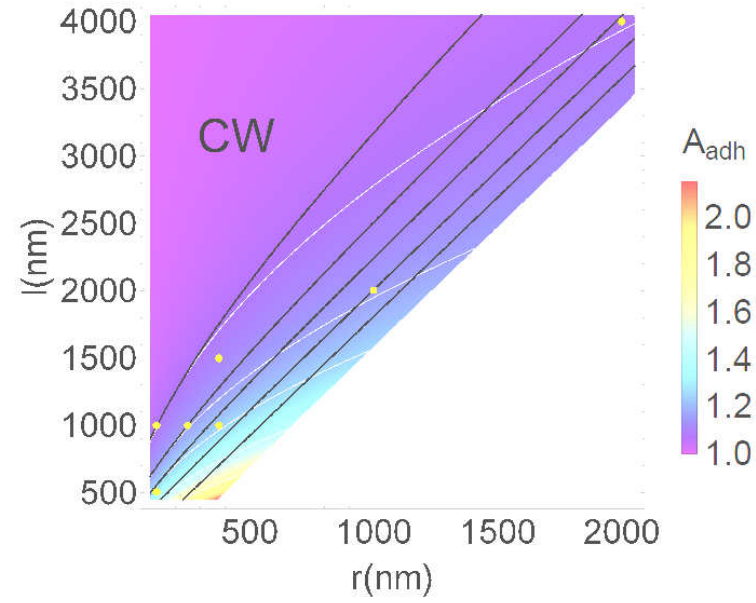
Figure 6.18. Area adhered by the membrane with respect to the surface area A_{adh}, as a function of pitch l, and radius of the nanopillar r. Black lines represent contours for different w values, viz., w=10, 20, 30, 50, and 100 μJ/m² , from left to right respectively. The white lines represent maximum A_{adh} for each of the w values. The experimental geometries are shown with yellow dots. White region in the right is the inaccessible due to geometrical constraints. Left of the black line represents CW, and to the right are shown PW states. For each completely wrapped state, the maximum A_{adh} can be read out. Each black line (different w values) requires different geometries for the new maximum A_{adh}, as shown by the white lines.

6.2. Interactions of neurons with anisotropic structures on different polymeric surfaces

6.2.1. Patterning and guidance of neurons on linear gradient nanosurfaces

A step forward was taken from homogeneous arrays towards line-based patterns at the nanoscale. Some fundamental studies showed that line-based topographies help to elucidate the mechanism behind the directional pathfinding of neurites.[42] A grooved architecture, due to its ability to guide cell alignment, is of particular interest for tissue regeneration. The general response to such topographic rippled features is cellular alignment and elongation along the groove direction. Additionally, neurites can grow either parallel or perpendicular to the micro/nano-grooves depending on the depth and width of these structures.[42] Gomez et al. showed that 2 μm lines were more effective at stimulating axon polarization in hippocampal neurons than chemical ligands. Also, a decrease in the distance between lines (1 μm) showed a more efficient polarization than 2 μm lines.[210] In the work of Park et al. the optimum distance to induce neurite directionality was found to be 4.5 μm (compared to 3, 6, 9, 12 μm interpillar distances).[202] Taking these investigations into account, a gradient array was designed in order to compare the influence of different interpillar distances on neuron alignment and polarization. The gradient array was designed to have a constant increase towards final interpillar distance of 1 μm (G1, slope $0.15 \cdot 10^{-3}$), 4 μm (G4, slope $0.75 \cdot 10^{-3}$), 10 μm (G10, slope $1.95 \cdot 10^{-3}$), and 20 μm (G20, $3.95 \cdot 10^{-3}$) along the *x* axis (mm). The diameter of structures was constant (250 nm), together with the pitch on the *y* axis, 500 nm. The four topographies were designed and combined to form a 1 x 1 cm four-quadrant grid to facilitate the acquisition of data for each design for the same neuron culture. Each quadrant consisted of an array of structures described above was separated from neighboring topographies by unpattern gaps (Table 6.3).

Table 6.3. Dimensions of the gradient design.

Gradient design	Name	Diameter (μm)/Pitch *y* axis (μm)	Pitch *x* axis (μm)
Linear gradient (Height 100 nm)	G1	0.25/0.5	0.5 – 1.25
	G4	0.25/0.5	0.5 – 4.25
	G10	0.25/0.5	0.5 – 10.25
	G20	0.25/0.5	0.5 – 20.25

6.2.1.1. OrmoComp nanosurface

Immunostaining of axons (NFH), microtubules (β3-tubulin), and nuclei (DAPI) was used to image the response of neurons on gradient arrays at a large scale (Figure 6.19). The quantitative cell-gradient interaction was analyzed for these images. To determine the

relationship between axon length and axon alignment to the lines, the angle that the axon formed with the pattern lines was measured. Neurites were considered "aligned" if they were extensively oriented within 10° of the target axis (α). Neurites growing in the direction of the lines was defined as a parallel alignment.
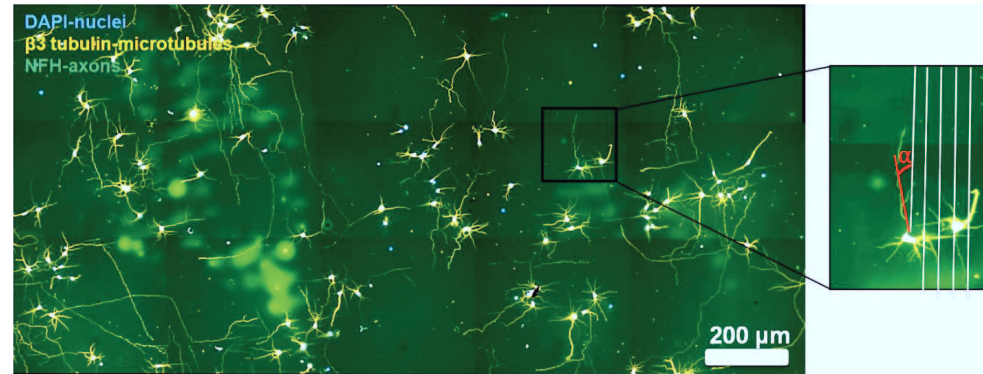
Figure 6.19. Large area fluorescence image of a gradient array. For alignment analysis, the axon angle that was defined depending on the described line (schematic white lines in the right image). Angle (α) less than 10° defines an aligned axon (red line) along the nanostructures (parallel direction).

Additionally, the four interpillar distances (G1-G20) in the beginning of each gradient represent an isotropic pattern: 250 nm diameter, 250 nm interpillar distance. The interactions of the cell membrane with the isotropic pattern was described in subchapter 6.1. The membrane distribution showed a low adhesion of the cell soma, with a 39.2 ± 11.5% contact between the cell and the nanostructures. A significant increase in the cell membrane-surface adhesion was obtained for B0.25 array (250 nm diameter, 750 nm interpillar distance), 78.8 ± 12%. This result shows that a larger interpillar distance was beneficial for cellular adhesion. Larger interpillar distances starting with 1 μm are expected to have a similar cellular adhesion. Additionally, a large interpillar distance of the anisotropic nanopillar array can induce guidance during the neurite outgrowth. Axons were considered aligned in the direction of the lines (parallel) at 0° and all angles of axons were taken under quantification. Figure 6.20 shows the polar plots of axons distributed on different patterns and representative fluorescent images. Axons on unpatterned OrmoComp surfaces show no directional preference of axon outgrowth (Figure 6.20a). Axon distribution in the case of G1 had a preferred orientation to the 0°, compared with the other patterns. Assuming that the fidelity of alignment to the 0° direction is an indicator of neurite preference for the *y* axis (line), axon directionality was quantified (Figure 6.20f). Interestingly, the axons preferential direction for the G1 array was in the parallel direction (40%). The percentage of axons in the perpendicular direction was equal to that of the

axons in a random direction (30%). In the case of the G4 area the directionality decreased for parallel and perpendicular direction to 27.5%, and 20%, respectively. The G1 pattern had the strongest influence on the axonal guidance since most of the axons had a parallel direction on the nanostructures. Moreover, the parallel orientation induced by the trenches topography (y axis) was preferred by the axons in detriment to the gradient slope (x axis). Nanopillars with larger distances (G10 and G20) showed a severe reduction in alignment that approached the axon distribution on a flat substrate (Figure 6.20).
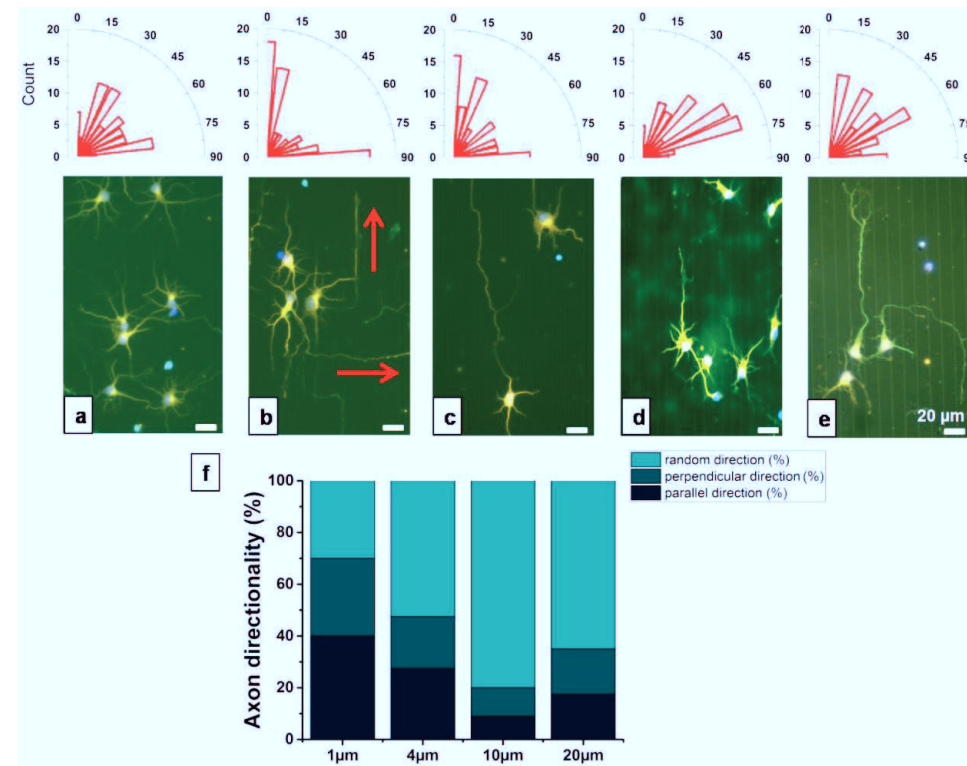
Figure 6.20. Polar plots and representative fluorescence images showing the distribution of axons on flat (a) and nanostructured substrates with different interpillar distances: 1 µm (b, G1), 4 µm (c, G4), 10 µm (d, G10), and 20 µm (e, G20); n=80. f) Axon alignment quantification shows that the guidance effect presents a preferred nanostructured area (G1) with 70% of the axons in the parallel or perpendicular direction of trenches (red arrows). G4 induced a ~50% guidance of the axon to the parallel or perpendicular direction, while for G10 and G20 areas the guidance effect was severely reduced.

Additionally, SEM images revealed the interaction of the cell body on different interpillar distances and neurites elongation along the nanostructures, Figure 6.21. A

smaller interpillar distance induced a rather elongated soma (Figure 6.21a), compared with cells cultured on G4 and G10 patterns (Figure 6.21b, c). Also, it can be observed that filopodia align along the nanostructures on the y axis, Figure 6.21d, e.
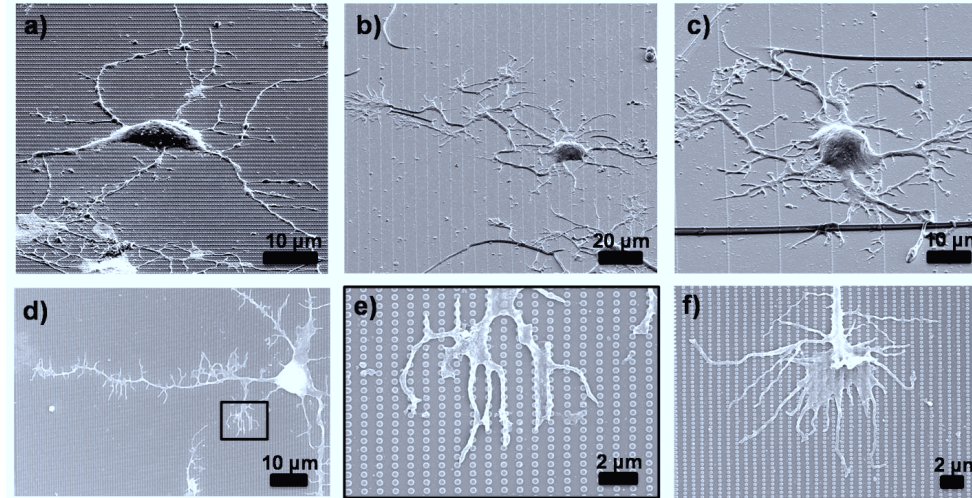
Figure 6.21. SEM images of primary neurons interacting with anisotropic surfaces. Cells have a slightly elongated soma on the G1 area (a), compared with cells on the G4 area (b), and G20 (c). d) Neuronal filopodia tend to align along the nanostructured surface on the G1 area. e) Zoom-in image of filopodia alignment where the cell mainly interacts with the top of the nanostructures. f) Image of the growth cone with corresponding filaments that interact in all direction with the nanostructures (G1 area). All SEM images were recorded with 3 KV at 52° tilt for a)-c) and 0° in case of d)-f) images.

In addition to the axon alignment, the gradient array was investigated regarding the neurite number and the axon length, Figure 6.22. There are no significant differences in the neurite number on the nanostructured arrays, no matter the interpillar distance (Figure 6.22a). Cells cultured on flat surface showed an average neurite number of 4.3 ± 1, while similar values were obtained for all nanopatterned surfaces: 4.4 ± 1.2 for G1 with, 4.4 ± 1 for G4, 3.8 ± 0.9 for G10, and 4.1 ± 0.8 for G20. Axon growth was affected by the gradient nanostructured surfaces, Figure 6.22b. Small pillars interdistances of G1 and G4 arrays induce an increase of the axon length from 149 ± 76 μm mean value for flat surface to 195 ± 109 μm (G1) and 158 ± 90 μm (G4). In accordance with the alignment results presented above the arrays with 1 μm and 4 μm interpillars distances showed that the topography of the anisotropic nanopillars could not only align the axons, but also elongate the axon outgrowth. Larger interpillar distances present a decreasing tendency of the axon length values to 92.9 ± 25.3 μm (G10) and 129.7 ± 41.8 μm (G20).
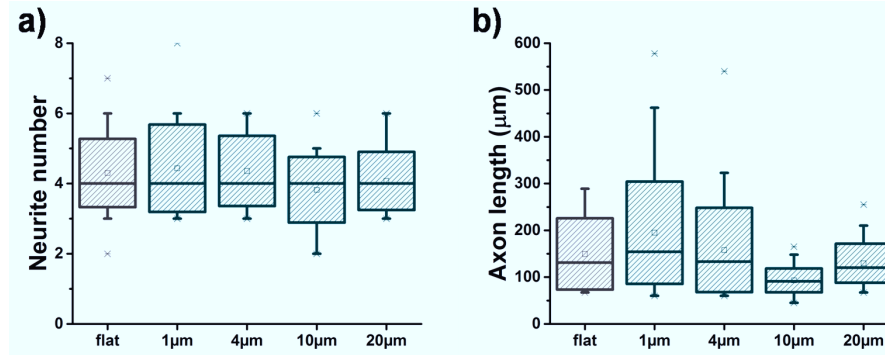
Figure 6.22. Quantification and data analyses of the different nanopillar interdistance of the gradient for a) neurite number and b) axon length. No significant differences in neurite number were observed between the surface topographies and the control. Axon length was increased on 1 μm and 4 μm interpillar distances in comparison to that on control substrates.

Throughout the process of axon outgrowth, the growth cones constantly protrude and retract while probing their surroundings. Previous reports explored the importance of biologically relevant scales when employing topographies, such as filopodium- or axon-sized silica beads.[39,211] While the filopodia are in the range of single nanostructures (250 nm), the growth cones, could dynamically expand to ~7 μm in width.[202,212] This could give an explanation as to why the axon alignment is not present when the interpillar distance reaches 10 μm. Only topographies with features smaller than the growth cone size encourage a continuous outgrowth along the nanostructures. Also, the total surface area (increased by the nanopillars distribution) could induce a correlation between the increase in directionality and axon elongation observed. The surface area of the nanostructured surface was calculated related to the lateral surface area of the pillars on x axis (2π·radius·height= 0.0785 μm², value corresponding for one pillar). In case of isotropic area (250 nm diameter, 250 nm interpillar distance, 100 nm height) the surface area increased by introduction of nanotopography by 31.4%, while for gradient patterns the following values were reached: 7.8% for G1, 4.5% for G4, 0.8% for G10, and 0.4% for the G20 gradient. It can be assumed that the increased surface area could significantly induce a different neuronal response. Higher values of the surface area (more signals for neurite outgrowth) showed an increase in orientation and axon length for the G1 pattern. 4 μm distance between the structures (G4 array) was found to still orient the neurite outgrowth, however less then G1 pattern. However, G10 and G20 patterns did not significantly influence axon orientation compared to the planar surface. This can be related to the lack of contacts points (topographical information) for neurite outgrowth. Signals from pillar sidewalls become insignificant on these arrays (<0.8% increase, G10 pattern) and neurons behave like on a planar surface.

6.2.1.1. Parylene nanosurface

In this subchapter, the neuronal alignment was investigated on parylene linear gradients fabricated from Si/SiO$_2$ molds. Parylene plays an important role in neuroscience since it is one of the most common polymers that have already been established in many clinical applications or in research and development as a material for neural implants.[16] The resulting parylene films containing flat and nanostructured surface arrays (1 x 1cm) were transferred in a reproducible manner onto a transparent substrate (glass slide covered with PDMS). The structures exhibited a lower pillar height (60 ± 9.6 nm) and a lower diameter (205 ± 13 nm) than the anticipated 100 nm and 250 nm, respectively. A reason for this could be the fact that the thin parylene film (13 µm) was not fully removed from the lower parts of the mold structures during transfer. SEM characterization of the parylene nanopillars is shown in Figure 6.23a. Planar and gradient-pattern parylene surfaces were compared regarding cell viability, adhesion, morphology, and polarity.
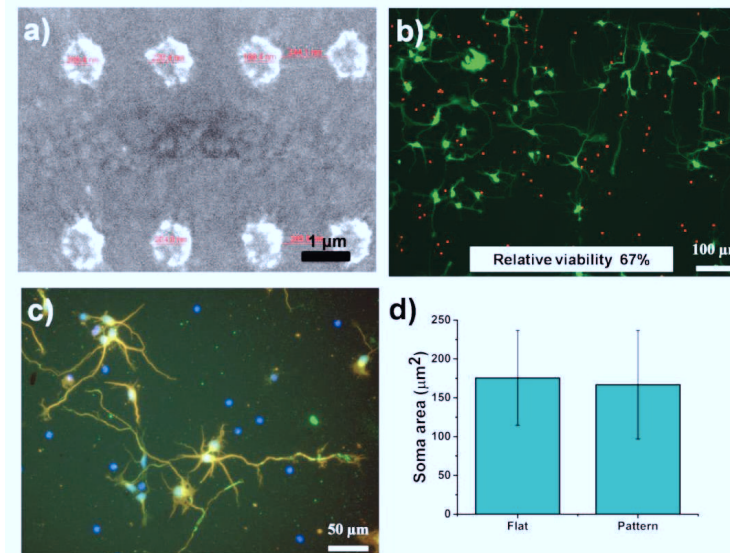
Figure 6.23. a) SEM image of the gradient-patterned surface depicting the nanopillars diameter. b) Representative images for live (green) and dead (red) staining neurons cultured on pattern parylene surface. Relative viability calculated after normalization with a control substrate showed that neurons survived in relatively high numbers. c) Fluorescent microscopy of neurons on gradient-patterned surfaces for specific axon development (green-NFH), cytoskeleton arrangement (orange-β3 tubulin), and nuclei (blue-DAPI). d) Contact area of the neuronal soma on flat and patterned parylene, n=40. Characterization of neural morphology shows a Stage 3 development and a strong adhesion comparable with control surfaces.

Figure 6.23 shows representative images of live/dead staining (Figure 6.23b) and immunostaining (DAPI-blue, NHF-green, β3 tubulin-orange, Figure 6.23c). Live/dead staining images reveal a relative viability of 67% (after normalization with a control sample, cell density 2 x 10⁴ cells/ml). Parylene supports cell growth with single neurons and partial network formation (Figure 6.23b). The cell/surface interface imaged by FIB cross sections reveals that only 39% of the cell membrane showed a conformal contact with flat parylene surfaces. The lower value of cell soma adhesion can relate to chemical characteristics of parylene compared with planar OrmoComp. In case of the parylene surface, cells form fewer adhesive contacts during neuronal culture. This can be related to the hydrophobicity of the surface. Since parylene has a lower contact angle than the Ormocomp surface, the PLL adsorption is higher. For nanostructured parylene the adhesion of the cell membrane on top and on the bottom of the nanostructures (bottom contact) reached 31%. A significant increase of membrane bending between the pillars was observed, 45% (Figure 6.24). The membrane fraction that bends between the nanopillars increased for parylene gradient pattern in comparison to OrmoComp substrate. This is a direct consequence not only of the chemical composition differences but also of the lower nanopillar height for parylene. Since the ratio of parylene topographical features (3.3 aspect ratio, width/height nanoholes) is increased compared to OrmoComp (AR=2.5) the membrane needs less energy to bend in the space between the pillars, Figure 6.24. The cell membrane exhibits a close adhesion with the polymer surface and bending between the nanopillars.
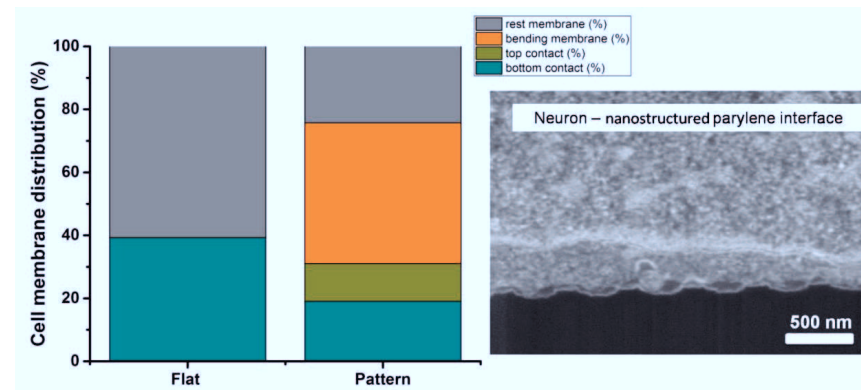
Figure 6.24. Neuronal soma membrane distribution at the cell-nanostructured parylene interface. Characterization of the cell membrane distribution for the flat and nanostructured parylene, where membrane percentage of conformal contacts is shown in blue (bottom) and green (top), bending membrane in orange, and membrane not in contact with surface in grey (left image). FIB-SEM cross section reveals the membrane attachment contacts and bending between the nanopillars (right image).

Besides cell adhesion, neurite development was also evaluated. Samples with flat and gradient-pattern surfaces were used to determine the influence of the polymer on neuritogenesis and polarity. As shown in Figure 6.23, the cells had healthy morphologies characteristic of Stage 3 of development, where the longest neurite breaks the symmetry and becomes the axon. The number of neurites was not significantly different for the two surfaces, Figure 6.25a. The neurons present comparable neurite numbers for all surfaces. Axonal outgrowth was found to be influenced by the pitch of the gradient (Figure 6.25b). A slight increase of axon length is observed for all arrays, compare with the flat surface (136 ± 68 μm). The most pronounced outgrowth was obtained for G1 (1 μm pitch) and G4 (4 μm pitch) arrays with a top value for G4 array: 158 ± 45 μm. This confirms the influence of topography on cell morphology. The trenches with small pitch distances could influence axon outgrowth have a guiding effect. These aspects are in concordance with results obtained for OrmoComp gradient surfaces.
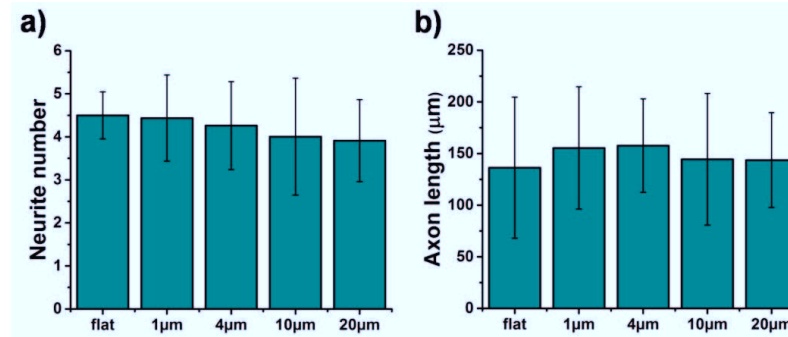
Figure 6.25. Characterization of neural development at 3 DIV regarding the number of neurites (a) and axon length (b).

The observed influences of parylene gradient-patterns were further studied regarding axonal alignment. SEM images of cells cultured on nanostructured parylene show well preserved cells with developed neurites and branching around the soma, Figure 6.26. It can be observed that the cell showed an increase number of neurites on the homogeneous area (diameter 250 nm, pitch 500 nm, Figure 6.26a) than on the gradient pattern (Figure 6.26b). Moreover, the array with a 1 μm pitch (G1) induced a polarization parallel to the direction of the trench and perpendicular to it.
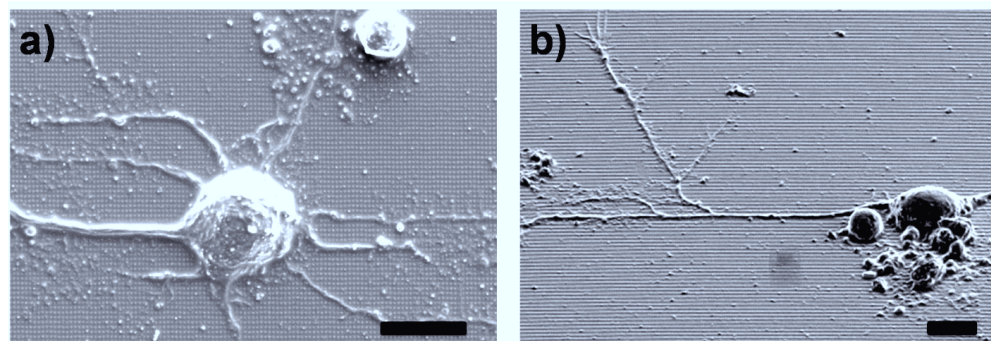
Figure 6.26. SEM images of neurons growing on parylene nanostructures. a) Cell body adhesion on an isotropic area (diameter 250 nm, pitch 500 nm). b) SEM image of a polarized neuron aligned to the topography (G1 array). Scale bars: 10 µm.

The axon alignment was quantified in order to observe the influence of the topography created by the different pitch of the trenches. Parallel direction of the axon was defined as the direction of the trench. The alignment was not so pronounced as in the case of OrmoComp substrates. Again the height difference played an important role. The two arrays with the smallest pitch distances (G1 and G4) had the highest values for alignment compared with G10 and G20. The arrays with a 4 µm pitch showed the highest alignment with 21% of parallel alignment and 15% in perpendicular direction. This correlates with the axon elongation observed for the same array, Figure 6.25b. The investigations of the axon alignment tended to show the same qualitative results as for OrmoComp surface. However, the directionality is less pronounced since the topographical impact diminished due to the smaller height (Figure 6.27).
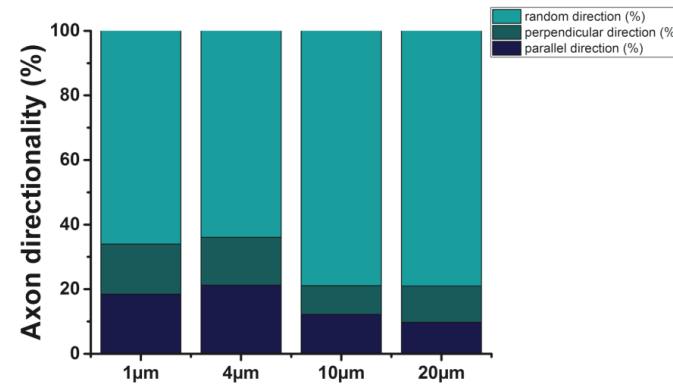
Figure 6.27. Axon directionality for the arrays with four different distances between the trenches. Axon outgrowth in the direction of the trench was defined as parallel, and perpendicular if it grew at a 90° angle relative to the direction of the trenches. Poor alignment can be observed for all sizes, but the trend of axon elongation in the direction of the trench is more pronounced for smaller trench distances.

6.2.2. Parylene nanostructured films deposited by oblique angle

In this subchapter, nanotextured parylene polymer (columnar-PPX) was employed to investigate the neuronal response to asymmetric surfaces characterized by dense, inclined polymer fibers. The columnar-PPX surface had a unidirectional orientation of nanotopographies. The columnar-PPX surface can exhibit both hydrophobic and water adhesive surface resulting in special wetting properties.[149,164] These wetting characteristics are described by a ratchet mechanism which includes water pinning and release functions. If the substrate is held 90° perpendicular to the ground, the pinning direction will hold a droplet at a critical volume whereas the same amount of water droplet will slide off in the release direction. This behavior also induced neuronal growth unidirectionality at low cell densities.[22] Neuronal cells cultured on the directional nano-PPX surface were directly affected by the biomechanical cues. Spedden et al. related the anisotropy in axonal outgrowth with the asymmetry in the growth cone-surface coupling caused by variations in the ratchet topography.[23] These experiments where performed at low cell densities, however, control of the cell growth and direction needs to be demonstrated also for higher cell densities in order to narrow the gap between *in vitro* studies and tissue in contact with implants. In this thesis, neuron development on asymmetric columnar-PPX surfaces was evaluated in regards to the: i) impact of the substrate topography on neuron maturation at higher cell densities in an early stage of neuronal development including viability, adhesion, and neuritogenesis analysis; ii) investigation of the actual interface between the neuron and 3D nanostructured PPX surface; iii) influence of the columnar-PPX surface on the initiation direction during axon formation.

6.2.2.1. Substrate characterization and modification

Planar and nanostructured PPX thin films were fabricated on glass and silicon substrates. The films had different morphologies due to the deposition system. Planar films were obtained in a normal configuration of the system. The thickness of the planar film was determined to be approximately 5 μm. For tilted films the deposition was carried out using a nozzle to disperse the entering monomer vapor on substrates. An assembly of tilted polymeric fibers with a length of 18-32 μm and a tilt angle of 53-61° was obtained for Si and glass substrate. Figure 6.28 shows the SEM and AFM characterization of the three surfaces. Top-view and cross-section SEM characterization of the columnar-PPX shows that the substrate can affect the final morphology of the polymeric film. The fibers on the Si surface had diameters in range of 50-100 nm, while being much wider (200-500 nm) on the glass substrate. In between these assemblies for both of the columnar surfaces, cracks and an irregular appearance could be observed (Figure 6.28d, g). Again, a difference was observed for the two substrates. Larger cracks and irregularities were found on glass substrates. The reason for the different film morphology can be related to the fact that the commercial glass substrates are normally 2 to 10 times rougher than Si wafers.[213] For a better understanding of the surface roughness the samples were analyzed by tapping-mode AFM. The calculated RMS roughness for planar-PPX was 2.7 ± 0.1 nm (Figure 6.28c). The columnar morphology, as expected, increased the surface roughness. Glass substrates exhibit a higher roughness (238.75 ± 29.1 nm, Figure 6.26f) compared to the Si substrate (151.6 ± 19.6 nm, Figure 6.28i). Using AFM images, the asymmetry parameter C_α (ratio of the rod angles facing the tilt direction and the rod angles facing the opposite direction of the tilt) was calculated. According to Spedden et al., the parameter C_α defines the asymmetry of the surface.[23] For columnar films deposited on both substrates the C_α parameter showed a quasi-similar asymmetry (C_α = 1.29 for Si substrate and C_α = 1.35 for columnar-PPX deposited on glass substrate). Another surface property induced by roughness was the surface wettability. Due to the periodic surface roughness the columnar-PPX exhibited hydrophobic properties with a contact angle of 110 ± 3°. Planar-PPX showed lower contact angles (88 ± 4°). All substrates were further modified using oxygen plasma and protein coating. After substrate modification the contact angles obtained were lower than 10°, indicating a hydrophilic surface.
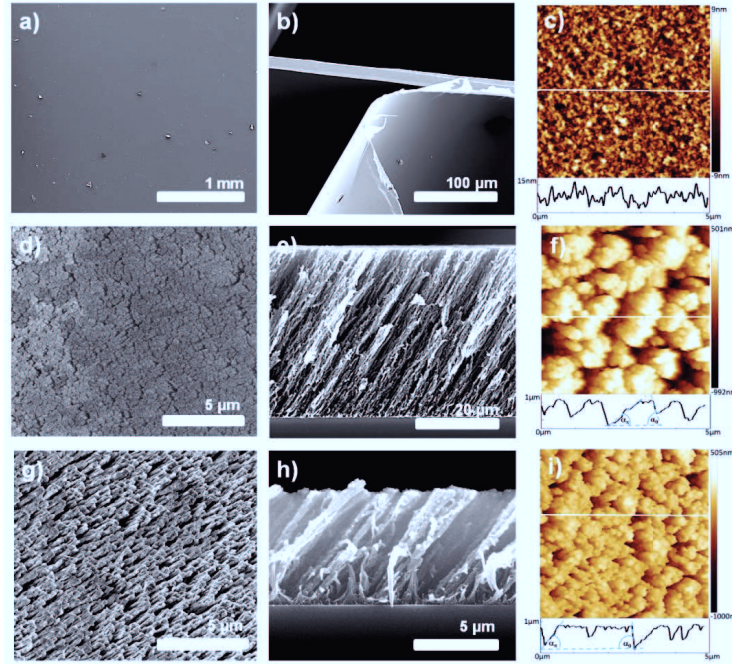
Figure 6.28. SEM and AFM characterization of PPX planar (a-c), columnar-PPX deposited on Si substrate (d-f), and columnar-PPX on glass substrate (g-i). AFM characterization was obtained by tapping mode-AFM. The white line indicates the position of the cross section shown at the bottom of each image. The cross-sections shows α_π and α_0, which were used to determine the asymmetry factor C_α.

6.2.2.2. Neuronal viability and development

After 3 or 4 DIV, a comprehensive analysis of viability, adhesion, neuritogenesis, and polarity was performed. The neuronal response on columnar-PPX was compared with the planar surface in order to observe the influence of the asymmetric surface on cell culture. Fluorescence microscopy was used to study the viability and development (Figure 6.29). Live/dead staining was used to determine cell viability. Representative images are shown in Figure 6.29a-c. Furthermore, the samples were investigated for specific cell components by immunostaining. Fluorescent microscopy of axon specific staining was done using Tau-1 antibodies, MAP2 for neurites, and DAPI for nuclei (Figure 6.29d-f). Figure 6.29 shows that PPX films support primary neuronal culture. Vital single neurons or neuronal networks are distributed over the entire area. The quantitative analysis of cell viability shown in Figure 6.29g reveals that planar-PPX surface had a higher viability compared to the two columnar surfaces. The viability was normalized to the control sample (cover slip with same PLL coating). The viability for control sample was taken as 100% and the viability determined

for all other substrates was recalculated relative to the control. Planar-PPX samples showed 75% viability, while cells on columnar-PPX showed a mean value of 50% for glass substrates, and 30% in case of Si substrates. Since the surface modification was identical for all substrates, the decrease in cell viability on columnar-PPX compared to the planar surface could be related to topographical cues. A similar trend can be observed for the soma area (Figure 6.29h). Large contact area of the soma indicating a strong and stable adhesion was found for planar-PPX in comparison to columnar-PPX surfaces. Cell responses caused by topography could be related to the way in which the cells contact the PLL on the surface. Furthermore, the influence of asymmetric surface topographies on neurite development was analyzed in detail. After 3 DIV, the neuronal maturation showed different stages on PPX surfaces. While neurons on control and columnar-PPX substrates showed a stage 3 development, those on planar-PPX were in Stage 2 (Figure 6.29d-f).
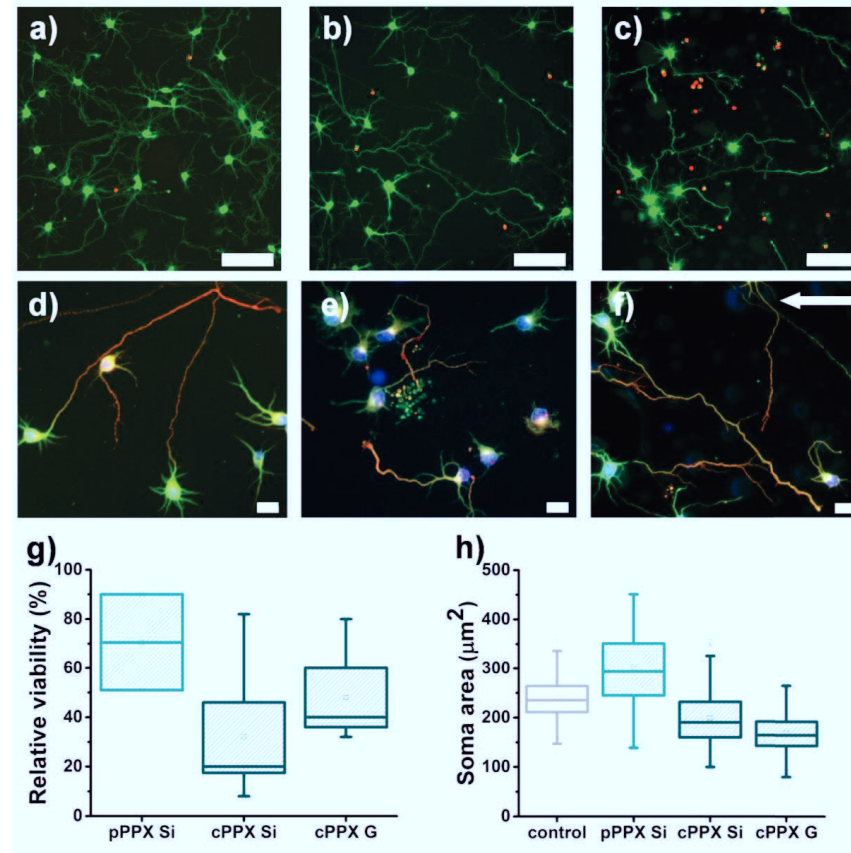
Figure 6.29. Representative fluorescence microscopy images after live/dead staining (a-c) and immunostaining (d-f). Live (green) and dead (red) primary neurons were imaged after 4 DIV for control (a), planar-PPX (b) and columnar-PPX (c) substrates. Scale bars a-c: 100 μm. Images after immunostaining for control (d), planar-PPX (e) and columnar-PPX (f) substrates after 3 DIV. Red (Tau1) color represents axons, whereas neurites (MAP2) are shown in green, and nuclei in blue (DAPI). Scale bars d-f: 20 μm. The white arrow indicates the direction of tilted nanofibers for columnar-PPX in c) and f) images. g) Viability of cultured neurons was calculated on planar-PPX (pPPX Si, n=98), columnar-PPX-Si (cPPX Si, n=138), and columnar-PPX-Glass (cPPX G, n=118), after normalization. h) Contact area of neural soma was analyzed from immunostaining images of the different PPX surfaces.

The neuritogenesis analysis showed a different behaviour of neurons on planar and columnar PPX films, Figure 6.30. Neurite number was found to decrease for all PPX surfaces (Figure 6.30a). This observation could be due to the chemical composition of the material. Neurons had a higher number of neurites on control substrates than for PPX samples, independent of their substrate. Comparing the axon length, neurons cultured on columnar

polymer surfaces had a similar mean value as control sample. Interestingly, neurons on planar-PPX surfaces had axons twice as short as those on columnar-PPX surfaces (Figure 6.30b). Since the polymer material and its topography did not only alter the formation of neurites, but also their outgrowth, these effects can be correlated. Due to the chemical composition of the material, the neurite development was inhibited, but the topographical aspect induced axonal elongation. Moreover, the axon branching was enhanced by the nanotextured surface as well. While control and planar-PPX samples showed no significant branching behavior the columnar samples exhibit enhanced branching (Figure 6.30c).
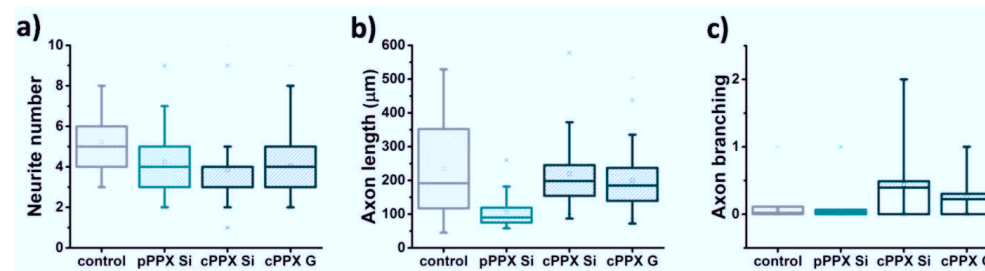
Figure 6.30. Statistical analysis of neural development at 3 DIV regarding number of neurites (a), axon length (b), and number of axon branches (c).

The SEM characterization of neurite interactions with planar and asymmetric PPX surfaces is shown in Figure 6.31. Exploration of the environment was studied due to the importance of filopodia extensions and growth cone sensing of their environment.[23,50,69,214,215] The shape of the growth cone was affected by the asymmetric surface. Typically, the growth cones showed a broad lateral extension.[216] The parylene material did not induce any change, since short and broad growth cone were observed on planar-PPX surface similar to planar control samples (Figure 6.31b). On the other hand, sprawled and slim growth cones were found on nanotextured surfaces, Figure 6.31a. This indicates that neurons sense many similar binding sites on the surface and the shape of the growth cone can be correlated with axon elongation. The investigation of the neurite processes revealed many small 20-50 nm projections reaching to the top polymer fibers, Figure 6.31c. These projections presumably contribute to the physical stability of neural processes.[217] When the polymer fibers bunch together they form assembles which are separated by gaps with varying widths. Mainly, the neurites adhere on the protruding top of the polymer fibers and overgrow gaps between fibers (Figure 6.31d-f). Small or micrometer large trenches can be crossed by neurites due to the tension created by the nanotextured surface. Moreover, these trenches can influence the pathfinding of axons and may interfere with the guiding effect of asymmetrical surface (see below).
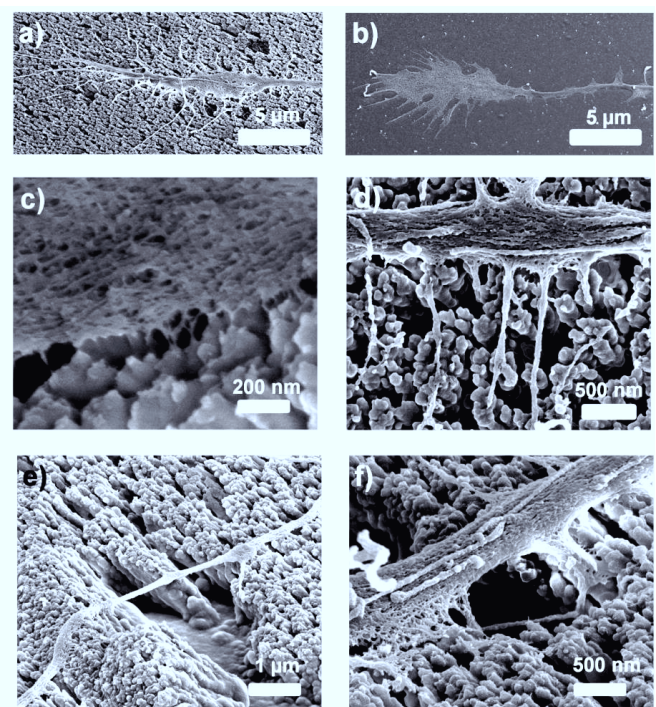
Figure 6.31. SEM micrographs of neurite interactions with planar and PPX asymmetric surfaces. a), b) Comparison of growth cone interaction with planar and columnar-PPX. The shape of the growth cone in the case of columnar-PPX is sprawled and slim (a), compared to much shorter and broader growth cones found on planar-PPX (b). c) Image of the cellular contact with the nanofibers at the filopodia level. Neurite interaction with the asymmetric surface on short distant depressions (d) and long distant depression (e, f). Increased neurite tension caused by the nanostructures might be responsible for overcoming long distances during growth. Micrographs were taken with 3 kV under 45° (a, b), 60° (c, e, f), and 0° tilt angle (d).

6.2.2.3. Adhesion and interface study

In addition, the cell-substrate interface was investigated at the nanometer scale after FIB-SEM cross-section (Figure 6.32). The cell-substrate interface can give an insight into the adhesion promoting properties of the respective material during neuron development.[141,218] Although no staining was performed, the cell-surface interface could be differentiated between the planar and columnar-PPX surface. On planar PPX surfaces, the soma had a flat and spread morphology that could be correlated with its large size shown above, Figure 6.32a. The cell membrane exhibited a conformal contact with the polymer, Figure 6.32b. In the case of columnar-PPX surfaces, the soma area showed a lower spread across the nanostructures (Figure 6.32c). A closer look at the interface obtained by FIB cross section

revealed that the cell membrane was mainly in contact with the top of the nanopillar. Only at some places, the cell membrane was able to adapt to the nanotextured surface and to grow projections into the space between the fibers (Figure 6.32d, f). This effect was also observed after double FIB cross section of the cell bodies, Figure 6.32e. For both columnar-PPX samples (Si and glass substrate) the cell membrane mainly gets in touch with the protruding apex of the polymer fibers due to the dense nanotextured surface. Also, although the pillars are tilted, there is no restriction to the cell membrane contact with the top created by anisotropy. As a mean value, the aspect ratio between the interpillar distance width and height was quantified as 1 (from AFM images, 500 nm width, 500 nm available height). The investigation on 100 nm OrmoComp arrays showed that 2.5 aspect ratio (nanoholes with 250 nm diameter, 100 nm height) was critical for membrane bending (7.8%) or adhesion contact with the surface between the pillars (1.7%). As expected, the lower aspect ratio induced by columnar-PPX surfaces decreased the membrane bending to 4% and contact with the interpillar surface to 0.8%. However, 60% of the total membrane length was found to be in contact with the top of the pillars.
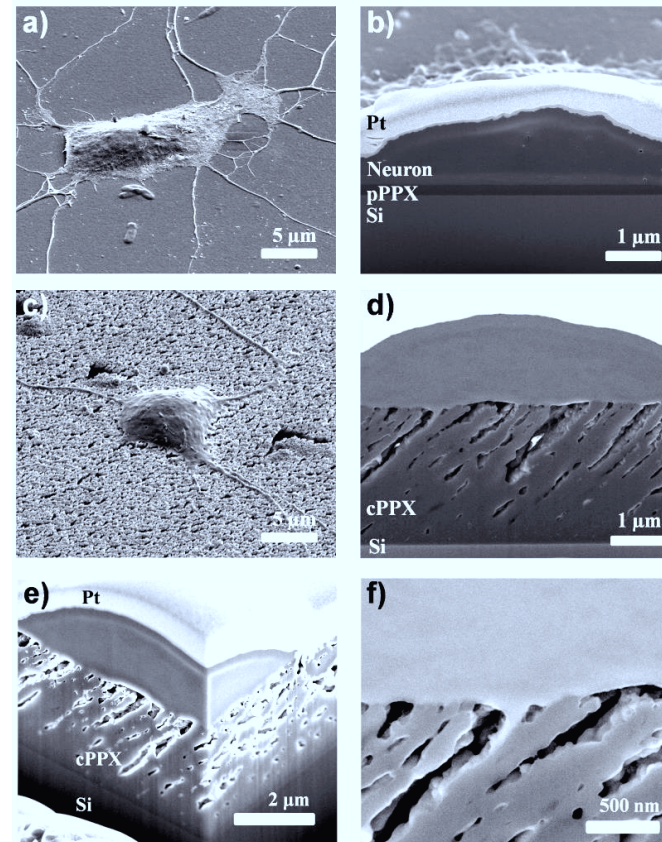
Figure 6.32. SEM and FIB cross-sections characterization of the neuronal soma interface with planar and columnar-PPX surfaces. a) Planar-PPX reveals a large soma size with b) conformal and continuous contact of the cell membrane. c) The cellular contact with the nanofibers showed a lower soma area. d) Cell-nanosurface interface showed conformal but non-continuous contact regions where the membrane bends into the interfilamental space. f) Zoom-in image of cell projections growing into the space between the fibers from d). e) Double cross-section of the cell body showing the cell-nanostructures contact in 2D.

6.2.2.4. Axon initiation and path finding angle

Due to the capability of the asymmetric surface to guide axon outgrowth direction at low cell densities, a point of interest was to observe the cell polarity at a higher density. Spedden et al. showed that the neurite alignment had a directional bias generated by the ratchet-like topography of the bunched PPX filaments (asymmetry parameter C_α). The neuronal directionality on the nanotextured surfaces, however, was achieved only at low densities of culture.[22,23] Beside the importance of a higher cell density to maintain high neuron

viability and long term culture, the guiding effect origin was also investigate. Until now, an open question was whether the guiding effect originates from oriented axon initiation or occurs during later axonal pathfinding. Figure 6.33a shows the schematics for determination of the axon angles. The initiation angle α (red color) was measured before the first change in axon direction, while the angle of the axon's distal end was measured as the path finding angle, β. Axons were considered aligned if the angle was 0° and if they were extended in the opposite direction of the nanofibers tilt angle.
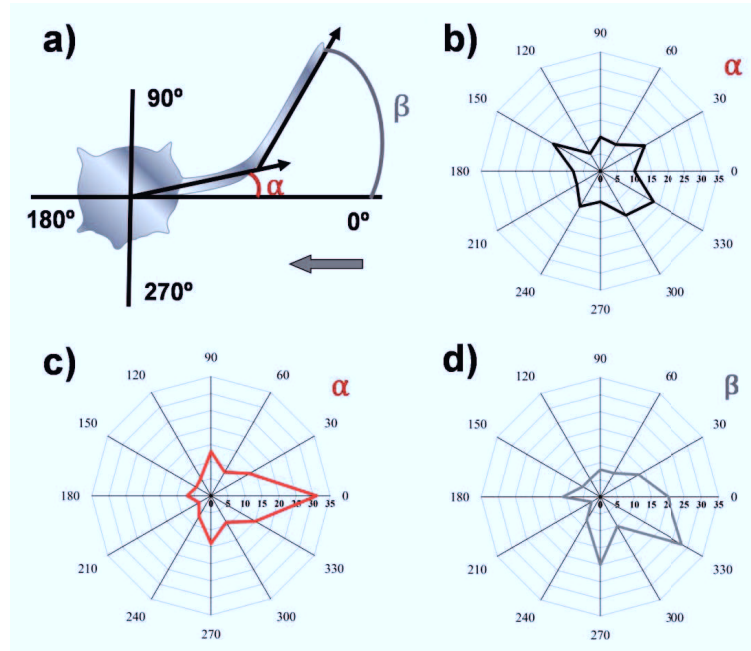
Figure 6.33. Guidance effect of high density neuronal cultures on planar and asymmetric surface. a) Schematic representation of the axon initiation angle (α, red color) and path finding angle (β, grey color). (b) Polar plots of the distribution of the initiation angles for control substrates showing a random distribution of axonal outgrowth. Polar plots of the distribution of initiation (c) and final path finding angles (d) on columnar-PPX. The asymmetric columnar-PPX surface strongly affects the axon initiation but this influence is attenuated in later stages of axonal outgrowth.

The asymmetric topographical cues induce a significant polarity of the axon, compared to the control substrate. Cell body shape and extending axon direction on control substrates and planar-PPX substrates exhibited no directional preference (Figure 6.33b). On the other hand, the asymmetric topographical cues induced less soma spreading and a directional axon elongation. Figure 6.33c shows that the axon initiation angles were regulated by the nanotextured surface opposite to the tilt direction of the nanopillars. This

indicates that neurites extending from the soma on the opposite tilt direction of nanopillars have a much higher probability to develop into axons than those initiated in the tilt direction. However, the directionality is less pronounced for the axon path finding angle (Figure 6.33d). Due to interfering of cell-cell signaling or surface topography (trenches/crack in the surface) the neuronal polarization is not maintained over long distances. These results indicate that the asymmetric nanotopography was capable of triggering axon polarization with a higher impact in the earlier stages of development but later, during path finding, the impact of topographical guiding cues diminished and interfering signaling randomized the axon elongation.

In the presented study, the influence of anisotropic surfaces on neuronal cultures on two different surface morphologies was investigated: i) linear gradients of nanostructures in OrmoComp and parylene and ii) tilted nanotextured parylene. The transition from isotropic to anisotropic surfaces was done by keeping the material, namely OrmoComp polymer. The anisotropic nanopillar array substrates were successfully used to induce axon polarization without any changes in the local chemical composition of the surface. Moreover, not only the guidance of axon was achieved but also elongation. 1 μm (x axis) and 250 nm (y axis) interpillar distances (G1 array) showed axon alignment with a mean value of 70% of the axons growing along or perpendicular to the trenches formed and a 25% increase in axon length compared to the flat surface. 4 μm distance between the structures (G4 array) was found to still orient neurite outgrowth (50%), however less robust then the G1 pattern. Neurite outgrowth alignment decreased drastically on 10 μm (G10) and 20 μm (G20) interpillar distances, due to less topographical cues available. Surface area increased <0.8% (due to lateral surface area of pillars) on the G10 array which did not affect neuronal development compared to the flat surfaces. These findings suggest that the orientation is dependent on the spacing between the trenches, which correlates with the total surface area. The molecular clutch model indicates that the cell-substrate contact points can induce the formation of focal adhesion complexes. These complexes induce a polymerization of F-actin as a mechanism of cell migration.[219–221] If the topographical information is subcritical then the cell can lose the alignment, as observed for interpillar distances larger than 10 μm. For smaller distances (1 and 4 μm), the anisotropic nanopillars affect the intracellular organization of cytoskeletal components and influence the axon length.

The impact of the linear gradient was also investigated for parylene polymer, commonly used as a material for implants. It is important to note that parylene showed a slightly harmful chemical effect. Cell viability, adhesion, neuritogenesis, and guidance are slightly lower compared to the OrmoComp polymer. Viability and cell body adhesion can be directly correlated with the chemical derogation while topography played an important role in cell development and guidance. Due to a different replication method of the materials, final dimensions of the structures did not have the same values for PPX and OrmoComp. Parylene replicas had a lower pillar height (60 nm) and smaller diameter (200 nm),

compared to the high fidelity replication of the OrmoComp material. The nanostructure height was especially relevant for axon guidance. The maximum guidance was reached on the G4 area with only 35% in parallel or perpendicular direction of the trenches. As a result, it appears that <1% increase in surface area of the G4 pattern did not impose sufficient topographical information for axonal guidance. These results correlate with OrmoComp's characteristic where 0.8% increase od surface area, introduced by nanostructures, did not affect neurite alignment (G10). However, the topographical parylene surface induced an improvement regarding cell-nanostructured interface. Due to the increased aspect ratio between the width of the interpillar distance and their height (3.3) compared to OrmoComp (2.5 aspect ratio, 250 nm width, 100 nm height) the cell membrane exhibits a close adhesion with the polymer surface. 45% of the cell membrane was bending in the space between the pillars on parylene nanostructured surface, while OrmoComp exhibited a lower value (7.8%).

The asymmetric parylene showed an interesting correlation between mechanical material properties and topography. PPX films with dense inclined polymer nanopillars supported primary neuronal culture but presented a lower viability than planar or gradient polymer surfaces. Beside the adhesion impairing properties, columnar-PPX showed axon and growth cone elongation as well as branching. For a better understanding of these results, surface topography and mechanical material compliance were addressed. First, the influence of nano-topography showed the same effect as in the case of isotropic surfaces, discussed in the subchapter above. The nano-topography showed a lower soma area. Tilted-nanopillars surface act as geometrical constraints restraining cell spreading. However, there is no restriction of the cell membrane contact with the top created by anisotropy. FIB cross-sections showed that 60% of the total membrane length was in contact with the top of the pillars. Due to the low aspect ratio (1, 500 nm interpillar distance width and 500 nm available height) cell bending or contact with the surface between the pillars was reduced (membrane bending 4%, contact with interpillar surface 0.8%), compared with OrmoComp surface (membrane bending 7.8%, contact with interpillar surface 1.7%). The second influence of topography was related to neurite elongation. Axon and growth cone elongation was more pronounced as in the case of gradient surface. Although, the asymmetric nanopillars taken separately correspond to the pillar diameter obtained for the gradients (200 nm), the asymmetry of the surface could prevent breaking of clutching of actin filaments, leading to advancing protrusions at the leading edge and neurite elongation.[50] Another reason for the increased neurite elongation could be related to the reduced stiffness of columnar-PPX compare to planar and gradient surfaces. In general, PPX can be considered as a relatively rigid polymer with a Young's modulus in the range from 2.5-3 GPa, depending on the deposition conditions.[17,222,223] However, high aspect ratio of nanopillars (diameter/height) decreases drastically the stiffness.

The Young's modulus was calculated for columnar-PPX (E_{eff}), in comparison with the bulk material (E_{bulk}):

$$E_{eff} = \frac{27}{16} E_{bulk} \left(\frac{r}{h}\right)^3,$$

where r represents the pillar radius, and h the pillar height.[51]

For 30 μm long nanopillars with radii of 50 nm and 220 nm, the E_{eff} decreases to 20 Pa and 2 kPa, respectively. These values are similar to the physiological stiffness of brain tissue. Here, the nanopillars had a 4 μm height, which leads to 8 kPa and 700 kPa for radii of 50 nm and 220 nm, respectively. The difference from planar bulk polymer stiffness is less pronounced, but possibly still sufficient to affect neuron development.[224] Softer substrates can stimulate mechanosignaling inducing neurite elongation and branching.[224–226] Softer surfaces can allow substrate displacement and thus lower traction forces. Lower adhesion forces conserve clutching of actin filaments linked on nanotopographies and induce neurite elongation as discussed above.[50] Furthermore, the nanotextured surface lead to axon elongation with a preferred directionality in early stages of neuron development. The asymmetric surface influenced the initiation angle of axon growing opposite to the tilt direction of the nanotexture. However, the directionality is less pronounced for the axon path finding angle due to the interfering of cell-cell signaling or surface topography. This indicates that neurites extending from the soma on the opposite tilt direction of nanopillars have a much higher probability to develop into axons than those initiated in any other direction. All these results imply the importance of interplay between biophysical cues (topography) and mechanical material properties in neuritogenesis, neurite outgrowth, and polarity.

7. CONCLUSIONS AND OUTLOOK

The aim of this thesis was to study the effect of 3D nano and microstructures fabricated from polymer materials on the primary neuronal cells viability, adhesion, and guidance. This thesis has demonstrated that physical cues of the OrmoComp and parylene polymer surfaces facilitate to control cell behavior for future improvement of implants surface.

The study included the fabrication of the 3D nano and microstructured isotropic substrates. Design variables such as height, diameter, and pitch size were used to produce reliable large area (1 x 1 cm) for cell culture exploration. It was demonstrated that nanoimprint lithography is a suitable technique for preparing inexpensive and reliable nanopatterned substrates. The dimensions and distances between the structures were ranging from 250 nm to 4 μm with 100 and 400 nm heights. The obtained polymer substrates were replicated from Si/SiO_2 molds with reasonable pattern fidelity for OrmoComp and parylene materials.

Prior to neuronal-surface study, a novel procedure for electron microscopy imaging was developed. In particular, an optimized cell fixation method was established in order to reduce cell preparation artifacts for electron microscopy characterization. The ultra-thin resin embedding method allows imaging the interface between neuron and 3D artificial surfaces for same specimen.[33] Fixation and staining improvement of the samples was achieved by a well defined path staining with OsO_4, tannic acid, and UrAc. Then, the samples were embedded in epoxy resin for cell's volume preservation. Before resin polymerization, the excess resin was removed at nanometer range. Well preserved morphology was obtained for single cells, cell-cell, and cell-3D surface interaction during SEM imaging. FIB-SEM characterization of the same possible specimen can disclose the information about the cell membrane conformation around the nanostructures. Moreover, this procedure can follow a fluorescence investigation of samples. The correlation of fluorescence microscopy with electron microscopy studies facilitates a comprehensive characterization of cell's topography, as well as high-resolution examination of the interface between cell and artificial 3D structures.

The cell response to alterations in surface topography was presented separately for isotropic and anisotropic surfaces. Two polymers were implemented: Ormocomp and parylene C. It was shown that not only the topography feature size, but also the properties of the bulk material showed an influence in cell response. For this reason, the results of neurons cultured on 3D substrates were compared with the cell behavior on planar polymers throughout this thesis. General morphological characteristics such as soma area, neurite number, axon length, turns, and alignment was conducted to investigate topographic effects on neuronal cells. Additionally, FIB-SEM microscopy was used to elucidate the actual adhesion at the cell-structures interface.

The study of isotropic OrmoComp surface included 10 arrays which aimed to influence the neuronal viability, development, and guidance. All OrmoComp polymer substrates supported neuronal growth and development without any significant detrimental effects on cell viability. The systematic investigation was used to identify which structures dimensions could influence neuronal morphological characteristics. An obvious behavior change was observed for cells cultures on arrays with 400 nm high pillars compare with the lower ones (100 nm). Higher pillars induce a significant axon elongation compare to flat and all the 100 nm high pillars arrays. The axon elongation was observed to be correlated to an increase number of axon branching and turns, but an inhibition of neurite number and cell body area. Moreover, the accelerated elongation on 400 nm pillars was accompanied by a preferential axon alignment according to the 3D surface. All structures present a good alignment and orthogonality orientation with a high fidelity on the pattern. Alignment and elongation incensement for the 400 nm pillars array can rely to the energetic balance between the filopodia adhesion and neurite bending. In case of 100 nm pillars the neurites showed to connect with the upper part of the pillars (top). That means that the neurite are suspended between the pillars top and only membrane protrusions interacts with the space between the pillars. For higher pillars the pull of the gravity onto the structures allow the neurites to increase the contact of with the flat surface between the pillars and pillars walls. Moreover, pillar walls act as local adhesion point to decrease the need of soma spreading and trigger the axon elongation. From all symmetric structures investigated pillars with 0.4 aspect ratio (height:diameter, A1 array, 400 nm height) showed the strongest axon elongation and alignment.

The interface characterization was performed to investigate the cell membrane deformation for 100 nm high structures for two different arrays types (aspect ratio defined as width/height of interpillar nanocavity/nanohole): arrays with pitch double the diameter: diameter pillars 250 nm (AR=2.5), 500 nm (AR=5), 750 nm (AR=7.5), 1 μm (AR=10), 2 μm (AR=20); arrays with 1 μm constant pitch: diameter pillars 250 nm (AR=7.5), 500 nm (AR=5), 750 nm (AR=2.5). The cell response was investigated considering the total membrane length and the surface area that the 3D structures can provide. A higher surface area can provide an increased value of cell-3D structure contact compared with the flat surface. However, the 20% increase of the surface area (compare with the flat surface) characteristic for pillars with AR=2.5 improve the cell-nanostructured surface contact. The membrane interacts in this case preferentially with the top of the pillars. Moreover, this observation was shown also for a 10% increase of the surface area (750 nm diameter, 1 μm pitch), but same AR (2.5). These results showed that the space between the pillars played a significant role since the membrane was observed to follow the curvature of the pillars and wrap them. Theoretical calculation was used to address this engulfment-like process in order to explore the wrapping effects and compare them to experimental results. Calculation of membrane deformation energy and adhesion energy lead to formation of different wrapping states similar with the experimental observations.

This thesis showed the possibility to successfully fabricate structures with a large range, nanometer to micrometer dimensions, with same parameters. The Si/SiO_2 molds were used to produce replicas of anisotropic 3D nanostructurd surfaces for OrmoComp and parylene polymers. The design consisted in a linear gradient with different slopes on *x* axis that reach a final distance of 1 μm, 4 μm, 10 μm, and 20 μm. The structures diameter and interpillar distance on *y* axis was design as 250 nm, constant for all arrays. Neurons cultured on the OrmoComp gradients showed an increase polarity induced exclusively by the surface topography. Small interpillar distances (1 and 4 μm) induced an axon alignment preference of 3.5 (number of aligned axons/number of nonaligned axons) along or perpendicular to the nanopillar lines. The preference decrease drastically for 10 and 20 μm, since the cells did not had enough topographical cues to react (<08% surface area increase compare to the flat surface). For 1 and 4 μm interpillar distances the signaling from closely spaced pillars may lead to a "domino" mechanism for growth stimulation, introduced by pillar contacts that maintain growth rate constant compared to the situation of more separated pillars, where signaling decay occurs.[227] Also for larger distances the growth cone is out of range to respond to geometrical cue.[219–221] To be noted that the height was defined as 100 nm and these results can be compared with the isotropic surface. Apparently the combination of the dimensions and their localization at certain discrete locations points induced a preferred distribution of the growth stimuli. In this regard, the obvious influence of the anisotropic surface created by nanopillar lines could generate an axonal guidance even at low 3D structures heights. Implementing the gradient design for parylene replica structures with lower height (60 nm) and lower diameter (200 nm) were obtained. In this case, the topographical information was not sufficient to induce a high axonal alignment. The maximum guidance was reached for 4 μm interpillars space area with 0.6 preference (number of aligned axons/number of nonaligned axons) in parallel or perpendicular direction of the trenches. Moreover, the parylene decrease the neuronal viability which can be directly correlated with the chemical derogation of the material.

The final surface used to explore the cell-3D nanostructures was represented by asymmetric PPX surface characterized by dense inclined polymer nanopillars (columnar-PPX). The columnar-PPX surface was showed to be inexpensive, easy-to-produce, with multi-functional surface. The production process does not require any clean room facilities or lithography technique.[21,150] The effect of columnar-PPX showed interesting correlation between mechanical material properties and topography on neuronal response. The asymmetry of the surface induced by the tilted nanopillars enhanced axons and growth cones elongation, as well as axon branching. However, the cell adhesion was impaired by the nanotextured surface inducing a lower viability than planar PPX film or parylene gradient replica. It is noteworthy that the 3D nano-texture of the polymer affects oppositely the neurogenises and adhesion. Furthermore, the axon elongation showed a preferred directionality in the earlier stages of neuron development. The initial angle can be

correlated with the probability that an axon can initiated with this 3D structure in the opposite tilt direction of nanopillars

A major advantage of the approach used in this thesis lies on the high reproducibility with which the substrates can be fabricated. The systematic variation of pillar design allowed to explore the changes in neuronal morphology that occurred as a consequence of pillar contact. Future applications lie on the impact in neuronal repair strategies of optimal topographical cues. Nanostructured arrays show great potential for chip electrode modification. An optimal contact at the interface might improve the complete signal transfer from the neuronal cell to the recording device. A relative quantification of the cell-surface contact with 250 nm diameter, 750 nm interpillar distance, and 100 nm height structures showed a 142% higher adhesion compare with the planar surface. Other open question could be related to the neuronal soma membrane deformation on 400 nm pillar height. In principle, it is necessary to investigate the complete cell body interaction. FIB-SEM sequential cutting of whole cells can provide the 3D reconstruction of the interface. The wrapping in 3D can show information about the higher aspect ratio structures on cell components modulation as nucleus in report with the surface. Also, the combination between the gradient property to increase axonal polarity for higher aspect ratio pillars could be of great interest. Array with higher alignments showed for isotropic surface (1 μm diameter, 2 μm pitch, 400 nm height) can be design and converted into gradient designs with short distances. It is expected that axons will shown a bidirectionality along the trenches. Increase axon directionality can be further investigated on columnar-PPX, too. Deformation of the columnar-PPX rods at different angles for higher asymmetry factor can be used to investigate the dominance of chemical or mechanical cues during neuronal development. Guided, elongated axons in a desired direction can offer therapeutic solution for the regeneration of damaged nerves.

8. REFERENCES

(1)   Donoghue, J. P. Connecting Cortex to Machines: Recent Advances in Brain Interfaces. *Nat. Neurosci.* **2002**, *5 Suppl*, 1085–1088.

(2)   Rivas, A.; Marlowe, A. L.; Chinnici, J. E.; Niparko, J. K.; Francis, H. W. Revision Cochlear Implantation Surgery in Adults. *Otol. Neurotol.* **2008**, *29*, 639–648.

(3)   Limousin, P.; Martinez-Torres, I. Deep Brain Stimulation for Parkinson's Disease. *Neurotherapeutics* **2008**, *5*, 309–319.

(4)   Winslow, B. D.; Tresco, P. A. Quantitative Analysis of the Tissue Response to Chronically Implanted Microwire Electrodes in Rat Cortex. *Biomaterials* **2010**, *31*, 1558–1567.

(5)   Santhanam, G.; Linderman, M. D.; Gilja, V.; Afshar, A.; Ryu, S. I.; Meng, T. H.; Shenoy, K. V. HermesB: A Continuous Neural Recording System for Freely Behaving Primates. *IEEE Transactions on Biomedical Engineering*, **2007**, *54*, 2037–2050.

(6)   http://www.cyberkinetics.com/.

(7)   Hoffman-Kim, D.; Mitchel, J. A.; Bellamkonda, R. V. Topography, Cell Response, and Nerve Regeneration. *Annu. Rev. Biomed. Eng.* **2010**, *12*, 203–231.

(8)   Kang, K.; Kim, M.-H.; Park, M.; Choi, I. S. Neurons on Nanotopographies: Behavioral Responses and Biological Implications. *J. Nanosci. Nanotechnol.* **2014**, *14*, 513–521.

(9)   Fattahi, P.; Yang, G.; Kim, G.; Abidian, M. R. A Review of Organic and Inorganic Biomaterials for Neural Interfaces. *Adv. Mater.* **2014**, *26*, 1846–1885.

(10)   Ovsianikov, A.; Chichkov, B.; Mente, P.; Monteiro-Riviere, N. A.; Doraiswamy, A.; Narayan, R. J. Two Photon Polymerization of Polymer Ceramic Hybrid Materials for Transdermal Drug Delivery. *Int. J. Appl. Ceram. Technol.* **2007**, *4*, 22–29.

(11)   Greiner, A. M.; Klein, F.; Gudzenko, T.; Richter, B.; Striebel, T.; Wundari, B. G.; Autenrieth, T. J.; Wegener, M.; Franz, C. M.; Bastmeyer, M. Cell Type-Specific Adaptation of Cellular and Nuclear Volume in Micro-Engineered 3D Environments. *Biomaterials* **2015**, *69*, 121–132.

(12)   Klein, F.; Richter, B.; Striebel, T.; Franz, C. M.; Freymann, G. Von; Wegener, M.; Bastmeyer, M. Two-Component Polymer Scaffolds for Controlled Three-Dimensional Cell Culture. *Adv. Mater.* **2011**, *23*, 1341–1345.

(13)   Klein, F.; Striebel, T.; Fischer, J.; Jiang, Z.; Franz, C. M.; Von Freymann, G.; Wegener, M.; Bastmeyer, M. Elastic Fully Three-Dimensional Microstructure Scaffolds for Cell Force Measurements. *Adv. Mater.* **2010**, *22*, 868–871.

(14)   Scheiwe, A. C.; Frank, S. C.; Autenrieth, T. J.; Bastmeyer, M.; Wegener, M. Subcellular Stretch-Induced Cytoskeletal Response of Single Fibroblasts within 3D Designer Scaffolds. *Biomaterials* **2015**, *44*, 186–194.

(15)   Weiss, T.; Hildebrand, G.; Schade, R.; Liefeith, K. Two-Photon Polymerization for Microfabrication of Three-Dimensional Scaffolds for Tissue Engineering Application. *Eng. Life Sci.* **2009**, *9*, 384–390.

(16)   Hassler, C.; Boretius, T.; Stieglitz, T. Polymers for Neural Implants. *J. Polym. Sci. Part B Polym. Phys.* **2011**, *49*, 18–33.

(17) Schmidt, E. M.; McIntosh, J. S.; Bak, M. J. Long-Term Implants of Parylene-C Coated Microelectrodes. *Med. Biol. Eng. Comput.* **1988**, *26*, 96–101.

(18) Fromherz, P.; Offenhäusser, A.; Vetter, T.; Weis, J. Junction : A Retzius Cell of the. *Science (80-.).* **1991**, *252*, 1290–1293.

(19) Cogan, S. F. Neural Stimulation and Recording Electrodes. *Annu. Rev. Biomed. Eng.* **2008**, *10*, 275–309.

(20) Hsu, J. M.; Rieth, L.; Normann, R. A.; Tathireddy, P.; Solzbacher, F. Encapsulation of an Integrated Neural Interface Device with Parylene C. *IEEE Trans. Biomed. Eng.* **2009**, *56*, 23–29.

(21) Demirel, M. C. Emergent Properties of Spatially Organized Poly(p-Xylylene) Films Fabricated by Vapor Deposition. *Colloids Surfaces A Physicochem. Eng. Asp.* **2008**, *321*, 121–124.

(22) Beighley, R.; Spedden, E.; Sekeroglu, K.; Atherton, T.; Demirel, M. C.; Staii, C. Neuronal Alignment on Asymmetric Textured Surfaces. *Appl. Phys. Lett.* **2012**, *101*.

(23) Spedden, E.; Wiens, M. R.; Demirel, M. C.; Staii, C. Effects of Surface Asymmetry on Neuronal Growth. *PLoS One* **2014**, *9*, e106709.

(24) Rothschild, R. M. Neuroengineering Tools/Applications for Bidirectional Interfaces, Brain–Computer Interfaces, and Neuroprosthetic Implants – A Review of Recent Progress. *Front. Neuroeng.* **2010**, *3*, 112.

(25) Axelrod, D. Total Internal Reflection Fluorescence Microscopy in Cell Biology. *Traffic* **2001**, *2*, 764–774.

(26) Toma, K.; Kano, H.; Offenhäusser, A. Label-Free Measurement of Cell–Electrode Cleft Gap Distance with High Spatial Resolution Surface Plasmon Microscopy. *ACS Nano* **2014**, *8*, 12612–12619.

(27) Friedmann, A.; Hoess, A.; Cismak, A.; Heilmann, A. Investigation of Cell-Substrate Interactions by Focused Ion Beam Preparation and Scanning Electron Microscopy. *Acta Biomater.* **2011**, *7*, 2499–2507.

(28) Wrobel, G.; Höller, M.; Ingebrandt, S.; Dieluweit, S.; Sommerhage, F.; Bochem, H. P.; Offenhäusser, A. Transmission Electron Microscopy Study of the Cell–sensor Interface. *J. R. Soc. Interface* **2008**, *5*, 213–222.

(29) Santoro, F.; Neumann, E.; Panaitov, G.; Offenhäusser, A. FIB Section of Cell–electrode Interface: An Approach for Reducing Curtaining Effects. *Microelectron. Eng.* **2014**, *124*, 17–21.

(30) Wierzbicki, R.; Købler, C.; Jensen, M. R. B.; Łopacińska, J.; Schmidt, M. S.; Skolimowski, M.; Abeille, F.; Qvortrup, K.; Mølhave, K. Mapping the Complex Morphology of Cell Interactions with Nanowire Substrates Using FIB-SEM. *PLoS One* **2013**, *8*, 1–12.

(31) Bushby, A. J.; P'ng, K. M. Y.; Young, R. D.; Pinali, C.; Knupp, C.; Quantock, A. J. Imaging Three-Dimensional Tissue Architectures by Focused Ion Beam Scanning Electron Microscopy. *Nat. Protoc.* **2011**, *6*, 845–858.

(32) Santoro, F.; Neumann, E.; Panaitov, G.; Offenhäusser, A. FIB Section of Cell-Electrode Interface: An Approach for Reducing Curtaining Effects. *Microelectron. Eng.* **2014**, *124*, 17–21.

(33) Belu, A.; Schnitker, J.; Bertazzo, S.; Neumann, E.; Mayer, D.; Offenhäusser, A.; Santoro, F. Ultra-Thin Resin Embedding Method for Scanning Electron Microscopy of Individual Cells on High and Low Aspect Ratio 3D Nanostructures. *J. Microsc.* **2016**,

263, 78–86.

(34) Reuveny, A.; Yokota, T.; Sekitani, T.; Someya, T. Ultra-Flexible Short-Channel Organic Field-Effect Transistors. **1882**, *91601*.

(35) Corey, J. M.; Lin, D. Y.; Mycek, K. B.; Chen, Q.; Samuel, S.; Feldman, E. L.; Martin, D. C. Aligned Electrospun Nanofibers Specify the Direction of Dorsal Root Ganglia Neurite Growth. *J. Biomed. Mater. Res. Part A* **2007**, *83A*, 636–645.

(36) Franze, K.; Guck. The Biophysics of Neuronal Growth. *Reports Prog. Phys.* **2010**, *73*, 94601.

(37) Nguyen, A. T.; Sathe, S. R.; Yim, E. K. F. From Nano to Micro: Topographical Scale and Its Impact on Cell Adhesion, Morphology and Contact Guidance. *J. Phys. Condens. Matter* **2016**, *28*, 183001.

(38) Kim, H. K.; Kim, E.; Jang, H.; Kim, Y.-K.; Kang, K. Neuron–Material Nanointerfaces: Surface Nanotopography Governs Neuronal Differentiation and Development. *ChemNanoMat* **2017**, *3*, 278–287.

(39) Kang, K.; Choi, S.-E. E.; Jang, H. S.; Cho, W. K.; Nam, Y.; Choi, I. S.; Lee, J. S. In Vitro Developmental Acceleration of Hippocampal Neurons on Nanostructures of Self-Assembled Silica Beads in Filopodium-Size Ranges. *Angew. Chemie - Int. Ed.* **2012**, *51*, 2855–2858.

(40) Bucaro, M. A.; Vasquez, Y.; Hatton, B. D.; Aizenberg, J. Fine-Tuning the Degree of Stem Cell Polarization and Alignment on Ordered Arrays of High-Aspect-Ratio Nanopillars. *ACS Nano* **2012**, *6*, 6222–6230.

(41) Toma, M.; Belu, A.; Mayer, D.; Offenhäusser, A. Flexible Gold Nanocone Array Surfaces as a Tool for Regulating Neuronal Behavior. *Small* **2017**, *13*, 1700629.

(42) Rajnicek, A.; Britland, S.; McCaig, C. Contact Guidance of CNS Neurites on Grooved Quartz: Influence of Groove Dimensions, Neuronal Age and Cell Type. *J. Cell Sci.* **1997**, *110 (Pt 2*, 2905–2913.

(43) Harrison, R. G. The Cultivation of Tissues in Extraneous Media as a Method of Morpho-Genetic Study. *Anat. Rec.* **1912**, *6*, 181–193.

(44) Yusoff, N. H.; Alshehadat, S. A.; Azlina, A.; Kannan, T. P.; Hamid, S. S. A. A Comparison of Culture Characteristics between Human Amniotic Mesenchymal Stem Cells and Dental Stem Cells. *Trop. Life Sci. Res.* **2015**, *26*, 21–29.

(45) Young, C. S.; Terada, S.; Vacanti, J. P.; Honda, M.; Bartlett, J. D.; Yelick, P. C. Tissue Engineering of Complex Tooth Structures on Biodegradable Polymer Scaffolds. *J. Dent. Res.* **2002**, *81*, 695–700.

(46) Loesberg, W. A.; te Riet, J.; van Delft, F. C. M. J. M.; Schon, P.; Figdor, C. G.; Speller, S.; van Loon, J. J. W. A.; Walboomers, X. F.; Jansen, J. A. The Threshold at Which Substrate Nanogroove Dimensions May Influence Fibroblast Alignment and Adhesion. *Biomaterials* **2007**, *28*, 3944–3951.

(47) Micholt, L.; Gärtner, A.; Prodanov, D.; Braeken, D.; Dotti, C. G.; Bartic, C. Substrate Topography Determines Neuronal Polarization and Growth In Vitro. *PLoS One* **2013**, *8*, 1–14.

(48) Xu, K.; Zhong, G.; Zhuang, X. Actin, Spectrin, and Associated Proteins Form a Periodic Cytoskeletal Structure in Axons. *Science* **2013**, *339*, 452–456.

(49) Roth, S.; Bisbal, M.; Brocard, J.; Bugnicourt, G.; Saoudi, Y.; Andrieux, A.; Gory-Faure, S.; Villard, C. How Morphological Constraints Affect Axonal Polarity in Mouse Neurons.

PLoS One **2012**, *7*, e33623.

(50) Kerstein, P. C.; Nichol Iv, R. H.; Gomez, T. M. Mechanochemical Regulation of Growth Cone Motility. *Front. Cell. Neurosci.* **2015**, *9*, 244.

(51) Bugnicourt, G.; Brocard, J.; Nicolas, A.; Villard, C. Nanoscale Surface Topography Reshapes Neuronal Growth in Culture. *Langmuir* **2014**, *30*, 4441–4449.

(52) Martini, F. *Fundamentals of Anatomy & Physiology*; Benjamin Cummings, **2004**.

(53) Thery, M.; Racine, V.; Piel, M.; Pepin, A.; Dimitrov, A.; Chen, Y.; Sibarita, J.-B.; Bornens, M. Anisotropy of Cell Adhesive Microenvironment Governs Cell Internal Organization and Orientation of Polarity. *Proc. Natl. Acad. Sci. U. S. A.* **2006**, *103*, 19771–19776.

(54) Bornens, M. The Centrosome in Cells and Organisms. *Science* **2012**, *335*, 422–426.

(55) Barnes, A. P.; Polleux, F. Establishment of Axon-Dendrite Polarity in Developing Neurons. *Annu. Rev. Neurosci.* **2009**, *32*, 347–381.

(56) Yu, W.; Baas, P. W. Changes in Microtubule Number and Length during Axon Differentiation. *J. Neurosci.* **1994**, *14*, 2818 LP-2829.

(57) Alberts, B.; Johnson, A.; Lewis, J.; Raff, M.; Roberts, K.; Walter, P. *Molecular Biology of the Cell, 5th Edition*; Garland Science, **2007**.

(58) Jones, J. C. R.; Goldman, A. E.; Steinert, P. M.; Yuspa, S.; Goldman, R. D. Dynamic Aspects of the Supramolecular Organization of Intermediate Filament Networks in Cultured Epidermal Cells. *Cell Motil.* **1982**, *2*, 197–213.

(59) Kirmse, R.; Qin, Z.; Weinert, C. M.; Hoenger, A.; Buehler, M. J.; Kreplak, L. Plasticity of Intermediate Filament Subunits. *PLoS One* **2010**, *5*, e12115.

(60) Menna, E.; Disanza, A.; Cagnoli, C.; Schenk, U.; Gelsomino, G.; Frittoli, E.; Hertzog, M.; Offenhauser, N.; Sawallisch, C.; Kreienkamp, H.-J.; *et al.* Eps8 Regulates Axonal Filopodia in Hippocampal Neurons in Response to Brain-Derived Neurotrophic Factor (BDNF). *PLoS Biol.* **2009**, *7*, e1000138.

(61) Balland, M.; Richert, A.; Gallet, F. The Dissipative Contribution of Myosin II in the Cytoskeleton Dynamics of Myoblasts. *Eur. Biophys. J.* **2005**, *34*, 255–261.

(62) Shemesh, T.; Bershadsky, A. D.; Kozlov, M. M. Physical Model for Self-Organization of Actin Cytoskeleton and Adhesion Complexes at the Cell Front. *Biophys. J.* **2012**, *102*, 1746–1756.

(63) Mogilner, A.; Oster, G. Cell Motility Driven by Actin Polymerization. *Biophys. J.* **1996**, *71*, 3030–3045.

(64) Gordon-Weeks, P. R. Microtubules and Growth Cone Function. *J. Neurobiol.* **2004**, *58*, 70–83.

(65) Gordon-Weeks, P. R. *Neuronal Growth Cones*; Cambridge University Press: Cambridge, **2000**.

(66) http://www.msunites.com/blog/2016/06/20/understanding-neurons/.

(67) Ramesh, V. Merlin and the ERM Proteins in Schwann Cells, Neurons and Growth Cones. *Nat Rev Neurosci* **2004**, *5*, 462–470.

(68) Leisman, G.; Moustafa, A. A.; Shafir, T. Thinking, Walking, Talking: Integratory Motor and Cognitive Brain Function. *Front. Public Heal.* **2016**, *4*, 94.

(69) Arimura, N.; Kaibuchi, K. Neuronal Polarity: From Extracellular Signals to Intracellular Mechanisms. *Nat. Rev. Neurosci.* **2007**, *8*, 194–205.

(70) Hynes, R. O. Integrins: Bidirectional, Allosteric Signaling Machines. *Cell* **2002**, *110*,

673–687.

(71) Goetz, J. G. Bidirectional Control of the Inner Dynamics of Focal Adhesions Promotes Cell Migration. *Cell Adh. Migr.* **2009**, *3*, 185–190.

(72) Alberts, B.; Johnson, A.; Lewis, J. *Molecular Biology of the Cell, 4th Edition*; Garland Science, 2002.

(73) Engler, A. J.; Sen, S.; Sweeney, H. L.; Discher, D. E. Matrix Elasticity Directs Stem Cell Lineage Specification. *Cell* **2006**, *126*, 677–689.

(74) Stopak, D.; Harris, A. K. Connective Tissue Morphogenesis by Fibroblast Traction. *Dev. Biol.* **1982**, *90*, 383–398.

(75) Leahy, D. J. Implications of Atomic-Resolution Structures for Cell Adhesion. *Annu. Rev. Cell Dev. Biol.* **1997**, *13*, 363–393.

(76) Kaech, S.; Banker, G. Culturing Hippocampal Neurons. *Nat. Protoc.* **2006**, *1*, 2406–2415.

(77) Lu, S.; Bansal, A.; Soussou, W.; Berger, T. W.; Madhukar, A. Receptor-Ligand-Based Specific Cell Adhesion on Solid Surfaces: Hippocampal Neuronal Cells on Bilinker Functionalized Glass. *Nano Lett.* **2006**, *6*, 1977–1981.

(78) Lee, M. H.; Brass, D. A.; Morris, R.; Composto, R. J.; Ducheyne, P. The Effect of Non-Specific Interactions on Cellular Adhesion Using Model Surfaces. *Biomaterials* **2005**, *26*, 1721–1730.

(79) Ballestrem, C.; Hinz, B.; Imhof, B. A.; Wehrle-Haller, B. Marching at the Front and Dragging behind: Differential alphaVbeta3-Integrin Turnover Regulates Focal Adhesion Behavior. *J. Cell Biol.* **2001**, *155*, 1319–1332.

(80) Rottner, K.; Hall, A.; Small, J. V. Interplay between Rac and Rho in the Control of Substrate Contact Dynamics. *Curr. Biol.* **1999**, *9*, 640–648.

(81) Riveline, D.; Zamir, E.; Balaban, N. Q.; Schwarz, U. S.; Ishizaki, T.; Narumiya, S.; Kam, Z.; Geiger, B.; Bershadsky, A. D. Focal Contacts as Mechanosensors: Externally Applied Local Mechanical Force Induces Growth of Focal Contacts by an mDia1-Dependent and ROCK-Independent Mechanism. *J. Cell Biol.* **2001**, *153*, 1175–1186.

(82) Clark, E. A.; King, W. G.; Brugge, J. S.; Symons, M.; Hynes, R. O. Integrin-Mediated Signals Regulated by Members of the Rho Family of GTPases. *J. Cell Biol.* **1998**, *142*, 573–586.

(83) Geiger, B.; Bershadsky, A.; Pankov, R.; Yamada, K. M. Transmembrane Crosstalk between the Extracellular Matrix--Cytoskeleton Crosstalk. *Nat. Rev. Mol. Cell Biol.* **2001**, *2*, 793–805.

(84) Goffin, J. M.; Pittet, P.; Csucs, G.; Lussi, J. W.; Meister, J.-J.; Hinz, B. Focal Adhesion Size Controls Tension-Dependent Recruitment of Alpha-Smooth Muscle Actin to Stress Fibers. *J. Cell Biol.* **2006**, *172*, 259–268.

(85) Tan, J. L.; Tien, J.; Pirone, D. M.; Gray, D. S.; Bhadriraju, K.; Chen, C. S. Cells Lying on a Bed of Microneedles: An Approach to Isolate Mechanical Force. *Proc. Natl. Acad. Sci. U. S. A.* **2003**, *100*, 1484–1489.

(86) Stricker, J.; Sabass, B.; Schwarz, U. S.; Gardel, M. L. Optimization of Traction Force Microscopy for Micron-Sized Focal Adhesions. *J. Phys. Condens. Matter* **2010**, *22*, 194104.

(87) http://www.reading.ac.uk/cellmigration/adhesion.htm.

(88) Geiger, B.; Spatz, J. P.; Bershadsky, A. D. Environmental Sensing through Focal Adhesions. *Nat. Rev. Mol. Cell Biol.* **2009**, *10*, 21–33.

(89) Folkman, J.; Moscona, A. Role of Cell Shape in Growth Control. *Nature* **1978**, *273*, 345–349.

(90) Perez-Garnes, M.; Barcia, J.; Gomez-Pinedo, U.; Monleon Pradas, M.; Valles-Lluch, A. Materials for Central Nervous System Tissue Engineering. In *Cells and Biomaterials in Regenerative Medicine*; **2014;** pp. 201–259.

(91) Yamada, K. M. Adhesive Recognition Sequences. *J. Biol. Chem.* **1991**, *266*, 12809–12812.

(92) Sagvolden, G.; Giaever, I.; Pettersen, E. O.; Feder, J. Cell Adhesion Force Microscopy. *Proc. Natl. Acad. Sci. U. S. A.* **1999**, *96*, 471–476.

(93) Branch, D. W.; Corey, J. M.; Weyhenmeyer, J. A.; Brewer, G. J.; Wheeler, B. C. Microstamp Patterns of Biomolecules for High-Resolution Neuronal Networks. *Med. Biol. Eng. Comput.* **1998**, *36*, 135–141.

(94) Wheeler, B. C.; Corey, J. M.; Brewer, G. J.; Branch, D. W. Microcontact Printing for Precise Control of Nerve Cell Growth in Culture. *J. Biomech. Eng.* **1999**, *121*, 73–78.

(95) Fricke, R.; Zentis, P. D.; Rajappa, L. T.; Hofmann, B.; Banzet, M.; Offenhäusser, A.; Meffert, S. H. Axon Guidance of Rat Cortical Neurons by Microcontact Printed Gradients. *Biomaterials* **2011**, *32*, 2070–2076.

(96) Hudalla, G. A.; Murphy, W. L. Chemically Well-Defined Self-Assembled Monolayers for Cell Culture: Toward Mimicking the Natural ECM. *Soft Matter* **2011**, *7*, 9561–9571.

(97) Norde, W. Adsorption of Proteins from Solution at the Solid-Liquid Interface. *Adv. Colloid Interface Sci.* **1986**, *25*, 267–340.

(98) Kleinfeld, D.; Kahler, K. H.; Hockberger, P. E. Controlled Outgrowth of Dissociated Neurons on Patterned Substrates. *J. Neurosci.* **1988**, *8*, 4098–4120.

(99) Corey, J. M.; Wheeler, B. C.; Brewer, G. J. Micrometer Resolution Silane-Based Patterning of Hippocampal Neurons: Critical Variables in Photoresist and Laser Ablation Processes for Substrate Fabrication. *IEEE Trans. Biomed. Eng.* **1996**, *43*, 944–955.

(100) Wyart, C.; Ybert, C.; Bourdieu, L.; Herr, C.; Prinz, C.; Chatenay, D. Constrained Synaptic Connectivity in Functional Mammalian Neuronal Networks Grown on Patterned Surfaces. *J. Neurosci. Methods* **2002**, *117*, 123–131.

(101) Gilles, S.; Winter, S.; Michael, K. E.; Meffert, S. H.; Li, P.; Greben, K.; Simon, U.; Offenh??usser, A.; Mayer, D. Control of Cell Adhesion and Neurite Outgrowth by Patterned Gold Nanoparticles with Tunable Attractive or Repulsive Surface Properties. *Small* **2012**, *8*, 3357–3367.

(102) Gefen, A.; Margulies, S. S. Are in Vivo and in Situ Brain Tissues Mechanically Similar? *J. Biomech.* **2004**, *37*, 1339–1352.

(103) Lu, Y.-B.; Iandiev, I.; Hollborn, M.; Korber, N.; Ulbricht, E.; Hirrlinger, P. G.; Pannicke, T.; Wei, E.-Q.; Bringmann, A.; Wolburg, H.; *et al.* Reactive Glial Cells: Increased Stiffness Correlates with Increased Intermediate Filament Expression. *FASEB J. Off. Publ. Fed. Am. Soc. Exp. Biol.* **2011**, *25*, 624–631.

(104) Horner, P. J.; Gage, F. H. Regenerating the Damaged Central Nervous System. *Nature* **2000**, *407*, 963–970.

(105) Suter, D. M.; Miller, K. E. The Emerging Role of Forces in Axonal Elongation. *Prog.*

Neurobiol. **2011**, *94*, 91–101.

(106) Franze, K. The Mechanical Control of Nervous System Development. *Development* **2013**, *140*, 3069–3077.

(107) Georges, P. C.; Janmey, P. A. Cell Type-Specific Response to Growth on Soft Materials. *J. Appl. Physiol.* **2005**, *98*, 1547–1553.

(108) Wong, J. Y.; Leach, J. B.; Brown, X. Q. Balance of Chemistry, Topography, and Mechanics at the Cell–biomaterial Interface: Issues and Challenges for Assessing the Role of Substrate Mechanics on Cell Response. *Surf. Sci.* **2004**, *570*, 119–133.

(109) Ma, P. X. Biomimetic Materials for Tissue Engineering. *Adv. Drug Deliv. Rev.* **2008**, *60*, 184–198.

(110) Rehfeldt, F.; Engler, A. J.; Eckhardt, A.; Ahmed, F.; Discher, D. E. Cell Responses to the Mechanochemical Microenvironment--Implications for Regenerative Medicine and Drug Delivery. *Adv. Drug Deliv. Rev.* **2007**, *59*, 1329–1339.

(111) Nemir, S.; West, J. L. Synthetic Materials in the Study of Cell Response to Substrate Rigidity. *Ann. Biomed. Eng.* **2010**, *38*, 2–20.

(112) Brown, X. Q.; Ookawa, K.; Wong, J. Y. Evaluation of Polydimethylsiloxane Scaffolds with Physiologically-Relevant Elastic Moduli: Interplay of Substrate Mechanics and Surface Chemistry Effects on Vascular Smooth Muscle Cell Response. *Biomaterials* **2005**, *26*, 3123–3129.

(113) Previtera, M. L.; Langhammer, C. G.; Firestein, B. L. Effects of Substrate Stiffness and Cell Density on Primary Hippocampal Cultures. *J. Biosci. Bioeng.* **2010**, *110*, 459–470.

(114) Flanagan, L. A.; Ju, Y.-E.; Marg, B.; Osterfield, M.; Janmey, P. a. Neurite Branching on Deformable Substrates. *Neuroreport* **2002**, *13*, 2411–2415.

(115) Betz, T.; Koch, D.; Lu, Y.-B.; Franze, K.; Käs, J. A. Growth Cones as Soft and Weak Force Generators. *Proc. Natl. Acad. Sci.* **2011**, *108*, 13420–13425.

(116) Georges, P. C.; Miller, W. J.; Meaney, D. F.; Sawyer, E. S.; Janmey, P. A. Matrices with Compliance Comparable to that of Brain Tissue Select Neuronal over Glial Growth in Mixed Cortical Cultures. *Biophys. J.* **2006**, *90*, 3012–3018.

(117) Fu, J.; Wang, Y.-K.; Yang, M. T.; Desai, R. A.; Yu, X.; Liu, Z.; Chen, C. S. Mechanical Regulation of Cell Function with Geometrically Modulated Elastomeric Substrates. *Nat Meth* **2010**, *7*, 733–736.

(118) Evans, N. D.; Gentleman, E. The Role of Material Structure and Mechanical Properties in Cell-Matrix Interactions. *J. Mater. Chem. B* **2014**, *2*, 2345–2356.

(119) http://me.engin.umich.edu/ibbl/research.html.

(120) Kim, M.-H.; Park, M.; Kang, K.; Choi, I. S. Neurons on Nanometric Topographies: Insights into Neuronal Behaviors in Vitro. *Biomater. Sci.* **2014**, *2*, 148–155.

(121) Chou, L.; Firth, J. D.; Uitto, V. J.; Brunette, D. M. Substratum Surface Topography Alters Cell Shape and Regulates Fibronectin mRNA Level, mRNA Stability, Secretion and Assembly in Human Fibroblasts. *J. Cell Sci.* **1995**, *108 (Pt 4*, 1563–1573.

(122) Karuri, N. W.; Liliensiek, S.; Teixeira, A. I.; Abrams, G.; Campbell, S.; Nealey, P. F.; Murphy, C. J. Biological Length Scale Topography Enhances Cell-Substratum Adhesion of Human Corneal Epithelial Cells. *J. Cell Sci.* **2004**, *117*, 3153–3164.

(123) Lim, J. Y.; Donahue, H. J. Cell Sensing and Response to Micro- and Nanostructured Surfaces Produced by Chemical and Topographic Patterning. *Tissue Eng.* **2007**, *13*,

1879–1891.

(124) Teixeira, A. I.; Abrams, G. A.; Bertics, P. J.; Murphy, C. J.; Nealey, P. F. Epithelial Contact Guidance on Well-Defined Micro- and Nanostructured Substrates. *J. Cell Sci.* **2003**, *116*, 1881–1892.

(125) den Braber, E. T.; de Ruijter, J. E.; Ginsel, L. A.; von Recum, A. F.; Jansen, J. A. Quantitative Analysis of Fibroblast Morphology on Microgrooved Surfaces with Various Groove and Ridge Dimensions. *Biomaterials* **1996**, *17*, 2037–2044.

(126) den Braber, E. T.; de Ruijter, J. E.; Ginsel, L. A.; von Recum, A. F.; Jansen, J. A. Orientation of ECM Protein Deposition, Fibroblast Cytoskeleton, and Attachment Complex Components on Silicone Microgrooved Surfaces. *J. Biomed. Mater. Res.* **1998**, *40*, 291–300.

(127) Meyle, J.; Gültig, K.; Brich, M.; Hämmerle, H.; Nisch, W. Contact Guidance of Fibroblasts on Biomaterial Surfaces. *J. Mater. Sci. Mater. Med.* **1994**, *5*, 463–466.

(128) Walboomers, X. F.; Croes, H. J.; Ginsel, L. A.; Jansen, J. A. Growth Behavior of Fibroblasts on Microgrooved Polystyrene. *Biomaterials* **1998**, *19*, 1861–1868.

(129) Roach, P.; Farrar, D.; Perry, C. C. Surface Tailoring for Controlled Protein Adsorption: Effect of Topography at the Nanometer Scale and Chemistry. *J. Am. Chem. Soc.* **2006**, *128*, 3939–3945.

(130) Siechen, S.; Yang, S.; Chiba, A.; Saif, T. Mechanical Tension Contributes to Clustering of Neurotransmitter Vesicles at Presynaptic Terminals. *Proc. Natl. Acad. Sci. U. S. A.* **2009**, *106*, 12611–12616.

(131) Kriparamanan, R.; Aswath, P.; Zhou, A.; Tang, L.; Nguyen, K. T. Nanotopography: Cellular Responses to Nanostructured Materials. *J. Nanosci. Nanotechnol.* **2006**, *6*, 1905–1919.

(132) Fan, Y. W.; Cui, F. Z.; Hou, S. P.; Xu, Q. Y.; Chen, L. N.; Lee, I.-S. I.-S. S. Culture of Neural Cells on Silicon Wafers with Nano-Scale Surface Topology. *J. Neurosci. Meth.* **2002**, *120*, 17–23.

(133) Khan, S. P.; Auner, G. G.; Newaz, G. M. Influence of Nanoscale Surface Roughness on Neural Cell Attachment on Silicon. *Nanomedicine Nanotechnology, Biol. Med.* **2005**, *1*, 125–129.

(134) Brunetti, V.; Maiorano, G.; Rizzello, L.; Sorce, B.; Sabella, S.; Cingolani, R.; Pompa, P. P. Neurons Sense Nanoscale Roughness with Nanometer Sensitivity. *Proc. Natl. Acad. Sci. U. S. A.* **2010**, *107*, 6264–6269.

(135) Kim, I.; Kim, S.-E.; Han, S.; Kim, H.; Lee, J.; Jeong, D.-W.; Kim, J.-J.; Lim, Y.; Choi, H.-J. Large Current Difference in Au-Coated Vertical Silicon Nanowire Electrode Array with Functionalization of Peptides. *Nanoscale Res. Lett.* **2013**, *8*, 502.

(136) Hallstrom, W.; Martensson, T.; Prinz, C.; Gustavsson, P.; Montelius, L.; Samuelson, L.; Kanje, M. Gallium Phosphide Nanowires as a Substrate for Cultured Neurons. *Nano Lett.* **2007**, *7*, 2960–2965.

(137) Shalek, A. K.; Robinson, J. T.; Karp, E. S.; Lee, J. S.; Ahn, D.-R.; Yoon, M.-H.; Sutton, A.; Jorgolli, M.; Gertner, R. S.; Gujral, T. S.; *et al.* Vertical Silicon Nanowires as a Universal Platform for Delivering Biomolecules into Living Cells. *Proc. Natl. Acad. Sci. U. S. A.* **2010**, *107*, 1870–1875.

(138) Prinz, C.; Hallstrom, W.; Martensson, T.; Samuelson, L.; Montelius, L.; Kanje, M. Axonal Guidance on Patterned Free-Standing Nanowire Surfaces. *Nanotechnology* **2008**, *19*,

345101.

(139) Cho, W. K.; Kang, K.; Kang, G.; Jang, M. J.; Nam, Y.; Choi, I. S. Pitch-Dependent Acceleration of Neurite Outgrowth on Nanostructured Anodized Aluminum Oxide Substrates. *Angew. Chem. Int. Ed. Engl.* **2010**, *49*, 10114–10118.

(140) Hai, A.; Shappir, J.; Spira, M. E. In-Cell Recordings by Extracellular Microelectrodes. *Nat. Methods* **2010**, *7*, 200–202.

(141) Kundu, P.; Belu, A.; Neumann, E.; Mayer, D.; Offenhäusser, A. 3D Au–SiO 2 Nanohybrids as a Potential Scaffold Coating Material for Neuroengineering. *RSC Adv.* **2016**, *6*, 47948–47952.

(142) Kuppusami, S.; Oskouei, R. H. Parylene Coatings in Medical Devices and Implants : A Review. *Univers. J. Biomed. Eng.* **2015**, *3*, 9–14.

(143) Tan, C. P.; Craighead, H. G. Surface Engineering and Patterning Using Parylene for Biological Applications. *Materials (Basel).* **2010**, *3*, 1803–1832.

(144) Rodger, D. C.; Fong, A. J.; Li, W.; Ameri, H.; Ahuja, A. K.; Gutierrez, C.; Lavrov, I.; Zhong, H.; Menon, P. R.; Meng, E.; *et al.* Flexible Parylene-Based Multielectrode Array Technology for High-Density Neural Stimulation and Recording. *Sensors Actuators, B Chem.* **2008**, *132*, 449–460.

(145) Cieślik, M.; Engvall, K.; Pan, J.; Kotarba, A. Silane-Parylene Coating for Improving Corrosion Resistance of Stainless Steel 316L Implant Material. *Corros. Sci.* **2011**, *53*, 296–301.

(146) Cieślik, M.; Zimowski, S.; Gołda, M.; Engvall, K.; Pan, J.; Rakowski, W.; Kotarba, A. Engineering of Bone Fixation Metal Implants Biointerface - Application of Parylene C as Versatile Protective Coating. *Mater. Sci. Eng. C* **2012**, *32*, 2431–2435.

(147) Grinberg, O.; Natan, M.; Lipovsky, A.; Varvak, A.; Keppner, H.; Gedanken, A.; Banin, E. Antibiotic Nanoparticles Embedded into the Parylene C Layer as a New Method to Prevent Medical Device-Associated Infections. *J. Mater. Chem. B* **2015**, *3*, 59–64.

(148) Chindam, C.; Wonderling, N. M.; Lakhtakia, A.; Awadelkarim, O. O.; Orfali, W. Microfiber Inclination, Crystallinity, and Water Wettability of Microfibrous Thin-Film Substrates of Parylene C in Relation to the Direction of the Monomer Vapor during Fabrication. *Appl. Surf. Sci.* **2015**, *345*, 145–155.

(149) Boduroglu, S.; Cetinkaya, M.; Dressick, W. J.; Singh, A.; Demirel, M. C. Controlling the Wettability and Adhesion of Nanostructured Poly-(P-Xylylene) Films. *Langmuir* **2007**, *23*, 11391–11395.

(150) Malvadkar, N. A.; Hancock, M. J.; Sekeroglu, K.; Dressick, W. J.; Demirel, M. C. An Engineered Anisotropic Nanofilm with Unidirectional Wetting Properties. *Nat. Mater.* **2010**, *9*, 1023–1028.

(151) Stout, K. J.; Blunt, L. *Three Dimensional Surface Topography*; Elsevier, 2000.

(152) Jandt, K. D. Atomic Force Microscopy of Biomaterials Surfaces and Interfaces. *Surf. Sci.* **2001**, *491*, 303–332.

(153) Bracco, G.; Holst, B. *Surface Science Techniques*; 2013; Vol. 51.

(154) Wenzel, R. N. RESISTANCE OF SOLID SURFACES TO WETTING BY WATER. *Ind. Eng. Chem.* **1936**, *28*, 988–994.

(155) Cassie, A. B. D.; Baxter, S. Wettability of Porous Surfaces. *Trans. Faraday Soc.* **1944**, *40*, 546–551.

(156) Goldstein, J.; Lyman, C.; Newbury, D.; Lifshin, E.; Echlin, P.; Sawyer, L.; Joy, D.; Michael, J. R. *Scanning Electron Microscopy and X-Ray Microanalysis, 3rd Edition*; Springer, **2004**.

(157) Lichtman, J. W.; Conchello, J.-A. Fluorescence Microscopy. *Nat. Methods* **2005**, *2*, 910–919.

(158) https://www.zeiss.com/microscopy/int/products/imaging-systems/apotome-2-for-biology.html.

(159) Madou, M. J. *Fundamentals of Microfabrication: The Science of Miniaturization, 2nd Edition*; CRC Press, **2002**.

(160) Xia, Y.; Whitesides, G. M. Soft Lithography. *Angew. Chemie Int. Ed.* **1998**, *37*, 550–575.

(161) Demirel, G.; Malvadkar, N.; Demirel, M. C. Template-Based and Template-Free Preparation of Nanostructured Parylene via Oblique Angle Polymerization. *Thin Solid Films* **2010**, *518*, 4252–4255.

(162) Demirel, G.; Babur, E. Vapor-Phase Deposition of Polymers as a Simple and Versatile Technique to Generate Paper-Based Microfluidic Platforms for Bioassay Applications. *Analyst* **2014**, *139*, 2326–2331.

(163) Cetinkaya, M.; Demirel, M. C. Bridging Experiments and Simulations in Oblique Angle Polymerization. *Chem. Vap. Depos.* **2009**, *15*, 101–105.

(164) Cetinkaya, M.; Boduroglu, S.; Demirel, M. C. Growth of Nanostructured Thin Films of Poly(p-Xylylene) Derivatives by Vapor Deposition. *Polymer (Guildf).* **2007**, *48*, 4130–4134.

(165) Petersen, K.; Pedersen, H. C. Detection Methods. *Educ. IO NA L Immunohistochem. Stain. Methods* **2013**, 78–93.

(166) Tarnowski, B. I.; Spinale, F. G.; Nicholson, J. H. DAPI as a Useful Stain for Nuclear Quantitation. *Biotech. Histochem.* **1991**, *66*, 297–302.

(167) Thavarajah, R.; Mudimbaimannar, V. K.; Elizabeth, J.; Rao, U. K.; Ranganathan, K. Chemical and Physical Basics of Routine Formaldehyde Fixation. *Journal of Oral and Maxillofacial Pathology : JOMFP*, **2012**, *16*, 400–405.

(168) Ackermann, J.; Juda, M.; Hirsch, D. Polymethyl Methacrylate (PMMA). *Kunststoffe Int.* **2014**, *2014*, 59–64.

(169) Saffih, F.; Con, C.; Alshammari, A.; Yavuz, M.; Cui, B.; Saffih, F. Fabrication of Silicon Nanostructures with Large Taper Angle by Reactive Ion Etching Fabrication of Silicon Nanostructures with Large Taper Angle by Reactive Ion Etching. **2014**, *4*, 4–8.

(170) Choi, S.; Hong, S. J. Use of Hard Mask for Finer (< 10 μ M) Through Silicon Vias (TSVs) Etching. **2015**, *16*, 312–316.

(171) DeRose, G.; Shearn, M.; Henry, D.; Chen, Y.; Scherer, A. Deep RIE and Cryo-Etching of Nanostructures in Silicon and Polymers. *Microsc. Microanal.* **2008**, *14*, 432–433.

(172) Helmut Schmidt. Processing and Optical Properties of Inorganic-Organic Composites. *Chemical Processing of Advanced Materials*, **1992**, 727–735.

(173) MicroResist. Ormocomp. *Forschung* 65762192–65762192.

(174) Popall, M.; Dabek, A.; Robertsson, M. E.; Valizadeh, S.; Hagel, O. J.; Buestrich, R.; Nagel, R.; Cergel, L.; Lambert, D.; Schaub, M. ORMOCER®S – Inorganic-Organic Hybrid Materials for E/o-Interconnection-Technology. *Mol. Cryst. Liq. Cryst. Sci. Technol. Sect. A. Mol. Cryst. Liq. Cryst.* **2000**, *354*, 123–142.

(175) Schizas, C.; Karalekas, D. Mechanical Characteristics of an Ormocomp Biocompatible Hybrid Photopolymer. *J. Mech. Behav. Biomed. Mater.* **2011**, *4*, 99–106.

(176) Lan, H. Soft UV Nanoimprint Lithography and Its Applications. *Intechopen* **2013**, 169–195.

(177) Voigt, A.; Engelke, R.; Ahrens, G.; Bullerjahn, F.; Schleunitz, A.; Klein, J. J.; Gruetzner, G. Removal of Highly Crosslinked Resists and Hybrid Polymers for Single Micro Parts Fabrication and Nanoimprint Stamp Rework. **2014**, *9051*, 90511H–90511H–10.

(178) Alivisatos, A. P.; Andrews, A. M.; Boyden, E. S.; Chun, M.; Church, G. M.; Deisseroth, K.; Donoghue, J. P.; Fraser, S. E.; Lippincott-Schwartz, J.; Looger, L. L.; *et al.* Nanotools for Neuroscience and Brain Activity Mapping. *ACS Nano* **2013**, *7*, 1850–1866.

(179) Conner, S. D.; Schmid, S. L. Regulated Portals of Entry into the Cell. *Nature* **2003**, *422*, 37–44.

(180) Spira, M. E.; Kamber, D.; Dormann, A.; Cohen, A.; Bartic, C.; Borghs, G.; Langedijk, J. P. M.; Yitzchaik, S.; Shabthai, K.; Shappir, J. Improved Neuronal Adhesion to the Surface of Electronic Device by Engulfment of Protruding Micro-Nails Fabricated on the Chip Surface. In *Solid-State Sensors, Actuators and Microsystems Conference, 2007. TRANSDUCERS 2007. International*; **2007**; pp. 1247–1250.

(181) Hanson, L.; Lin, Z. C.; Xie, C.; Cui, Y.; Cui, B. Characterization of the Cell-Nanopillar Interface by Transmission Electron Microscopy. *Nano Lett.* **2012**, *12*, 5815–5820.

(182) Santoro, F.; Dasgupta, S.; Schnitker, J.; Auth, T.; Neumann, E.; Panaitov, G.; Gompper, G.; Offenhäusser, A. Interfacing Electrogenic Cells with 3D Nanoelectrodes: Position, Shape, and Size Matter. *ACS Nano* **2014**, *8*, 6713–6723.

(183) Drobne, D. 3D Imaging of Cells and Tissues by Focused Ion Beam/Scanning Electron Microscopy (FIB/SEM). In *Nanoimaging*; Sousa, A. A.; Kruhlak, M. J., Eds.; Methods in Molecular Biology; Humana Press, **2013**; pp. 275–292.

(184) Friedmann, A.; Cismak, A.; Tautorat, C.; Koester, P. J.; Baumann, W.; Held, J.; Gaspar, J.; Ruther, P.; Paul, O.; Heilmann, A. FIB Preparation and SEM Investigations for Three-Dimensional Analysis of Cell Cultures on Microneedle Arrays. *Scanning* **2012**, *34*, 221–229.

(185) Lešer, V.; Drobne, D.; Pipan, Ž.; Milani, M.; Tatti, F. Comparison of Different Preparation Methods of Biological Samples for FIB Milling and SEM Investigation. *J. Microsc.* **2009**, *233*, 309–319.

(186) Hayat, M. A. *Principle and Techniques of Electron Microscoly, Biological Application, 4th Edition*; Cambridge University Press, **2000**.

(187) McCarthy, D. A.; Pell, B. K.; Holburn, C. M.; Moore, S. R.; Perry, J. D.; Goddard, D. H.; Kirk, A. P. A Tannic Acid Based Preparation Procedure Which Enables Leucocytes to Be Examined Subsequently by Either SEM or TEM. *J. Microsc.* **1985**, *137*, 57–64.

(188) Bertazzo, S.; Gentleman, E.; Cloyd, K. L.; Chester, A. H.; Yacoub, M. H.; Stevens, M. M. Nano-Analytical Electron Microscopy Reveals Fundamental Insights into Human Cardiovascular Tissue Calcification. *Nat. Mater.* **2013**, *12*, 576–583.

(189) Gusnard, D.; Kirschner, R. H. Cell and Organelle Shrinkage during Preparation for Scanning Electron Microscopy: Effects of Fixation, Dehydration and Critical Point Drying. *J. Microsc.* **1977**, *110*, 51–57.

(190) Kim, S.; Qiu, F.; Kim, S.; Ghanbari, A.; Moon, C.; Zhang, L.; Nelson, B. J.; Choi, H. Fabrication and Characterization of Magnetic Microrobots for Three-Dimensional Cell

Culture and Targeted Transportation. *Adv. Mater.* **2013**, *25*, 5863–5868.

(191) Greiner, A. M.; Jäckel, M.; Scheiwe, A. C.; Stamow, D. R.; Autenrieth, T. J.; Lahann, J.; Franz, C. M.; Bastmeyer, M. Multifunctional Polymer Scaffolds with Adjustable Pore Size Andchemoattractant Gradients for Studying Cell Matrix Invasion. *Biomaterials* **2014**, *35*, 611–619.

(192) Bonde, S.; Buch-Manson, N.; Rostgaard, K. R.; Andersen, T. K.; Berthing, T.; Martinez, K. L. Exploring Arrays of Vertical One-Dimensional Nanostructures for Cellular Investigations. *Nanotechnology* **2014**, *25*, 362001.

(193) Roach, P.; Parker, T.; Gadegaard, N.; Alexander, M. R. Surface Strategies for Control of Neuronal Cell Adhesion: A Review. *Surf. Sci. Rep.* **2010**, *65*, 145–173.

(194) Lim, J. Y.; Donahue, H. J. Cell Sensing and Response to Micro- and Nanostructured Surfaces Produced by Chemical and Topographic Patterning. *Tissue Eng.* **2007**, *13*, 1879–1891.

(195) Stiles, J.; Jernigan, T. L. The Basics of Brain Development. *Neuropsychol. Rev.* **2010**, *20*, 327–348.

(196) Czeschik, A.; Offenhäusser, A.; Wolfrum, B. Fabrication of MEA-Based Nanocavity Sensor Arrays for Extracellular Recording of Action Potentials. *Phys. status solidi* **2014**, *211*, 1462–1466.

(197) Czeschik, A.; Rinklin, P.; Derra, U.; Ullmann, S.; Holik, P.; Steltenkamp, S.; Offenhäusser, A.; Wolfrum, B. Nanostructured Cavity Devices for Extracellular Stimulation of HL-1 Cells. *Nanoscale* **2015**, *7*, 9275–9281.

(198) Li, P.; Greben, K.; Wördenweber, R.; Simon, U.; Offenhäusser, A.; Mayer, D. Tuning Neuron Adhesion and Neurite Guiding Using Functionalized AuNPs and Backfill Chemistry. *RSC Adv.* **2015**, *5*, 39252–39262.

(199) Mahoney, M. J.; Chen, R. R.; Tan, J.; Saltzman, W. M. The Influence of Microchannels on Neurite Growth and Architecture. *Biomaterials* **2005**, *26*, 771–778.

(200) Repić, T.; Madirazza, K.; Bektur, E.; Sapunar, D. Characterization of Dorsal Root Ganglion Neurons Cultured on Silicon Micro-Pillar Substrates. *Sci. Rep.* **2016**, *6*, 39560.

(201) Tysseling-Mattiace, V. M.; Sahni, V.; Niece, K. L.; Birch, D.; Czeisler, C.; Fehlings, M. G.; Stupp, S. I.; Kessler, J. A. Self-Assembling Nanofibers Inhibit Glial Scar Formation and Promote Axon Elongation after Spinal Cord Injury. *J. Neurosci.* **2008**, *28*, 3814–3823.

(202) Park, M.; Oh, E.; Seo, J.; Kim, M. H.; Cho, H.; Choi, J. Y.; Lee, H.; Choi, I. S. Control over Neurite Directionality and Neurite Elongation on Anisotropic Micropillar Arrays. *Small* **2016**, *12*, 1148–1152.

(203) Singh, K. Interaction of Biomembranes with Nanostructures, Not Published, University of Cologne, **2017**.

(204) Helfrich, W. Elastic Properties of Lipid Bilayers: Theory and Possible Experiments. *Z. Naturforsch. C.* **1973**, *28*, 693–703.

(205) Kell, A.; Glaser, R. W. On The Mechanical and Dynamic Properties of Plant Cell Membranes: Their Role in Growth, Direct Gene Transfer and Protoplast Fusion. *J. Theor. Biol.* **1993**, *160*, 41–62.

(206) Dai, J.; Sheetz, M. P.; Wan, X.; Morris, C. E. Membrane Tension in Swelling and Shrinking Molluscan Neurons. *J. Neurosci.* **1998**, *18*, 6681–6692.

(207) Hochmuth, F. M.; Shao, J. Y.; Dai, J.; Sheetz, M. P. Deformation and Flow of Membrane

into Tethers Extracted from Neuronal Growth Cones. *Biophys. J.* **1996**, *70*, 358–369.

(208) Xie, X.; Xu, A. M.; Angle, M. R.; Tayebi, N.; Verma, P.; Melosh, N. A. Mechanical Model of Vertical Nanowire Cell Penetration. *Nano Lett.* **2013**, *13*, 6002–6008.

(209) Xie, X.; Aalipour, A.; Gupta, S. V.; Melosh, N. A. Determining the Time Window for Dynamic Nanowire Cell Penetration Processes. *ACS Nano* **2015**, *9*, 11667–11677.

(210) Gomez, N.; Chen, S.; Schmidt, C. E. Polarization of Hippocampal Neurons with Competitive Surface Stimuli: Contact Guidance Cues Are Preferred over Chemical Ligands. *J. R. Soc. Interface* **2007**, *4*, 223–233.

(211) Kang, K.; Yoon, S. Y.; Choi, S. E.; Kim, M. H.; Park, M.; Nam, Y.; Lee, J. S.; Choi, I. S. Cytoskeletal Actin Dynamics Are Involved in Pitch-Dependent Neurite Outgrowth on Bead Monolayers. *Angew. Chemie - Int. Ed.* **2014**, *53*, 6075–6079.

(212) Bovolenta, P.; Mason, C. Growth Cone Morphology Varies with Position in the Developing Mouse Visual Pathway from Retina to First Targets. *J. Neurosci.* **1987**, *7*, 1447–1460.

(213) Chang, T. Y.; Yadav, V. G.; De Leo, S.; Mohedas, A.; Rajalingam, B.; Chen, C. L.; Selvarasah, S.; Dokmeci, M. R.; Khademhosseini, A. Cell and Protein Compatibility of Parylene-C Surfaces. *Langmuir* **2007**, *23*, 11718–11725.

(214) Weiss, P. Experiments on Cell and Axon Orientation in Vitro: The Role of Colloidal Exudates in Tissue Organization. *J. Exp. Zool.* **1945**, *100*, 353–386.

(215) Shefi, O.; Ben-Jacob, E.; Ayali, A. Growth Morphology of Two-Dimensional Insect Neural Networks. *Neurocomputing* **2002**, *44–46*, 635–643.

(216) Godement, P.; Wang, L.-C.; Mason, C. A. Retinal Axon Divergence in the Optic Chiasm – Dynamics of Growth Cone Behaviour at the Midline. *J. Neurosci.* **1994**, *11*, 7024–7039.

(217) Baranes, K.; Kollmar, D.; Chejanovsky, N.; Sharoni, A.; Shefi, O. Interactions of Neurons with Topographic Nano Cues Affect Branching Morphology Mimicking Neuron-Neuron Interactions. *J. Mol. Histol.* **2012**, *43*, 437–447.

(218) Seyock, S.; Maybeck, V.; Scorsone, E.; Rousseau, L.; Hébert, C.; Lissorgues, G.; Bergonzo, P.; Offenhäusser, A. Interfacing Neurons on Carbon Nanotubes Covered with Diamond. *RSC Adv.* **2017**, *7*, 153–160.

(219) Arnold, M.; Cavalcanti-Adam, E. A.; Glass, R.; Blümmel, J.; Eck, W.; Kantlehner, M.; Kessler, H.; Spatz, J. P. Activation of Integrin Function by Nanopatterned Adhesive Interfaces. *ChemPhysChem* **2004**, *5*, 383–388.

(220) Cavalcanti-Adam, E. A.; Volberg, T.; Micoulet, A.; Kessler, H.; Geiger, B.; Spatz, J. P. Cell Spreading and Focal Adhesion Dynamics Are Regulated by Spacing of Integrin Ligands. *Biophys. J.* **2007**, *92*, 2964–2974.

(221) Jang, K. J.; Kim, M. S.; Feltrin, D.; Jeon, N. L.; Suh, K. Y.; Pertz, O. Two Distinct Filopodia Populations at the Growth Cone Allow to Sense Nanotopographical Extracellular Matrix Cues to Guide Neurite Outgrowth. *PLoS One* **2010**, *5*.

(222) Kang, D.; Standley, A.; Chang, J. H.-C.; Liu, Y.; Tai, Y.-C. Effects of Deposition Temperature on Parylene-C Properties. *2013 IEEE 26th Int. Conf. Micro Electro Mech. Syst.* **2013**, 389–390.

(223) Sohal, H. S.; Jackson, A.; Jackson, R.; Clowry, G. J.; Vassilevski, K.; O'Neill, A.; Baker, S. N. The Sinusoidal Probe: A New Approach to Improve Electrode Longevity. *Front. Neuroeng.* **2014**, *7*, 10.

(224) Leach, J. B.; Brown, X. Q.; Jacot, J. G.; Dimilla, P. A.; Wong, J. Y. Neurite Outgrowth and

127

Branching of PC12 Cells on Very Soft Substrates Sharply Decreases below a Threshold of Substrate Rigidity. *J. Neural Eng.* **2007**, *4*, 26–34.

(225) Kim, E. G. R.; John, J. K.; Tu, H.; Zheng, Q.; Loeb, J.; Zhang, J.; Xu, Y. A Hybrid Silicon-Parylene Neural Probe with Locally Flexible Regions. *Sensors Actuators, B Chem.* **2014**, *195*, 416–422.

(226) Kim, H. N.; Jang, K.-J.; Shin, J.-Y.; Kang, D.; Kim, S. M.; Koh, I.; Hong, Y.; Jang, S.; Kim, M. S.; Kim, B.-S.; *et al.* Artificial Slanted Nanocilia Array as a Mechanotransducer for Controlling Cell Polarity. *ACS Nano* **2017**, acsnano.6b07134.

(227) Li, G. N.; Hoffman-Kim, D. Tissue-Engineered Platforms of Axon Guidance. *Tissue Eng. Part B. Rev.* **2008**, *14*, 33–51.

ACKNOWLEDGMENTS

I wish to express sincere thanks to all the people that were around me before and during my PhD. You all contribute to the person and scientist that I am today. Many thanks to the PGI-8/ICS-8 institute, collaborators, and the following people in particular:

Prof. Dr. Andreas Offenhäusser, thank you for providing a platform for success in the academic environment. I appreciate the endless support that you offered me and the fact that you always see the positive part in any situation.

Dr. Dirk Mayer, thank you for your valuable time. The fruitful discussions, advices, and guidance from the beginning until submission made this thesis possible. Thanks for constant motivation and patience.

Prof. Dr. Ulrich Simon, many thanks for being co-examiner for my thesis. I appreciate the time and help.

IHRS BioSoft, for all the nice courses that help to improve my knowledge in other fields. New collaboration and friends was the benefit of being part of this school. Many thanks for organization go towards Dr. Thorsten Auth.

Dr. Gokhan Demirel (Gazi University, Turkey), sincere thanks for PPX fabrication and all the support.

Karandeep Singh and **Dr. Thorsten Auth**, thank you for the nice collaboration regarding theoretical calculation part in the thesis.

Many thanks to the cleanroom team: Michael, Regina, Stefan, Iris, Georg, Marko. **Michael**, I cannot image the cleanroom without you. Your help was invaluable in all aspects and I wish you never change. **Elmar**, you also have a special place in the thank you list. Your willingness to extend a helping hand is a great quality. Elke, Gregor, Steffy, Florian, thank you for all the help. Vanessa and Tina, many thanks for introducing me to the bio world and organization help.

My colleagues from Molecular Bioelectronics group for all the support. Your presence and patience during long meetings made this journey easier: Frano, Quang, Silke, Irina, Pinggui, Mana, Paromita, Francesca, Mathis, Volker, Dmitry.

Special thanks must go to the contribution of some people who started colleagues but become amazing friends. From the moment I enter the research group, me, Stella, and Dmitry made a great team. We shared the kicker practice, as mandatory step to finish the PhD, anniversaries, and great memories. Many other people also made an interesting and entertaining experience: Qiu, Viviana, Frano, Mathis, Nouran, Fabian, Bastian, Volker, Alexey, Hanna. Silke, thank you for everything, you are the most organized and helpful person I know. Big thanks to Irina for always being cheerful and chatty. I also want to thank

the people from FZJ that made the commuting enjoyable: "RTB people" and "quality time in Düren".

I hope I have not forgotten anyone, and if I have then please be assured that you have my deepest thanks.

Finally, no acknowledgement for this thesis would be complete without recognizing the love, support, and motivation given to me by my husband.

Mulțumesc din suflet profesorilor, prietenilor și familiei pentru că ați făcut parte din evoluția mea profesională și personală. Sunt azi ceea ce sunt datorită fiecăruia dintre voi.

This thesis is dedicated to my grandfather for being my inspiration.

Aceasta teză este dedicată bunicului meu.

Sper că am devenit omul bun și inventiv pe care tu l-ai crescut și inspirat. Mulțumesc!

APPENDIX A: ABBREVIATIONS

BCI	Brain computer interfaces
FDA	Food and Drugs Administration
CNS	Central nervous system
PNS	Peripheral nervous system
ECM	Extracellular matrix
DIV	Days *in vitro*
PLL	Poly-L-lysine
PDL	Poly-D-lysine
SAMs	Self-assembled monolayers
PDMS	Polydimethylsiloxane
Parylene C, PPX	Poly(dichloro-p-xylylene)
AFM	Atomic force microscopy
SEM	Scanning electron microscopy
BE	Backscattered electrones
SE	Secondary electrones
FIB	Focus Ion Beam
EBL	Electron beam lithography
NIL	Nanoimprint lithography
PMMA	Polymethylmethacrylate
RIE	Reactive ion etching
FOTCS	Trichloro(1H,1H,2H,2H-perfluorooctyl)silane
GBSS	Grey's Balance Salt Solution
PFA	Paraformaldehyde
PBS	Phosphate buffered saline
BB	Blocking buffer
AF	Alexa Flour
DAPI	4',6-diamidino-2-phenylindole
CPD	Critical point drying
OsO_4	Osmium tetroxide
UrAc	Uranyl acetate
MEAs	Microelectrodes arrays

APPENDIX B: MATERIALS AND SOLUTIONS

B1. Reagents list

Reagent	Supplier	Specification
Polymethylmethacrylate (PMMA)	Allresist	AR-P 669.04 600K
Developer AR 600-55	Allresist	
Iso propanol	Sigma-Aldrich	≥99.5%
N_2		purity of 99.8%
MilliQ	Elix and MilliQ system of Millipore	18.2 MΩ
Acetone	Sigma Aldrich	99.5%, highly flammable
Trichloro(1H,1H,2H,2H-perfluorooctyl)silane (FOTCS)	Sigma Aldrich	97%
OrmoPrime	Micro resist technology	
OrmoThin	Micro resist technology	
OrmoComp	Micro resist technology	
Polydimethylsiloxane (PDMS)	Sylgard 184, Dow Corning Corporation	1:10
Ethanol absolute	Fischer Scientific	200 Proof, flammable liquid
Poly-*L*-lysine (PLL)	Sigma-Aldrich	10 mg/ml
Grey's Balance Salt Solution (GBSS)	Life Technologies	
B-27	Invitrogen	
L-Glutamine	Invitrogen	
Gentamycin	Sigma Aldrich	10 mg/ml
Neurobasal media	life technologies	
Fetal bovine serum	life technologies	
Trypsin/EDTA	life technologies	
Trypan blue	Sigma Aldrich	toxic reagent
Ethidium homodimer	Invitrogen	toxic reagent
Calcein AM	Sigma Aldrich	1mg/ml in dry DMSO
Paraformaldehyde (PFA)	Sigma Aldrich	powder, 95%

Alexa Fluor (AF 488, AF 546, AF 633)	Life Technologies	
AntiMAP2	Millipore	
40,6-Diamidino-2-phenylindole dihydrochloride (DAPI)	Sigma Aldrich	1 mg/ml
Anti-200 kD Neurofilament Heavy (NFH)	abcam	2 mg/ml
Anti-Tau1	Life Technologies	
Glutaraldehyde solution	Sigma Aldrich	50% in H_2O solution. The reagent is specially purified for use as an electron microscopy fixative.
Cacodylate buffer	Morphisto	pH 7.4, 0.1 mol/l
Epoxy embedding medium (1,2,3 propanetriol, polymer with 2-(chloromethyl)oxirane)	Sigma Aldrich	may cause skin irritation, eye irritation and respiratory irritation.
Epoxy embedding medium, hardener DDSA - (Dihydro-3-(tetrapropenyl)furan-2,5-dione)	Sigma Aldrich	may causes and eye irritation.
Epoxy embedding medium, hardener MNA ≥95.0% (Methyl-5-norbornene-2,3-dicarboxylic anhydride)	Sigma Aldrich/ Fluka	may cause skin irritation, eye irritation and respiratory irritation.
DMP (2,4,6 tris(dimethylaminomethyl)phenol 95% (, cat. no. T58203)	Sigma Aldrich	may cause skin irritation, eye irritation and respiratory irritation.
Osmium tetroxide (OsO_4)	Sigma Aldrich	highly toxic chemical
Tannic acid	Electron Microscopy Sciences	low molecular weight
Uranyl acetate	Electron Microscopy Sciences	2% solution in water, depleted uranium
NaCl	Sigma Aldrich	
KCl	Sigma Aldrich	
Na_2HPO_4	Sigma Aldrich	
KH_2PO_4	Roth	

B2. Solutions

B2.1. Cortical Neurons media

100 μl of B27 (final concentration 1% vol/vol), 25 μl of L-glutamine (final concentration 0.25% vol/vol), 10 μl of gentamycin (final concentration 1‰ vol/vol) were added to 10 ml of Neurobasal media.

B2.2. Phosphate Buffer Saline solution (PBS)

In one l of distilled water, NaCl is dissolved to a final concentration of 137 mM, KCl to a final concentration of 2.7 mM, Na_2HPO_4 to a final concentration of 8 mM, and KH_2PO_4 to a final concentration of 1.8 mM. This solution is then diluted in a concentration of 1:10 in distilled water.

B2.3. Resin solution

As shown in Figure A1, in a 50 ml flacon tube 12.5 ml solution of Epon embedding medium was mixed sorely with 20 ml DDSA for 5 minutes (A). In parallel, a solution consisting of 17.5 ml Epon embedding medium and 15 mL MNA was prepared in a plastic tube as shown in Figure 1B. Afterwards, the two solutions were poured at the same time into a plastic container containing a magnetic stirrer and 1.3 ml DMP30 was added. At this step, the color of the final solution is typically red/orange (C). After 1h of stirring at room temperature the resin solution was prepared and the color changed in yellow (D). Finally, the epoxy solution can be directly used for infiltration. For an eventual storage the resin solution was picked up into 20 ml syringes (E), labeled (F), and stored at -20°C (G). The resin solution should not exceed one month of storage and before usage the solution was left for 10 min at room temperature.
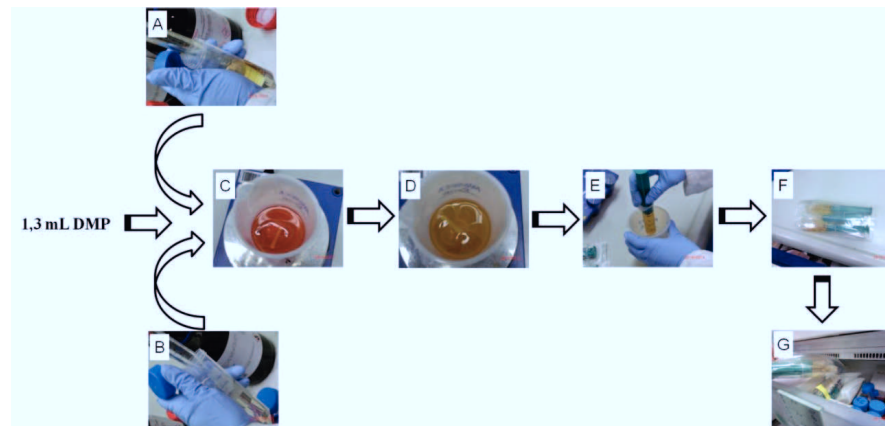

Figure A1. Resin preparation and storage.

APPENDIX C: CLEANROOM RECIPES

C1. Recipe for Si/SiO$_2$ mold fabrication (100 nm depth structures)

Mold substrate:	4 inch, p-silicon <100> 100 nm SiO$_2$
Resist:	PMMA AR-P669.04, 3000 rpm 180 °C, 300 sec
EBL:	Arrays: beam size 5 nm, 2 nA beam current, 50 kV voltage, 230 µC/cm^2 dose Labels: 50 nm beam size, 150 nA beam current, and 250 µC/cm^2 dose
Development:	AR 600.55 120 sec
RIE:	CHF$_3$/SF$_6$ 50/10 sccm, RF 25, ICP 2006, Bias 30, 0°C, 24 sec O$_2$ 45 sccm, 0°C, 90 sec

C2. Recipe for Si/SiO$_2$ mold fabrication (400 nm depth structures)

Mold substrate:	4 inch, p-silicon <100> 500 nm SiO$_2$
Resist:	PMMA AR-P669.04, 3000 rpm 180 °C, 300 sec double coating of resist with same parameters
EBL:	Arrays: beam size 5 nm, 2 nA beam current, 50 kV voltage, 230 µC/cm^2 dose Labels: 50 nm beam size, 150 nA beam current, and 250 µC/cm^2 dose
Development:	AR 600.55, 120 sec
RIE:	SiO$_2$ etching: CHF$_3$/SF$_6$ 50/10 sccm, RF 25, ICP 1500, Bias 50, -100 °C, 90 sec PMMA etching: O$_2$ 45 sccm, 0°C, 90 sec

C3. Parylene deposition for replica fabrication

RWTH Aachen, Institut für Werkstoffe der Elektrotechnik
PDS 2010 E LABCOTER 1 (firma SCS)

Material DPX-C	Lot. Nr. 14A21007
Temp. vapo	175°C
Temp. pyro	690°C
Temp. P.G.	135°C
Mass	5,45 g
Thickness	12988 ±156,9nm

Band / Volume 149
**Kinetic and thermodynamic considerations on the formation
of heteromolecular layers on metal surfaces**
C. Henneke (2017), vii, 157, XIV pp
ISBN: 978-3-95806-245-0

Band / Volume 150
**Spectroscopic characterization of local valence change processes
in resistively switching complex oxides**
C. Bäumer (2017), x, 206 pp
ISBN: 978-3-95806-246-7

Band / Volume 151
**Magnetic structure in relation to the magnetic field induced ferroelectricity
in Y-type hexaferrite Ba $_{2-x}$Sr$_x$Zn$_2$Fe$_{12}$O$_{22}$**
P. Thakuria (2017), 17, 180 pp
ISBN: 978-3-95806-250-4

Band / Volume 152
**Statistical analysis tools for assessing the functional relevance
of higher-order correlations in massively parallel spike trains**
V. Rostami (2017), x, 176 pp
ISBN: 978-3-95806-251-1

Band / Volume 153
**The influence of the substrate on the structure and electronic properties
of carbon-based 2D materials**
J. Sforzini (2017), XIII, 145 pp
ISBN: 978-3-95806-255-9

Band / Volume 154
**Gate-All-Around Silicon Nanowire Tunnel FETs for Low Power
Applications**
G. V. Luong (2017), ii, 136 pp
ISBN: 978-3-95806-259-7

Band / Volume 155
Graphene Devices for Extracellular Measurements
D. Kireev (2017), ix, 169 pp
ISBN: 978-3-95806-265-8

Band / Volume 156
**Nanoscale 3D structures towards improved cell-chip
coupling on microelectrode arrays**
S. D. Weidlich (2017), II, 154 pp
ISBN: 978-3-95806-278-8

Band / Volume 157
Interface phenomena in La$_{1/3}$Sr$_{2/3}$FeO$_3$ / La$_{2/3}$Sr$_{1/3}$MnO$_3$
heterostructures and a quest for p-electron magnetism
M. Waschk (2017), ix, 205 pp
ISBN: 978-3-95806-281-8

Band / Volume 158
Physics of Life
Lecture Notes of the 49th IFF Spring School 2018
26 February – 09 March 2018, Jülich, Germany
ed. by G. Gompper, J. Dhont, J. Elgeti, C. Fahlke, D. Fedosov,
S. Förster, P. Lettinga, A. Offenhäusser (2018), ca 1000 pp
ISBN: 978-3-95806-286-3

Band / Volume 159
Identifizierung von Bindungsdeterminanten von Tat-Vorläuferproteinen
an den TatBCRezeptorkomplex während der Tat-abhängigen
Proteintranslokation in *Escherichia coli*
A. Ulfig (2018), 186 pp
ISBN: 978-3-95806-290-0

Band / Volume 160
***Corynebacterium glutamicum* – a novel platform for the production**
of plant polyphenols
N. Kallscheuer (2018), XIII, 98 pp
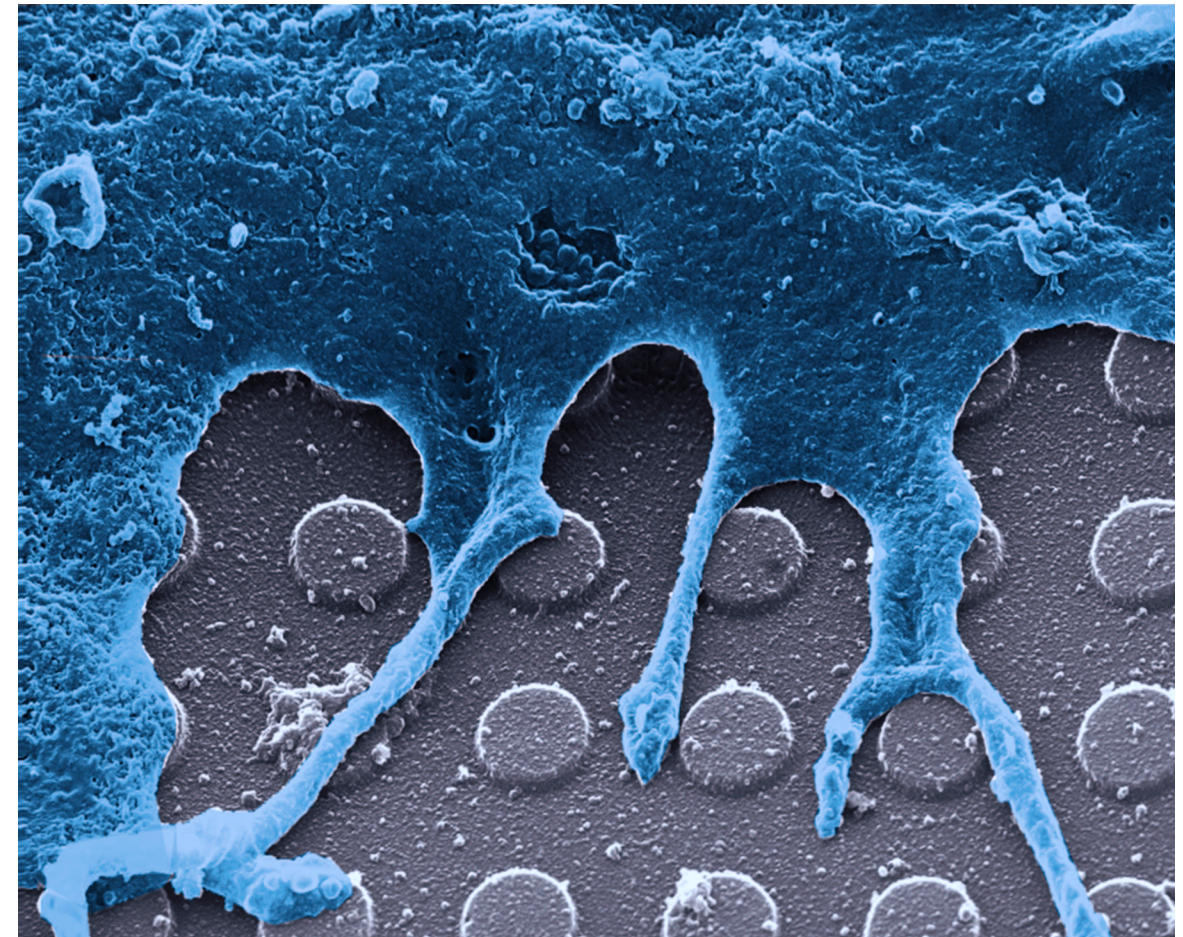ISBN: 978-3-95806-291-7

Band / Volume 161
Neurons on 3D polymer nanostructures
A. Belu (2018), vii, 135 pp
ISBN: 978-3-95806-296-2

Weitere ***Schriften des Verlags im Forschungszentrum Jülich*** unter
http://wwwzb1.fz-juelich.de/verlagextern1/index.asp

Schlüsseltechnologien
Key Technologies

Neurons on 3D polymer nanostructures

161

Neurons on 3D polymer nanostructures

Andreea Anamaria Belu

Andreea Anamaria Belu

JÜLICH
Forschungszentrum

Mitglied der Helmholtz-Gemeinschaft

JÜLICH
Forschungszentrum

Mitglied der Helmholtz-Gemeinschaft

JÜLICH
Forschungszentrum